Enabling wide-field, high-spatial-resolution fast transient searches on modern interferometry

Dissertation

zur

Erlangung des Doktorgrades (Dr. rer. nat.)

der

Mathematisch-Naturwissenschaftlichen Fakultät
der

Rheinischen Friedrich-Wilhelms-Universität Bonn

vorgelegt von

Weiwei Chen

aus

Guangdong, China

Bonn, Oktober 2021

Angefertigt mit Genehmigung der Mathematisch-Naturwissenschaftlichen Fakultät der Rheinischen Friedrich-Wilhelms-Universität Bonn

1. Referent:	Prof. Dr. Michael Kramer
2. Referent:	Prof. Dr. Frank Bertoldi
Tag der Promotion:	21.02.2022
Erscheinungsjahr:	2022

Abstract

Fast transients reveal the energetic universe to us. They are usually the products of rapid and enormous energy releases. To study the physical nature behind them, we must know the subtle temporal structure of the signal and where precisely they come from. Radio observation has been an indispensable part of the study of fast transients, thanks to their daylight-insusceptibility and weather-tolerance. The ever powerful single-dish telescopes have been used in pulsar observations and fast radio transient surveys, yielding substantial results. However, some sporadic or even one-off fast radio transients have brought challenges to the single-dish observations. Other than high time resolution, efficient fast transient surveys require a wide field of view and spatial resolution. While larger single-dish telescopes are harder and much expensive to build, interferometry provides a practical alternative. The high spatial resolution, scalability, flexibility and cost-efficiency have made interferometry wildly used in modern radio astronomy. With the beamforming techniques, interferometric arrays are able to carry out wide-field, high resolution surveys for fast radio transients.

In this thesis, I start the introduction with an instrument-wise history of radio observation and its importance in astronomy. Following that is the introduction of the fast radio transients, including various types of pulsars and fast radio bursts. Then I present radio interferometry as a solution to tackle the challenges in the fast radio transient surveys. A brief history of radio interferometry and its achievements are also provided.

The second chapter presents the various requirements for fast radio surveys with interferometry, such as high time and frequency resolution, large field of view and high spatial resolution. I then explain how beamformed observation with interferometric arrays can meet these requirements. A comparison between the raw-voltage beamforming and visibility beamforming is presented in the perspective of computing complexity. At the end of the chapter, I briefly outline the configuration of the MeerKAT telescope, its various backends and planned science projects. The overview of the transient search system of MeerKAT based on the abovementioned beamforming technique is presented. The reason for MeerKAT using the raw-voltage beamforming method is explained.

The third chapter describes the general beamforming technique in detail and provides its implementation. Following that, I provide the solutions to the challenges that come with this technique, such as the characterization of volatile beam shapes, the generation of efficient tiling of beams and the prediction of the evolution of the tiling through time. To provide a more realistic perspective, the integration of these techniques in the MeerKAT telescope is illustrated and the corresponding capacity and statistics are provided. As an evaluation, a real beamformed observation on 47 Tucanae using the said techniques is presented and the localization capability with multiple beams is demonstrated. The development and deployment of this technique have been proven successful and effective.

The performance of this beamforming platform has been further tested in numerous observations and surveys which are detailed in the fourth chapter. For example, the TRAPUM project consisting of but is not limited to surveys of globular clusters, nearby galaxies and targeted pulsar searches of unidentified FERMI gamma-ray sources. Another important survey is the MGPS project which searches pulsars in the Galactic plane at both L-band and S-band. From both projects, we have discovered a total of 66 pulsars at the time of writing.

I report a search for giant pulses in selected pulsars in the fifth chapter. Many models try to explain the emission mechanism behind giant pulses from pulsars, some of which invoke the re-connection events near the light cylinder. In the meantime, a population of giant pulse emitters shares similar properties, such as strong magnetic fields near the light cylinder and high energy emission. I select

a couple of pulsars with these properties as candidates. They were observed using the Effelsberg 100-meter telescope. I created a pipeline based on Heimdall to search giant pulses on the data and find no credible detection. The conclusion for the non-detection is that these pulsars do not emit giant pulses which are detectable by our observation, or the condition of high magnetic field strength near the light cylinder and high energy emission may not be a sufficient condition for the occurrence of giant pulses.

To my parents

Acknowledgements

I would like to express my sincere gratitude to the people that help me with this thesis and my PhD. There are so many people who offer helps in various ways. It could be official guidance, routine meetings, or a snap discussion of the matters. It also could be a simple question, a chat about the currents or a casual talk about our plans. Sometimes, a brief conversation or a single smile would keep me energetic for the whole day.

The first person I want to thank is my supervisor, Prof. Dr. Michael Kramer. I am grateful to him for giving me such an amazing opportunity to study here. It is always a pressure to talk with him, because he can always find ways to encourage me and provide creative solutions for all kinds of situations. Second, I would like to thank my day-to-day advisors Ewan Barr and Ramesh Karuppusamy. Their infinitive patience has made me comfortable as a novice in the field. I also thank them for their kindness for putting up with me. I want to thank Prof. Dr. Frank Bertoldi for giving me advices on my doctoral studies. I want to thank Alessandro Ridolfi, Federico Abbate and Robert Wharton for the helps they provided for my study.

My officemates also play important parts in my PhD. I am very lucky to have Jackie in my office because he made everything much easy for me. Jackie and I speak a similar mother tongue, which made my first arrival and the next few months much easier. It is also very nice to have him as a friend during my PhD as he taught me a lot of things. Madhuri Gaikwad arrived half a month before me, so we can help each other a lot in this new environment. Maja Kiedorf is my guide to German society and culture, what's more, she helped me in a lot of situations when German-speaking was required. I couldn't ask for better officemates!

The study mates in the institute have made my life much easier. I forget how many times I knocked on Marilyn Cruces's door to ask all sorts of questions and she always gave distinct answers. Eleni Graikou's laugh is always the sunshine in the group and she greets everyone nicely. I want to thank Nataliya Porayko for being my IMPRS buddy and provided me with much useful information while I arrived. There are also Joscha Jahns, Tim Sprenger and Ferdinand Jünemann who are very nice and help me a lot in German. I also felt really happy when I spent time with Hans Nguyen, Maitraiyee Tiwari, Arshia Jacob, Felix Pötzl and Fateme Kamali.

My study in the institute has also benefited from the help of Tuyet-Le Tran, Kira Kühn, Mariya Halvadzhieva and Barbara Menten in countless situations.

The staff of MeerKAT telescope has helped me in various ways, including giving suggestions about my code, taking the commissioning data for me to perform tests and taking observation on 47 Tucanae for my study. I also want to thank the staff of Effelsberg telescope for setting up and taking observations for the giant pulses searching project.

The IMPRS has provided me with great channels to connect with other students and to be involved in various academic activities. They opened my mind and enriched my perspectives. I also thank the European Research Council Synergy Grant BlackHoleCam for providing the funding for my study.

I want to give my thanks to my parent, Binhuang Chen and Zhaozhen Liang. It is so nice to talk to them even when I am very far away from home. Their supports for my pursuit give me the strengths to overcome the obstacles.

Finally, I want to thank the trees outside the institute, also the ones I saw during my hiking in Bonn. Whenever I was scratching my head and feeling stress, they were always there to calm me, to suggest I take a break so that I can appreciate the beauty of nature and the kind people around me.

Contents

CHAPTER 1

Introduction

From the first successful detection of an extraterrestrial radio source (Jansky, 1933a) to the present day, radio observations have been used for tracing back to the earliest moments of the Universe (e.g. Basu et al., 2019). The art of observing celestial sources at radio frequencies has evolved constantly with the development of ever more powerful observational techniques and instruments. In this thesis, I present beamforming, an increasingly important radio interferometric technique used in the fast transient search, and the corresponding observational strategies applied on the latest instrument. I also report an attempt to search giant pulses with the Effelsberg telescope.

Contents

1.1 Radio astronomy

Objects radiate energy in the form of electromagnetic waves across a range of frequencies. Visible light, to which the human eye is sensitive, occupies only a small subset of the electromagnetic spectrum which we split into sub-divisions by wavelength or energy.

Radio astronomy is interested in the radiative properties of celestial objects in the frequency range from 10^4 Hz to 10^{11} Hz. This broad radio spectrum is further divided into sub-bands and probed by different types of radio receptors. The ability to detect weak signals, called "sensitivity", is achieved by increasing the effective collecting area because the bigger the area the more photons can be collected. The ability to better resolve objects at a certain wavelength is achieved by increasing the spatial extent of the receptors according to the Rayleigh criterion $\theta = 1.22\frac{\lambda}{D}$ where λ is the wavelength and D is the extent of the receptor.

1.1.1 Importance of radio astronomy

Radio astronomy has greatly increased the observable window of the electromagnetic spectrum. Before the establishment of radio astronomy, observations were typically done with optical telescopes, and although this was done with great success, it had its limitations.

Natural radiation often emits in a broad spectrum. For instance, Active Galactic Nuclei (AGN) emit radiation in frequency regions spanning over radio, infrared, optical, x-ray and gamma-ray. The spectral behavior in each region can indicate different emission mechanisms and the presence or absence of emission in specific parts of the spectrum can be important in identifying the physical properties of the object. Only with the knowledge of the emission across a broad spectrum, can we learn the complete picture of the physical activity of the source.

Sources embedded in dense environments can still be observed at radio frequencies. Events like supernova generate a great amount of dust filling the remnant of the explosion. Dusty and cloudy environments surround the region where the star is being born. Due to the high optical depth (a measure of the amount of absorption occurring during propagation), it is hard to observe these sources with optical telescopes. Since radio emission propagates at much longer wavelengths than the size of the dust and clouds surrounding the source, significantly less absorption happens before it arrives at the telescope. This allows radio telescopes to more easily seeing through areas behind an optically thick medium. For example, Ginsburg et al. (2016) proposed a method to detect the stars inside the dense and dusty environment near the Galactic center through their synchrotron emission.

Another big obstacle is the atmosphere of Earth which blocks radiation from gamma-ray to ultraviolet, distorts visible light and absorbs infrared radiation, leaving the radio region a crucial window for astronomy as illustrated in 1.1.

Thanks to the fact that radio observations are less affected by weather and not affected by daylight, the availability of telescopes to scientists is greatly increased, allowing for the possibility of long and uninterrupted observations.

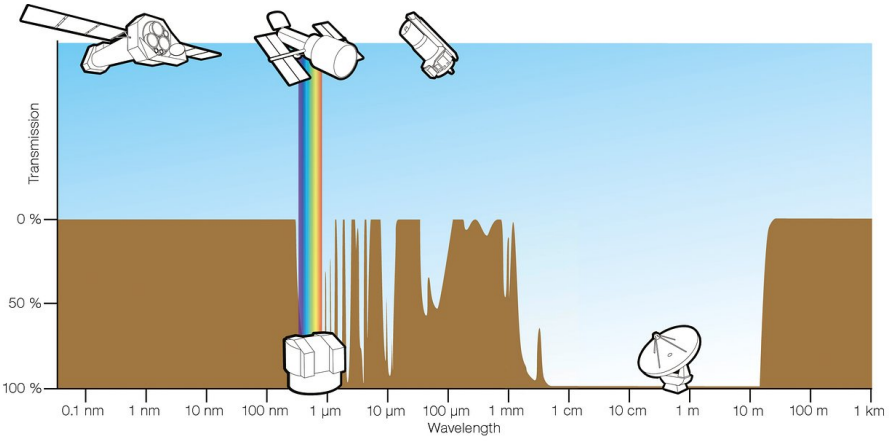

Figure 1.1: Transparency of the atmosphere and the preferred instruments for different atmosphere windows. Credit: ESA/Hubble (F. Granato)

Furthermore, radio observatories are easier to build and more flexible to use than their counterparts at other frequencies. Unlike the high energy telescopes that need to be carried by expensive spacecraft into orbit to avoid the atmosphere blockage and the also expensive and sophisticated mechanism of optical telescopes, radio telescopes are cheaper and easier to build and maintain. The new generation radio telescope arrays are designed to be flexible, extensible and reconfigurable to accommodate different scientific goals.

1.1.2 History of radio astronomy in instrumental perspective

Since James Clerk Maxwell unified electricity and magnetism with the Maxwell equation and predicted the existence of radio waves proven by Heinrich Hertz, people had tried to detect extraterrestrial radio signals.

Jansky detected a radio signal from the constellation Sagittarius using a rotating telescope. Originally tasked with the study of the interference in the long distance radio telephone calls, Jansky built a large circularly movable antenna so that he could steer it to different directions to track or localize the interference. During his study, an unknown interference appeared in his observations every 23 hours, 56 minutes and 4 seconds. He concluded that this interference is coming from outer space (Jansky, 1933c) as that interval is the period of the Earth's rotation and the same celestial object will appear in the same location in the sky 3 minutes and 56 seconds earlier each day. Jansky later managed to localize the interference to the constellation Sagittarius (Jansky, 1933b).

Following up on Jansky's work, Grote Reber built a parabolic dish reflector which is considered to be the first radio telescope. It could be steered in altitude and had a diameter of 9 meters and 3 receivers for different frequencies. He successfully used the telescope to carry out the earliest radio continuum survey, mapping the Galactic radio emission (Reber, 1944).

The need for exploring the Universe in higher sensitivity has driven the telescopes to get bigger and better in the last half century. Bernard Lovell designed the first large fully steerable radio telescope with an alt-azimuth mount and a diameter of 76 meters in 1957. The construction of the Effelsberg 100-meter telescope in 1971 increased the maximum size of a steerable dish by

overcoming considerable mechanical challenges related to gravitational deformation of the dish at different elevations. The Green Bank telescope build in 2000 also has a similar aperture to Effelsberg but with an offset feed and an asymmetric dish allowing the incoming radio waves to reach the focus without any blockage. This efficient structure serves as an example of the later widely used offset Gregorian structure in the new generation of telescopes.

There were also attempts to increase the field of view of single-dish telescopes such as the use of a multi-beam receiver (Staveley-Smith et al., 1996) on the Parkes Radio Telescope. The success of this technique has made multi-beam observation important in radio astronomy and promoted a wide range of implementations of multi-beam systems in later telescopes.

The 305-meter Arecibo telescope and the Five-hundred-meter Aperture Spherical Telescope (FAST) have offered an unparalleled sensitivity of an observation, representing the highest performance in single dish telescopes.

An important requirement in radio astronomical applications is the need for high spatial resolution, an ability that is proportional to the aperture of the telescope. It has long been established that the most practical approach to achieving high spatial resolution in radio astronomy is interferometry. It is coherent additions of signals from geographically separated receiving elements. The separation can be up to thousands of kilometers or even longer to achieve the resolution that never could have been practical for single dish telescopes. The next generation Square Kilometre Array (SKA) will consist of hundreds of small telescopes at different distances to offer high spatial resolution and high sensitivity.

1.1.3 Important discoveries

Discoveries in radio astronomy have provided us with important tools to study and explore the Universe. In the meantime, the desire for yet further discoveries presses for even higher observation requirements, pushing forward the development of instrumentation for radio observations.

The discovery of the 21-centimeter hydrogen line provided a great tool to study the Universe. When the state of spinning of the proton and electron of a hydrogen atom changes, it emits a photon with a distinguishable wavelength of 21.106 cm which was firstly discovered by a radio telescope. Assuming hydrogen is abundant and uniformly distributed, we can use it as a probe to study the universe. One example is to observe the Doppler shift of the spectral line of hydrogen to study the movement of the Galactic arms.

The discovery of pulsars is another milestone in radio astronomy, for it provided an indispensable tool to probe the Universe and test fundamental physics in extreme environments. In recent decades, a new kind of transient phenomenon called “Fast radio bursts” (FRBs) has been discovered. FRBs are so far only detectable in radio. Thanks to their extra-galactic origins, they have great potential for the study of cosmology and the intergalactic medium. Pulsars and FRBs are discussed in Section 1.2.2 in more detail.

The origin of the Universe is one of the most fundamental questions in physics. One of the theories of the creation of the Universe predicts that the Big Bang must have released a blast of radiation filling the Universe. Penzias and Wilson (1965) reported a non-removable residual background noise of 3.5 K in their study of radio waves and interpreted it as the signature of the Big Bang. The discovery of this cosmic microwave background (CMB) was critical evidence supporting the “Big bang” model of the birth of the universe. Since then the CMB became an important tool to study the early state and evolution of the Universe.

1.2 New challenge: fast radio transients

Fast radio transients are irregularly appearing radio emissions whose time scale is below 1 second. Among them, events like milliseconds or even shorter bursts spark wide scientific interest because bursts in an extremely short time scale usually indicate large energy release from the interaction among compact objects or cataclysmic events. This energetic phenomenon could provide us with unique laboratories to study fundamental physics in extreme environments.

1.2.1 Pulsars

Pulsars are fast rotating, highly magnetized neutron stars. Discovered by Jocelyn Bell Burnell in 1967, pulsars quickly became one of the most important sources in astronomy for their applications in a wide range of scientific fields.

They are the product of a supernova when a star with mass many times of our Sun reaches its end. When a massive ($8M_{sun} < M < 40M_{sun}$) star runs out of the hydrogen in its core, it leaves the main sequence phase and becomes a red giant. Fusion continues with heavier nuclei until the radiative and gas pressure from the fusion reaction can no longer counter the gravitational forces acting on the star. In the event of a supernova during the collapse, if the remaining mass of the star is around 1.4 Solar masses, a neutron star might be formed. Despite a large reduction in radius, most of the angular momentum and magnetic flux are conserved, resulting in the fast rotation and high magnetic field of the newborn neutron star.

The signals from most pulsars arrive at the Earth in very precise intervals. These signals are thought to come from the region near the magnetic axis of the pulsar. The periodicity is due to the misalignment between the rotation axis and the magnetic axis as illustrated in Figure 1.2. A single pulse (see Figure 1.3) can be detected when the continuous emission of the pulsar sweeps across the observer on Earth like a beam from a lighthouse.

Observational properties of pulsar

Period The rotation period is one of the most important observable parameters, as it reveals important information about the pulsar. Although the stability of the period is its renowned feature, it will slowly change through time. One of the reasons is that pulsars lose rotational energy with time because a rotating magnetic dipole in vacuum generates magnetic dipole radiation. Consider the pulsar as a simple axisymmetric system, the power of the radiation is:

$$P = \frac{2}{3}\frac{(BR^3 \sin\alpha)^2 \Omega^4}{c^3}, \tag{1.1}$$

where B is the strength of the magnetic field near the magnetic pole, R is the radius of the pulsar, α is the angle between the rotating axis and the magnetic axis, Ω is the rotation period of the pulsar and c is the speed of light. We usually call a pulsar an aligned rotator when $\alpha = 0^\circ$, an oblique rotator when $\alpha \neq 0^\circ$, and particularly, an orthogonal rotator when $\alpha = 90^\circ$. For the case of an (almost) orthogonal rotator, observers on earth would see the emission from both magnetic poles. In this situation, we usually call the pulse whose intensity is a fraction of the other pulse, an interpulse. As can be seen from the equation, the radiation occurs when $\alpha \neq 0^\circ$ as illustrated in Figure 1.2. The radiation propagates in the frequency of rotation of the pulsar, which is too weak to be directly observed on earth.

Spin down luminosity The loss of energy due to magnetic dipole radiation can be expressed as a function of the period. The rotation energy of a spinning sphere is:

$$E = \frac{1}{2} I\Omega^2, \tag{1.2}$$

where the I is the moment of inertia if we assume a neutron star is a rigid body of uniform density.

$$I = \frac{2MR^2}{5}. \tag{1.3}$$

and M is the mass of the pulsar, then assuming magnetic dipole radiation accounts for all the rotational energy loss:

$$-\dot{E} \equiv -\frac{dE}{dt} = -\frac{d}{dt}\left(\frac{1}{2} I\Omega^2\right) = -I\Omega\dot{\Omega} \tag{1.4}$$

We can rearrange the equation and obtain the loss of the energy or spin down luminosity as a function of the period

$$-\dot{E} = \frac{4\pi^2 I\dot{P}}{P^3}, \tag{1.5}$$

where $P = 2\pi/\omega$ and $\dot{P}$ is the derivative of the period.

Dispersion measure The radiation of pulsars is dispersed with a dependence on the square of the wavelength. That is because radio signals of different frequencies travel with a different group velocity through the interstellar medium (ISM) due to the frequency-dependent refractive index of the latter. For broadband signal, this leads to the power at high frequencies arriving at the observer earlier than the power at lower frequencies, as shown in Figure 1.3. We quantify this effect by the Dispersion Measure (DM), the integral of the free electron column density between the source and the observer. This is an important observational property because it reveals the information of the medium between the pulsar and the observer. A large DM may indicate that the radio wave travels a long distance or encounters a cloud of dense medium. In the meantime, the DM is crucial to reconstruct the signal, as the signal of a pulsar is strongly smeared by the ISM in low frequencies. Only with the correct DM can the dispersed power be aligned in time at all frequencies, so that they can be summed up coherently to increase the signal-to-noise ratio (S/N) of the detection.

Scattering and scintillation The random variation in the temporal and spatial density of the free electrons in the ISM scatters the radio waves propagating through it. This scattering effect causes a random irregularity in the signal intensity at the observer.

Depending on the wavelength and the distance between the scattering screen and the observer, scintillation can happen in either the weak regime and the strong regime (Narayan, 1992). The weak regime likely happens in the troposphere, ISM, ionosphere and the solar wind while the strong regime likely happens in ISM. Pulsars are extrasolar objects and observed at long wavelengths ranging from 30-meter to 0.003-meter, so here we focus more on the scintillation that happens in the strong regime, which can be further divided into the diffractive interstellar scintillation (DISS) and refractive

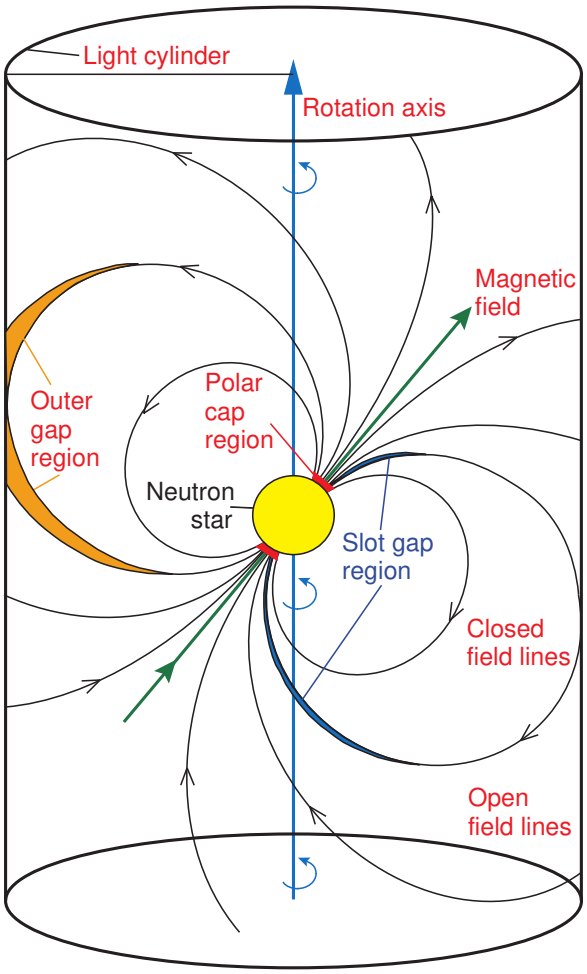

Figure 1.2: Geometry of emission of a pulsar, adapted from The MAGIC Collaboration et al., 2008

interstellar scintillation (RISS). The former is caused by the small scale of fluctuation in the ISM due to the diffractive scattering which creates constructive and destructive interference patterns in the dynamic spectra of the signal due to the multi-path propagation. This in particular causes a small variation of the arrival time of pulses because of the changes of the frequency structure and eventually broadens the pulse. The latter is caused by the refractive effect of the ISM on a much larger scale and eventually causes a long-timescale drift in the observed flux density. The flux will be modulated with a relatively low amplitude compared to DISS, over a longer time scale, such as months. This fluctuation can be analyzed in the auto-correlation of the dynamic spectra of the signals. As pulsars and fast transients are compact sources, so they are strongly affected by the scintillation and temporal broadening hence making it hard to detect. Strategies for searching these sources are dividing observation into multiple sessions(Cordes and McLaughlin, 2003) or carrying out the observation in higher time and frequency resolution with wide-band receivers.

Profile An individual pulse profile records the brightness variation through time when the emission beam of a pulsar sweeps across the observer. As illustrated in Figure 1.4, the data of the pulsar

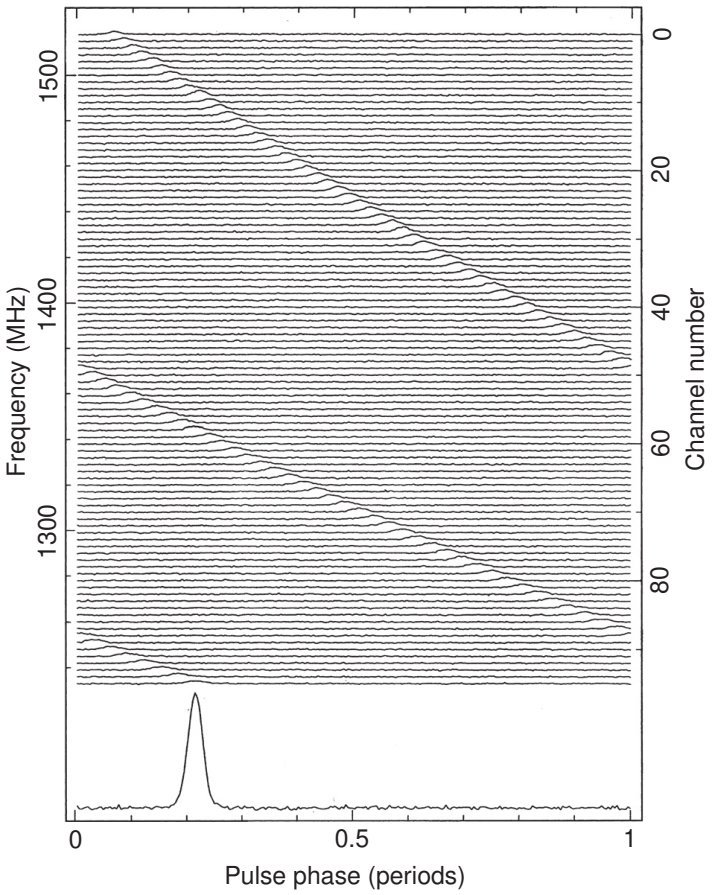

Figure 1.3: Dispersion measure. (Lyne and Graham-Smith, 2012)

observation are folded according to its period so that the S/N can be increased. Although for the majority of pulsars, their individual pulses are highly variable, the integrated or averaged profile of an observation is relatively stable. A high S/N profile is important for the timing which could further increase the precision of the period and place constraints on other derived properties. A change of the profile usually indicates a change of the emission state or current re-distribution events in the magnetosphere (Wang, Manchester and Johnston, 2007).

Different types of Pulsars

Pulsars can be divided into different classes depending on certain criteria. There are recycled pulsars and non-recycled pulsars depending on whether they go through a recycling process (more detail in Section 1.2.1). There are pulsars in binary systems or isolated pulsars according to the existence of companion stars. There are rotation powered, accretion powered and magnetic field decay powered neutron stars according to the source of energy. There are normal pulsars and magnetars according to the strength of the magnetic field. A period versus period derivative diagram as illustrated in Figure 1.5 provides an overview of pulsar of different classes.

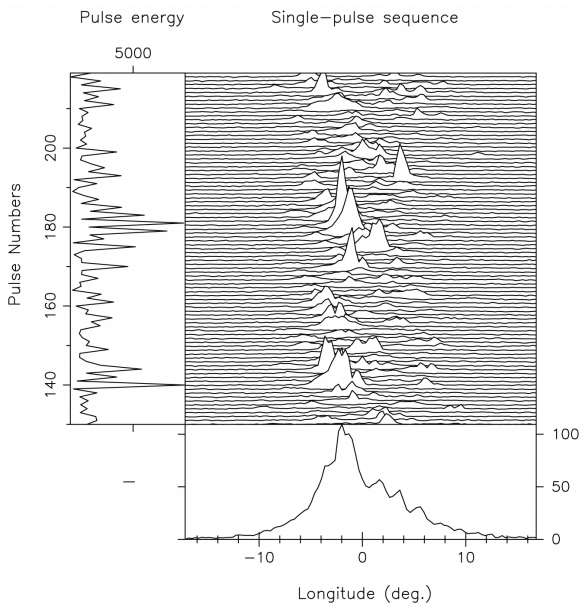

Figure 1.4: Pulsar Profile Folding (Deshpande and Rankin, 1999)

Millisecond pulsars Recycled pulsars with periods no more than several tens of milliseconds are usually called "millisecond" pulsars (MSPs). A pulsar's magnetic field gets weaker through time to a point that it can no longer produce detectable emissions (they move to the bottom right corner of the $P - \dot{P}$ diagram). In the formation scenario of MSPs, some of these pulsars accrete material and receive the angular momentum from their companion stars, and the pulsar spins up and its period reaches millisecond scale (Bhattacharya and van den Heuvel, 1991), a process known as "recycling". There are isolated MSPs as well, indicating that their companions might have been destroyed or that the pulsar was ejected from a globular cluster. The most important feature of an MSP is that its short period is extremely stable which opens possibilities for many scientific applications.

The stable period allows high precision measurements of its orbit. For example, Taylor and Weisberg (1982) discovered that the orbital decay of the PSR B1913+16 binary system was consistent with the prediction of the general relativity, making it the first detection of gravitational wave emission. Since then MSPs have been excellent laboratories for testing gravitational theories.

For an even higher requirement in precision, such as directly searching gravitational waves, an array of well-timed MSP can be correlated to form a pulsar timing array (PTA, Foster and Backer, 1990). Compared to laser-interferometer based approaches like LIGO (Abramovici et al., 1992), PTAs have much larger physical extent thus are more sensitive to gravitational waves of lower frequencies in the range of $10^{-9} \sim 10^{-7}$ Hz, such as those emitted by supermassive blackhole binaries (e.g. Moore, Cole and Berry, 2015). These kinds of systems are likely to exist in the center of galaxies, hence it provides a unique possibility to study the evolution of the supermassive blackholes and the formation of galaxies (e.g. Shannon et al., 2013; Tiburzi, 2018). Currently, there are observation campaigns carried out by North American Nanohertz Observatory for Gravitational Waves (NANOGrav, Jenet et al., 2009), European pulsar timing arrays (EPTA, Kramer and Champion, 2013), Parkes pulsar timing arrays (PPTA, Manchester et al., 2013), "MeerTime" with the MeerKAT (Bailes et al., 2020) and the Chinese Pulsar Timing Array (Lee, 2016). Meanwhile, the International Pulsar Timing Array

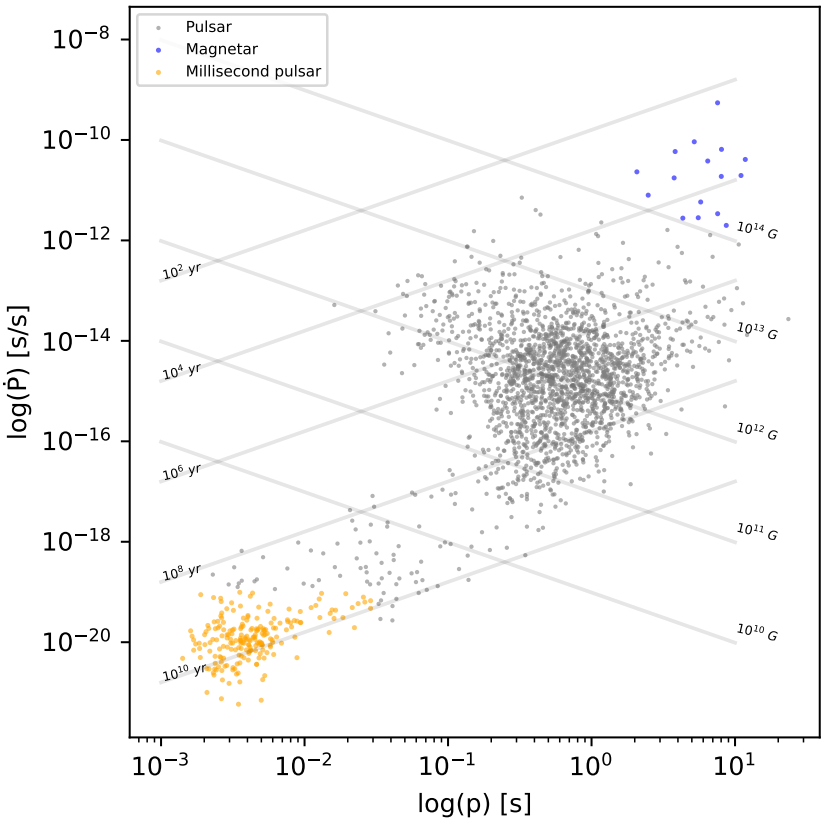

Figure 1.5: The $P - \dot{P}$ diagram showing the pulsars of different types. The normal pulsars are marked with grey dots. Here we consider pulsars with surface magnetic strength larger than 10^{13} Gauss as magnetars marked with blue dots. We also consider pulsars with periods $P \lesssim 30$ milliseconds and period derivatives $\dot{P} \lesssim 10^{19}$ s/s as millisecond (recycled) pulsars marked with yellow dots (Lorimer, 2008).

(IPTA, Manchester and IPTA, 2013) is aiming to join the efforts of different PTAs.

The millisecond binary system itself is a laboratory of great interest for binary stellar evolution. There are binary systems of a pulsar with a very low mass companion (black widow), systems with short orbit periods (redbacks), a triple stellar system containing an MSP (Archibald et al., 2018) and so on. These systems deviate from the normal millisecond pulsar binary systems, indicating potentially different formation scenarios and evolution paths.

Globular cluster Globular clusters (GCs) are groups of a large number of stars spherically and compactly bounded by gravity. They are considered to be formed from protoglobular gas clouds in the early stage of the Galaxy before the galactic disk was formed (Peebles and Dicke, 1968). This indicates the stars in the cluster are considerably older relative to the age of the galaxies. They are common in the Galaxy and there have been about 150 GCs discovered in the Milky Way. In Particular, they are abundant in the Galactic halo, orbiting the center of the Galaxy.

Because of the age and mass density of GCs, the properties of their pulsar populations is significantly different from those in the Galactic plane (Freire, 2013). For example, the majority of the population

is very old as expected due to the age of the GC itself. Moreover, the high stellar density leads to a density of pulsars that is several orders of magnitude larger than found in the Galactic disk. Most of the discovered pulsars in GCs are MSPs that are expected to have gone through the recycling process. There are also special binary systems that can possibly only be found in GCs because the large stellar density promotes frequent interactions (Ransom, 2008). This includes binaries with irregular ellipse and erratic timings. There are also systems with high eccentric orbits possibly produced during multiple stellar interactions or exchange encounters with nearby objects. These MSP and special binary systems are valuable in testing gravitational theories and studying stellar and binary evolution. Searching for pulsars in GCs requires high time resolution and high sensitivity instruments. The new MeerKAT telescope is the most sensitive telescope in the Southern Hemisphere which makes it an ideal instrument to perform high time resolution pulsar searches on GCs. A detailed demonstration and discussion of a beamformed observation on the 47 Tucanae GC with MeerKAT will be presented in Chapter 3.

Exotic pulsars and systems Some pulsars are distinguishable by their existence in a peculiar orbital system or their abnormal mass and so on. Unusual features can reveal information on the pulsar's structure and formation or make them good laboratories for specific physics experiments. It is normal to find pulsars in a binary system with a companion of a main sequence star or a white dwarf, while in the rare triple system PSR J0337+1715, a millisecond pulsar is orbiting with two white dwarfs. The formation of such a system has brought challenges to the current understanding of stellar evolution and provides unique evidence for the study of the "common envelope" evolution of a binary system (Tauris and Heuvel, 2014).

Relativistic Binaries are binary systems in which collapsed or degenerated objects are brought into an ultra-compact orbit as a result of stellar evolution. The decay of their orbits could be a source of gravitational waves. Antoniadis et al. (2013a) has observed and measured the orbital decay of the pulsar J0348+0432 and its companion. The result matches the expectations from general relativity and successfully ruled out several alternatives. Moreover, the work of Kramer et al., (submitted) uses the Double Pulsar PSR J0737-3039A/B to perform various tests on Strong-field gravity, achieving large improvements in the measurement of the relativistic effects of this system . Particularly, these tests reveal for the first time, the high-order effects of light propagation in strong gravitational fields, which is currently not testable in other methods. The best tool yet to be found to test the theories of gravity would be a pulsar-blackhole system as it allows the tests of the general relativity in the strong field limit (Kramer, 2004). However, these systems are rare and hard to search for, because of their extreme companions and environments. Their signals are not easy to model due to the higher order orbital derivatives or the potential for high ellipticities which makes them less sensitive to Fourier-based searches. An extra dimension of acceleration calculation should be performed during the search.

Magnetars A magnetar is a young and isolated pulsar powered by the decay of its ultra-strong magnetic field. They were first discovered by X-ray observatories thanks to their strong X-ray and soft gamma-ray emission. The magnetar model has successfully explained the spin-down rate of the soft gamma ray repeaters (SGR) and anomalous X-ray pulsars (Thompson and Duncan, 1995). Despite being young neutron stars, their periods are rather long, adding another mystery to their formation process which is still not fully resolved. A few magnetars have been found to manifest radio emission (e.g., Kramer et al., 2007) and some radio pulsars with high strength of magnetic field

have been observed to emit magnetar-like bursts, indicating there may be a similarity between them. There are proposals suggesting that the giant flares of the magnetars could be the progenitor of the bright, millisecond long and extragalactic fast radio bursts. This is supported by recent observation (CHIME/FRB Collaboration et al., 2020).

Pulsar emission mechanism

The radio emission mechanism is still poorly understood, 50 years after the discovery of pulsar. The major difficulties are to explain the mechanism to generate enough coherent radio emission to account for the detected brightness. After the discovery of pulsars, Goldreich and Julian (1969) modelled the electrodynamics of a pulsar as a magnetic dipole field with the surface surrounded by plasma instead of a vacuum proposed by Deutsch (1955). This is because the parallel electric field of the rotating neutron star is so strong that it surpasses the gravitational field, drawing the charged particle from the pulsar surface, producing a magnetosphere. However, this model neglects the effect of the plasma and the residual field, which means in the global structure of the magnetosphere, the magnetic and electric fields are balanced, i.e. the so-called "force-free" solution. This does not represent a realistic pulsar scenario as a residual parallel electric field is required to accelerate particles to produce the observed magnetosphere radiation.

The residual parallel electric fields were thought to exist in the distorted or non-closed regions of the global force-free structure. These regions often have a depletion of plasma and are referred to as "gaps" in the magnetosphere, where particles can be accelerated and multiplied. The gaps are often close to or bounded by an important geographic structure called "light cylinder" (see Figure 1.2). It is an imaginary boundary centered at the rotation axis of the pulsar and has a radius of $R_{LC} = c\omega$, where c is the speed of light and ω is the angular velocity of the pulsar. The matter inside the light cylinder co-rotates with the pulsar while the magnetic field lines crossing the boundary are disrupted as they can not move at superluminous speed. The magnetic field lines of the pulsar are thought to come out near the north magnetic pole and re-enter near the south magnetic pole, while some of them remain open because they extend out of the light cylinder as illustrated in Figure 1.2. The region above the pulsar surface surrounded by the last open magnetic field lines is called the "polar gap" of the pulsar.

Polar gap Because the field lines within the polar cap do not close, there exist residual electric fields which would be responsible for the observed radio emission. In the emission models suggested by Sturrock, 1971 and Daugherty and Harding, 1982, the particles near the polar cap are accelerated to relativistic speed by the strong residual electric fields and then move along the curved magnetic field lines. These relativistic charged particles emit curvature radiation or boost other photons via inverse-Compton scattering, resulting in high energy photons. If the energy of the photons is high enough, they would decay into pairs of electrons and positrons in strong magnetic fields. These newly created particles will again create high energy photons, repeating the same process. This cascade of pair production leads to an avalanche of plasma in the magnetosphere, creating the observed radio pulse profile. However, curvature radiation alone can not provide the necessary energy for the brightness temperature detected on earth. This is because the incoherent sum of the curvature radiation from the individual particles is not sufficient, a coherent radiation mechanism such as bunching (Gil, Lyubarsky and Melikidze, 2004), reactive instability (Asseo, Pellat and Rosado, 1980) and maser emission (Luo and Melrose, 1995), (Lyutikov, Blandford and Machabeli, 1999), is required.

Outer gap The polar cap is not the only "Gap" in the pulsar magnetosphere. According to Goldreich and Julian (1969), the pulsar magnetosphere is divided into four sectors with the plasma of opposite sign and separated by a null line or null surface where the plasma charge density (PG density) is zero. The region between the null charge line, the last (outermost) closed field line and the light cylinder is called "outer gap" (Cheng, Ho and Ruderman, 1986). The plasma of this region is depleted because they travel through the open field lines and cross the light cylinder therefore can not be compensated. The particles inside this region are accelerated by the residual electric field to emit curvature radiation. However, unlike the situation in the polar cap, the magnetic field in this region is much weaker, the particles will not go through a cascade of massive magnetic multiplication. Without a strong magnetic field, the particles are accelerated to a high energy state near the light cylinder, producing gamma-ray photons. Then the gamma-ray photons could create primary pairs by colliding with the X-ray photons from the surface. In this sense, the outer gap could be more responsible for the observed high energy emission from pulsars.

Slot gap "Slot" gap is another region that could accelerate particles and account for the observed wide pulse profiles. Though the polar cap model can possibly explain the observed radio pulse profile, it is challenged by some observed wide profiles in the high energy emissions as the polar cap should produce small emission areas. The slot gap model was originally proposed by Arons and Scharlemann (1979) then revised by Muslimov and Harding (2003), it describes a narrow region between the last open field line and the outermost closed field line where the electric field is low. The particles inside this region are slowly accelerated upward before they reach a high Lorentz factor. Therefore, the pair production does not occur near the surface of the pulsar, but at a much higher altitude as illustrated in Figure 1.6. The cascade of pair production around the slot gap will form a board "ring" shape beam in the line of sight or a hollow-cone beam centered at the magnetic pole. The high energy photons emitted by the high Lorentz factor particles or pair production at this high altitude hollow-cone beam could explain the width or peaks of the high energy pulse profiles (Harding et al., 2008).

Current sheet In recent decades, numerical simulation has become increasingly important in studying the global force-free magnetosphere. The plasma-filled magnetosphere model by Goldreich and Julian (1969) laid the foundation for numerous later models, it is of significance to verify quantitatively if such magnetosphere solution is viable or it indeed provides the necessary plasma density to produce the observed pulses. For example, Contopoulos, Kazanas and Fendt (1999) presented the first numerical solution of the structure of an axisymmetric force-free magnetosphere of an aligned rotating magnetic dipole, Spitkovsky (2006) proposes a numerical method for the solution of equations of force-free relativistic Magnetohydrodynamics (MHD), Chen and Beloborodov (2014) uses the "particle in-shell" (PIC) to study the evolution of the pulsar magnetosphere and put various gap models to test. In these numerical solutions, the existence of structures called "current sheets" plays an important role in producing the observed emission. They are created by the flows of the charged particle accelerated by the twisted or reversed magnetic field lines. Located at a Y-point among the closed co-rotating region, the edge of the polar cap and the light cylinder. The current sheet inside the light cylinder is called the "separatrix current sheet" with a negative charge and the one that extends far outside the light cylinder is called the "equatorial current sheet" (ECS) with a positive charge as illustrated in Figure 1.7. The positrons are accelerated to high Lorentz factors by the re-connection of the magnetic field in the ECS and emit curvature radiation. Philippov et al. (2019)

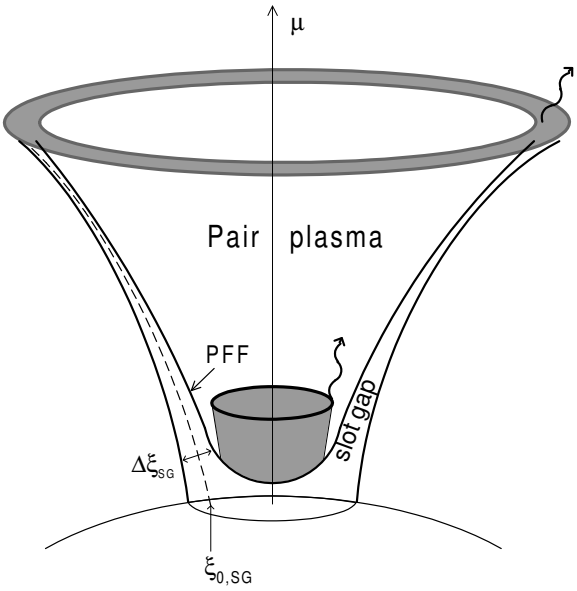

Figure 1.6: Slot gap model (Muslimov and Harding, 2003).

has proposed that the radio emission could be generated in the ECS by the merger of the plasmoids. During the re-connection events, the current surface is broken up into a series of plasmoids (Figure 1.8 a), they merge with each other to produce larger ones. New current sheets perpendicular to the ECS form in the merging of these large plasmoids (Figure 1.8 b). These unstable perpendicular current sheets could also break into secondary plasmoids. Both plasmoids in two sheets could be accelerated to relativistic speed and collide with each other or with the magnetic fields, emitting strong electromagnetic waves.

These plasmoids mergers would also create bright individual pulses. The intervals of the radio waves emission in these mergers are consistent with the timescale of the "nanoshot" observed in Crab pulsar (Philippov et al., 2019). A similar model proposed by Lyubarsky (2018) suggested that the coalescence of magnetic "islands" in the current sheet would be responsible for the observed giant nanoshots. These mechanisms will be discussed further in Chapter 5. The abovementioned giant nanoshots are related to the "giant pulses" observed in some pulsars.

Giant pulses

Apart from stable average profiles, we sometimes see individual pulses that are brighter than the average pulse by a factor of 10 in flux density or energy, which are called "giant pulses" (GPs). Beyond their brightness, GPs detected from different pulsars share similar observed properties, such as their narrow widths (Hankins et al., 2003, Kinkhabwala and Thorsett, 2000) and their flux density distribution.

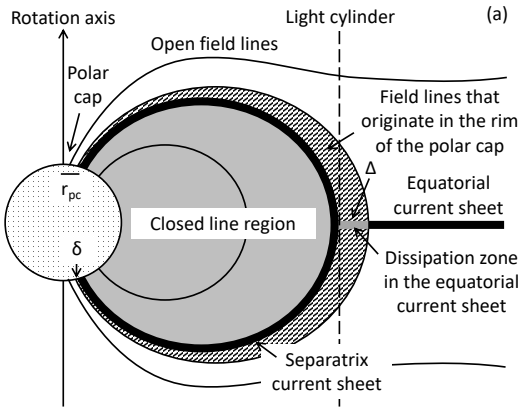

Figure 1.7: Current sheet. (Contopoulos, 2019)

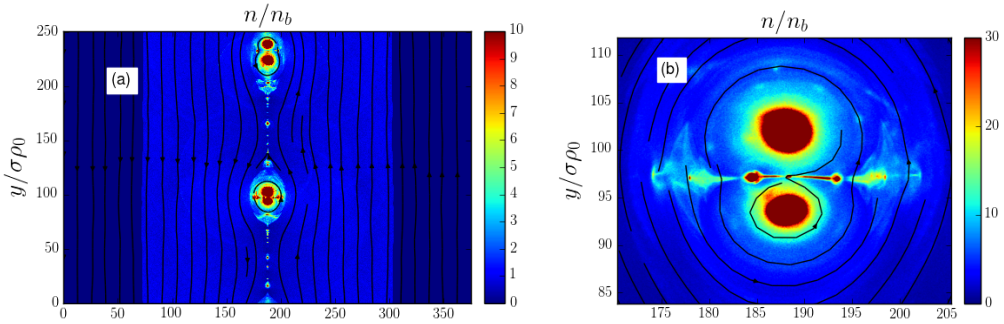

Figure 1.8: Plasmoids along the current sheets. (Philippov et al., 2019)

Unlike typical pulses that have approximately normal or log-normal flux density distributions, giant pulses appear to follow a power law.

Though they have been studied for more than a decade, the origin of these GPs is still unknown. Some of the giant pulse emitter shares similar features such as high magnetic fields at the light cylinder (Cognard et al., 1996) and high energy emission (Romani and Johnston, 2001a). If this correlation is secure, we would stand to gain a clearer understanding of the mechanism of pulsar radiation and set constraints on emission models, which are still elusive despite decades of intense observation and study. However, only a dozen pulsar have been found to emit GPs. The scarcity of GP emitting pulsars is problematic if we wish to perform a robust statistical analysis of this phenomenon. As such, there is a pressing need to increase the sample size. While increasing the sample size of giant pulse emitters is important to understand their emission mechanism, strengthening the association to gamma-ray pulsars is interesting for another reason. If the latter holds, it is plausible that radio-quiet gamma-ray pulsars may emit occasional giant radio pulses, thereby providing an alternate distance estimate to these pulsars using galactic electron distribution models (YMW16, Yao, Manchester and Wang, 2017; NE2001, Cordes and Lazio, 2002). Apart from their own mystery, GPs from nearby galaxies are also been suggested as origins of Fast Radio Bursts (FRBs). I submitted an observing proposal to the Effelsberg radio telescope for a few pulsars that have the potential to emit giant pulses. The result will be presented in Chapter 5.

Pulsar searching

Fourier methods are the primary approach to search for regular pulsars. That is due to the fact that we do not know the periods of the pulsars beforehand and without them we can not fold the data. The individual pulses of a pulsar are usually very weak and swamped by the noise. To detect most of the pulsars, it is necessary to fold the data with the period of the pulsar to increase the S/N of its profile. The Fourier technique will transform the data from time domain to frequency domain in which we can obtain and inspect the harmonics pattern of the data. Once the periodic information of the data is extracted, we can use them as the potential periods of the pulsar to fold the data.

Single pulse search is a method for searching pulsars with irregular emission patterns and transient events. The Fourier method is not sensitive enough to some pulsars because of their sporadic emission or period changes in extreme binary systems. Single pulse search techniques usually convolute the de-dispersed data with a match-box of various sizes to pick up the spikes in the time series, I will talk about it in more detail in Chapter 5.

1.2.2 Fast Radio Bursts

Fast radio bursts are bright millisecond radio bursts with dispersion measures exceeding the maximum value expected from the Milky Way in given line of sights. They were first reported by Lorimer et al. (2007) in a single pulse search on archival data targeting the Small Magellanic Cloud (SMC). One beam in the 13-beam receiver of Parkes telescope was saturated by the brightness of the burst which made it hard for further localization. The burst was detected with a DM of 375 cm^3 pc which greatly exceeded the galactic contribution of 25 cm^3 from this light of sight according to the NE2001 model (Cordes and Lazio, 2002).

To date, there are about 500 published FRB discoveries[1] (Petroff et al., 2016a; The CHIME/FRB Collaboration et al., 2021a). Nearly 20 of them have been found to repeat (Spitler et al., 2016; The CHIME/FRB Collaboration et al., 2021a). More than a dozen have been localized to host galaxies[2] (Heintz et al., 2020). Most of the progenitor theories invoke compact objects. We group the theories according to their ability to repeat assuming not all FRB repeats.

Compact objects' energetic emission or their interaction with other objects could produce FRBs. There are theories (Lyutikov, Burzawa and Popov, 2016) that propose FRBs are giant pulses from extra-galactic pulsars. Others propose the bright pulses from a young millisecond pulsar in a dense environment could be responsible for the observed phenomena. Recently, FRBs being the flares of magnetars has gained observational support (CHIME/FRB Collaboration et al., 2020; Bochenek et al., 2020). FRBs could also be the energy release of the interaction between compact objects or surrounding medium such as neutron stars and black holes (Zhang, 2017), neutron star and accreted material from a companion (Gu et al., 2016). These events all have the potential to repeat.

The massive energy released in cataclysmic events could also be the origin of the one-off FRBs. Such events could be super-massive neutron stars collapsing into black holes (Falcke, Heino and Rezzolla, Luciano, 2014), neutron star mergers (Totani, 2013) or neutron star black hole mergers (Liebling and Palenzuela, 2016).

FRBs provide us with a new approach to study the Universe on large scales. Because of the large DM of FRBs, one can track the ionized component of the baryonic matter in the inter-galactic medium

[1] http://www.frbcat.org
[2] http://frbhosts.org

(IGM) at a cosmic distance which helps to study the "missing baryons" mystery and test cosmological models (Macquart et al., 2020a). This is possible if we have a large population of localized FRBs with measured redshifts, which is why one of the most important aspects of current FRB studies is the positive association of the source with a host galaxy with an independent redshift estimate. Similar to DM, a quantification of the Faraday rotation experienced by the polarised signal as it propagates through the parallel magnetic field, called the rotation measure (RM), contains the contribution of the magnetization information from the Galactic medium, the inter-galactic medium and the host environment of FRBs. Therefore, a population of FRBs in different directions and distances will serve as a map or a probe of the magnetization in the universe.

The search method of FRB is similar to the single search pulse search method of pulsar with some consideration. However, due to the fact that most of the FRBs have not been observed to repeat in the follow-up observation, we must tune the observational strategies for capturing one-off events. The more field of view the telescope has, the larger possibility it has for capturing FRBs assuming there is no preferred direction for FRBs and that they are seemingly isotropically distributed. To study the properties of FRB requires the detected samples to be preserved in high time and frequency resolution because the signal is likely from other galaxies thus usually strongly dispersed. This relies on the real time searching capacity of the observational instruments. For example, the computational power to search for candidate pulses over a wide range of DMs in real time and a large transient buffer, an in-memory ring buffer that stores a snapshot of the raw voltages, are crucial for retrieving the full time and frequency resolution of the burst in the event of detection. A rapid localization scheme is also important to associate the sources.

1.3 Search fast transient with Interferometry

1.3.1 Interferometry

Introduction

Interferometry in astronomy observations is a class of methods that obtains the power pattern of the sky by coherently combining the response of multiple receiving elements. In radio regime, it allows one to measure and manipulate the property of interference between wave-like radio signals from individual antennas. This method excels in achieving high spatial resolution observations. Every pair of elements in an array can form a baseline that measures the combined response of these two elements to the sky. This response is the convolution between the power distribution of the sky and the interferometric pattern of the two elements. According to the definition of angular resolution $\theta = \frac{\lambda}{D}$ where λ is the wavelength and D is the separation of the receptors, each response has the resolving power on par with a single dish telescope with the diameter of the length of the baseline D. This method allows an array to achieve a spatial resolution that is generally not practical for single dish telescopes.

Development of interferometry

Since the birth of astronomy, the drive to achieve higher spatial resolution has never ceased. Pawsey and McCready were the first to use interferometry in radio astronomy. In 1946, they built a Sea Interferometer, using the surface of the sea as a reflector to create interference (McCready, Pawsey

and Payne-Scott, 1947). Almost at the same time, Martin Ryle built the first multiple-element radio interferometer to mimic a much larger telescope. This instrument served as a prototype for later interferometric arrays, laying the groundwork for modern radio interferometry. Following this, the separation of the telescopes in interferometric arrays became even larger. From the radio-linked interferometry that connects telescopes hundreds of kilometers apart (see e.g. Davies, Anderson and Morison, 1980), to Very-Long-Baseline Interferometry (VLBI) that utilizes telescopes on different continents and finally to space-based interferometry, the resolving power of interferometric instruments has increased by multiple orders of magnitude since their inception. Along with the development of the instruments, the strategies and software for interferometry were also evolving. For example, the adoption of aperture synthesis increases the variety of the baselines by sampling the source at different times through the rotation of the Earth, the CLEAN (Högbom, 1974) and self-calibration algorithms greatly improved the fidelity of the image.

Major achievements of radio interferometry

Interferometry has played an important role in the discovery of Quasars. A series of interferometric experiments were carried out in late 1950 to survey the radio sky. The instruments consist of the Lovell telescope and several small portable telescopes. They moved the small telescopes to gradually increase the baselines in order to resolve objects. In doing so they discovered that two sources (3C 48 and 3C 273) have very small angular sizes. These objects later were localized and identified by optical telescopes and given the name “Quasars”. They were subsequently classified as Active Galactic Nuclei (AGN) which is very important for the study of the evolution of galaxies. Today, interferometry still is the only solution when scientists tried to resolve the detailed structure of AGN.

Interferometry is indispensable for the localization of FRBs. In the development of progenitor theories of FRBs, one crucial factor is the association of the host galaxy, which provides environmental information of the progenitor. This brings challenges in most of the FRBs events because it requires the instrument has the ability to localize them within arc seconds in the event of detection, with which single dish telescope seldom provides. This was first achieved by Bannister et al. (2019) with ASKAP, an SKA pathfinder in Australia.

Interferometry has enabled the first ever image of a black hole. Theoretical models predict that photons captured near the radius of a non-rotation Schwarzschild black hole will appear to be a bright emission ring to distant observers. Within this photon capture radius, the photons can not escape, thus the black hole and the event horizon appears to be a black shadow within a ring. The expected diameter of the event horizon structure of M87* is around 40 microseconds which should be detectable by VLBI. The Event Horizon Telescope collaboration assembles a global VLBI array consisting of observatories from six locations around the world with baselines up to 10700 kilometers, achieving a resolution of 25 microseconds. Event Horizon Telescope Collaboration et al. (2019) has successfully imaged the black hole with multiple independent data sets and different imaging techniques. The result is similar to the simulation and the derived mass estimation is also consistent with the Kerr black hole metrics. The direct image of a black hole made by interferometric techniques has provided us with a new tool to study gravity.

Advantages of interferometry

Interferometers have many advantages over single dish telescopes from the perspectives of the resolution, mechanical complexity and RFI resilience.

High resolving capacity It is indispensable to use interferometry in the study of the detailed structures of the AGN (Boccardi et al., 2017), the central black holes in other galaxies (Fish, Shea and Akiyama, 2020) and its surrounding stars, the star and planet formation (ALMA Partnership et al., 2015), the gravitational lensing events (Hezaveh et al., 2016), searching and locating for fast radio transients (Chatterjee et al., 2017) and so on.

Low mechanical complexity, flexible and inexpensive Building an interferometric array tackles a much lower mechanical complexity compared to large single dish telescopes and it is flexible, easy to scale up. Increasing the aperture of the dish was once the easiest approach to increase the sensitivity of the telescopes. However, the cost and difficulties of designing and constructing the supporting structures, the servo system and the active optical system go up steeply as the aperture increases. The state-of-the-art large single dish telescopes have compromised their steering capability by putting the dish on a non-movable topography. They are also expensive to upgrade or modify as a whole instrument. Furthermore, no observation can be made during the maintenance of the telescopes. Modern interferometric array usually consists of a large number of small antennas which are highly modular and are relatively inexpensive. Apart from the benefit of the high spatial resolution thanks to the long baselines, the coherent combination of the response from them could obtain a sensitivity on par with or larger than a single dish telescope. In the perspective of flexibility, the individual antennas of an array can be small steerable telescopes or numerous non-movable receptors with electrical steering capability or even a combination of them both. Different subsets of the array can be allocated and operated independently so that the array can be configured to meet wide and diverse science cases. Individual antennas can be put offline for maintenance without interrupting the observation.

RFI resilience Interferometry is good at resisting self-induced RFI. Because the self-induced RFI from individual antennas are often not correlated, they are destructively suppressed while the gain of the individual receptors are constructively combined during the stages of coherent summing. For external RFI such as inference from satellite passing, the adverse effects are lesser when the distances between receptors are larger. That is because the larger differential delay correction for each receptor leads to a stronger decorrelation of signals not in the synthesised beam. (Thompson, 1982)

Challenges of interferometry

Phase correction The challenges of modern interferometry come from its computing complexity. Because of the geometric separation of the interferometry elements, the signals from individual antennas are out of phase. It is crucial to precisely correct the phase differences before combining the signals so that coherence is achieved.

Data volume The need for constant phase correction or correlation has brought challenges to high time and frequency resolution observation with a large number of antennas. The situation will further escalate when real time searching and detection is required as the computing system needs to equip

with a large amount of memory and high speed computing units. It also brings pressure to the offline data reduction process if raw data is required. These two difficulties have been largely alleviated in the recent decade thanks to the fast development of high performance computing units, wide adoption of parallel computing techniques and affordable storage equipment.

Variable sky pattern The power pattern of an interferometric array is highly variable. The product of an astronomical observation is the convolution of the power pattern of the instrument and the actual sky power pattern. Usually people try to de-convolve the product to obtain the original power pattern of the source. However, unlike single dish telescopes whose power patterns are largely consistent between observations, the power pattern of an interferometric array changes constantly with the position of the source due to the changes of the projected baselines. This requires accounting for the power pattern of the instruments while carrying out the observation and performing data analysis.

1.3.2 Observation method of interferometric array

The general approach of interferometry is to combine the responses from receiving elements with different geometry separations so that the power pattern of the sky can be sampled in different scales. In the meantime, the combination needs to be coherent to preserve the sensitivity. There are generally two implementations for this purpose.

Correlation

One method is to perform an inverse Fourier transform on responses of baselines. During the observation, every antenna in the array samples the sky individually with precise timestamps. In the meantime, each antenna pairs with any other antenna in the array to form baselines. The baselines are analogues to a number of single dish telescopes with different apertures. Data of two antennas that belong to the same baseline are correlated to create a "visibility", a quantitative description of the interference response pattern between these two antennas. After the observation, the magnitudes of the visibilities are gridded by their projection location to the source inside a UV-plane which is a measurement of the lengths of the baselines in wavelength. The inverse Fourier transform performed on the UV-plane produces a point spread function (PSF) which is a convolution product of the actual power distribution on the sky and the interferometric pattern of the array. Finally, the power pattern on the sky can be obtained by de-convolution. In this method, a large field of view can be achieved in a single pointing.

Beamforming

The other method is to align and sum the voltages from individual antennas to form highly directional spatial responses, termed as beams. During the observation, every antenna in the array samples the sky individually with precise timestamps. The times of arrival of the radiation from a position in the sky to each individual antenna is different due to their geometric separation. These differences are calculated referring to a shared reference in order to align the data of each antenna temporally. After the alignment, the voltages from all antennas can be summed coherently, forming an electrical beam, pointing to the above-mentioned sky position with the resolution of the largest separation and the sensitivity of all antennas combined. This procedure can be performed simultaneously to create

multiple beams for different positions in the sky. This method can achieve high time resolution for a limited number of beams.

1.3.3 Current interferometry arrays and fast transient surveys

The current actively used interferometries are listed in table 1.1 with characteristic properties. The

Table 1.1: List of modern interferometers. The "versatile" in array type means that the elements are steerable single dish antennas, the "PAF" is similar to "versatile" with additional phased array feeds built-in, the "uni-direct" means they are non-movable all-sky antennas and "sub-/milli" means that the antennas observe in the sub-millimeter band.

Name	Element	Longest baseline (km)	Collecting area (m^2)	Array type	Bandwidth (MHz)	Frequency (GHz)
VLA	27	36.4	13253	versatile	1024 - 2048	0.058 - 50
ATCA	6	6	2280	versatile	2048	2.1 - 95
uGMRT	30	30	47713	versatile	400	0.13 - 1.4
MeerKAT	64	8	9160	versatile	864	0.58 -3.5
SKA-Mid	188		33222	versatile		
ASKAP	36	6	4072	PAF	300	0.7-1.8
Apertif	14	3	6872	PAF	300	1-1.75
CHIME	256	100	8000	uni-direct.	400	0.4-0.8
Lofar	52, 76	1000	300000	uni-direct.	60	0.01-0.24
LWA	13000	400	1000	uni-direct.	78	0.01-0.088
MWA	4096	2.864	2752	uni-direct.	30.72	0.07-0.3
UTMOST	7744	0.778	18000	uni-direct.	30	0.843
ALMA	66	16	7000	sub-/milli	8000	40-950

recent and ongoing fast transient surveys with their primary goals are listed in Table 1.2.

1.4 About this thesis

This thesis is organized in 6 chapters. The introduction chapter is followed by Chapter 2, which discussed the requirements of fast transient surveys and how beamformed observation try to meet them with MeerKAT as an example. Then Chapter 3 presents the concepts of the beamforming techniques on modern radio interferometers and the corresponding observational strategies to tackle the challenges. A practical beamformed observation on 47 Tucanae was carried out and evaluated using the mentioned techniques. After that, Chapter 4 reviews the various applications of the MeerKAT beamforming platform in different transient surveys. Next in the thesis is Chapter 5 dedicated to a search of giant pulses with the Effelsberg telescope to investigate the relationship between high energy emission and giant pules. Finally, Chapter 6 is the conclusion of this thesis.

Table 1.2: List of recent and ongoing fast transient surveys

Name	Interferometer	Description
LOTAAS	LOFAR	The LOFAR Tied-Array All-Sky Survey is a northern sky survey centered at 135 MHz to search pulsar and fast transient.
CRAFT	ASKAP	The Commensal Real-time ASKAP Fast Transients survey is a high time survey to search for fast radio transient between 700 and 1500 MHz.
realfast	VLA	The Real-time, Commensal Fast Transient Surveys is a high time and spatial resolution survey to search fast transient by searching the image created in real time.
TRAPUM	MeerKAT	The Transients and Pulsars with MeerKAT is a high time resolution survey to search pulsar and transient focusing on globular clusters, Galactic center and extra-galactic regions at L-band and S-band.
CHIME FRB project	CHIME	The CHIME Fast Radio Burst Project searches FRBs in real time and performs simultaneous pulsar timing with high time and frequency resolution at 800 MHz.

CHAPTER 2

Fast transient surveys with Interferometers

Single dish telescopes face many challenges when they come to carrying out large-scale fast transient surveys. As mentioned in Chapter 1.2, millisecond and shorter timescale radio bursts are of high interest, but their sporadic or even one-off occurrence makes them particularly hard to detect and localize. To increase the possibility of detection, it is better to use an instrument having a large field of view, high sensitivity and high frequency and time resolution. To maximise the science from each detected burst, a high spatial resolution to localize the source is also important. Though large single dish telescopes currently have the highest sensitivity, they lack field of view as these two properties are reciprocal for single dish telescopes. This rule is also applicable to the individual elements of an interferometer, but with the use of additional computing power, individual elements can be combined to construct an instrument with the field of view of a single element and the sensitivity of all elements combined.

Contents

2.1 Requirement of fast transient surveys

2.1.1 Time resolution

Fast transient surveys have a pressing need for high time and frequency resolution. For millisecond pulsars and Rotating radio transient (RRATs, McLaughlin et al., 2006), the pulse microstructure can be down to microseconds in scale (Hankins, 1971). Furthermore, extremely narrow giant pulse groups, containing individual pulse with timescale down to nanoseconds, have been detected from the Crab pulsar (Hankins et al., 2003). Hence, to explore the fast transient population as completely as possible, we need time resolution of the order of microseconds or sub-microseconds. From the telescope perspective, this requires a low-noise amplifier with wide bandwidth to ensure the time resolution is preserved after channelization. In the meantime, high time resolution increases the data rate of the observation, especially for interferometers with large numbers of receiving elements.

2.1.2 Frequency resolution

For the low frequency component of a broadband transient that is subject to frequency dispersion, high frequency resolution increases the detection possibility. This is due to the fact that without prior information about the sources being search for, a high number of de-dispersion trials are performed on the data with different DM values. This type of search is only efficient on data with high frequency resolution as during the de-dispersion process, the wider the channels the worse the intra-channel smearing that decreases the S/N of the signal, thus making it harder to detect. In other words, the frequency resolution is one of the factors that determines the depth of the search. However, for a given sampling rate, the time resolution of the data decreases as the number of channels increases, hence the number of channels should be carefully chosen according to the scientific goal.

2.1.3 Field of view

Wide field-of-view survey capability has become increasingly important in transient surveys. Bright transient bursts such as FRBs and giant pulses originated from other galaxies could be detected from Earth (McLaughlin and Cordes, 2003) and they could appear isotropically in the sky if the cosmological principle holds on the scales of the detectable population of FRBs. This scenario has been supported by the recent published population of the FRBs (Bhandari et al., 2018; The CHIME/FRB Collaboration et al., 2021a). Instruments with wide-field survey capability have a much larger probability of detecting extragalactic bursts which is a fact clearly demonstrated by CHIME (CHIME/FRB Collaboration et al., 2018)[1].

2.1.4 Spatial resolution

For extragalactic fast transients with unknown origins, localization is one of the keys to test progenitor theories. The early study of the FRBs was hindered by the coarse localization of the single dish telescopes. Their relatively low spatial resolution could not unambiguously associate the burst to a host galaxy (Lorimer et al., 2007), which makes it difficult to test progenitor theories. This situation has gradually improved with more and more interferometric observation such as Bhandari et al.

[1] https://www.chime-frb.ca/

(2020). Currently, most of the attempts at localization are performed on repeating sources as their re-occurrences allow different telescopes to be used. To improve the localization of the one-off events during a survey, real time high precision localization is required.

2.2 Beamformed observation

In recent decades, different beamformed observational techniques have been widely adopted to achieve both high sensitivity and high spatial resolution.

2.2.1 Multi-beam receiver and phased array feed

Multi-horn feeds and phased array feeds (PAFs) aim to increase the field of view of single dish telescopes by recovering signal across the telescope focal plane with an array of receiving elements. The multi-horn feed physically increases the viewing angle of the receiver while a PAF is making "electronic horns" over the focal plane. In most cases, they can be directly deployed on existing telescopes without significantly altering the structure of the telescopes and possess the same sensitivity if cryogenic cooling is equipped. Although with a PAF the localization of point sources can be improved by overlapping beams, the physical resolution does not increase, because the diameter of the telescope remains the same. Therefore, multi-horn feeds and PAFs are valuable upgrades for single dish telescopes, but they are not the most efficient instruments to perform fast transient searches that require both wide field and rapid arcsecond localization capability.

2.2.2 Beamforming with interferometric arrays

Beamformed observations with interferometric arrays have emerged to tackle the challenges of efficient fast transient searches. Beamforming is the process of combining the signals from an arbitrary number of receiving elements coherently to enhance the spatial response towards a particular direction. It enables interferometric arrays to form a large number of high temporal and spatial resolution coherent beams simultaneously at different sky positions. Coherency can be archived by compensating for geometric and instrumental delays to the signal received at each element. The compensation can be applied in either time domain or Fourier domain. Here I focus on approaches in Fourier domain as they can utilize the outputs from the F-stage (channelization) in an FX (First Fourier transform then correlation) structure backend illustrated in Figure 2.4, which is used by most modern interferometric telescopes. The implementation will be explained in detail in Chapter 3.

For the same sensitivity, beamformed observations have faster survey speed and higher spatial resolution given enough computational power to generate numerous electrical beams and the long baselines. They can also be easily re-configured to carry out different types of observations. The survey speed figure of merit for multi-beam interferometric surveys suggested by Cordes (2009) can be expressed as:

$$FoMSS = B\frac{N_{\mathrm{FoV}}\Omega_{\mathrm{FoV}}}{N_{\mathrm{sa}}}\left(\frac{f_{\mathrm{c}}A_{\mathrm{e}}}{mT_{\mathrm{sys}}}\right)^2 \tag{2.1}$$

where B is the bandwidth of the receiver, N_{FoV} is the number of synthesized beams, Ω_{FoV} is the field of view of a single synthesized beam, N_{sa} is the number of sub arrays, A_{e} is the effective area of the

entire array, f_c is the fraction of A_e that is available, m is the S/N detection threshold and T_{sys} is the system temperature.

According to equation 2.1, for a given interferometric array and time resolution, the survey speed figure of merit can be considered as a product of the beam number, the field of view, the square of the sensitivity of each beam and the receiver bandwidth. For wide-field fast transient surveys, one can use short baselines to form large beams to cover a large field of view while at the same time reduced bandwidth to lower the data rate to trade a higher number of beams. While for targeted surveys that need high sensitivity and high spatial resolution, one can utilize all the antennas or long baselines to create fewer but more sensitive, higher resolution beams. If a transient buffer is equipped, a voltage dump from the transient buffer can be triggered to preserve the raw time and frequency resolution in the event of detection. These raw voltages allow for subsequent processing such as secondary beamforming with longer baselines to improve the localization.

2.2.3 Complexity analysis

The observational instruments can perform beamforming in the Fourier domain on different kinds of data. Besides using raw-voltages, imaging the sky with "visibilities" (see Section 1.3.2) could also cover an excellent field of view and achieve high spatial resolution. It is useful to briefly discuss which is preferable and under which circumstances. Here we will look at "raw-voltage" beamforming using the channelised voltages from the antennas and visibility beamforming using the output of the correlator.

For this comparison, I assume an array of 44 antennas with an 856 MHz bandwidth, two polarisations and 8-bit data. To compare the computational cost, both approaches form 11442 beams or pixels to fill a field of view of 0.89 degree in diameter and integrate 22 samples for a time resolution of 105.271 microseconds. The memory pressure and operation count of these two processes can be calculated using the following equations:

$$M = \frac{BN_{\text{stream}}N_{\text{pol}}N_{\text{bit}}}{N_{\text{int}}} \tag{2.2}$$

$$C = \frac{BN_{\text{stream}}N_{\text{pol}}N_{\text{bit}}N_{\text{beam}}}{N_{\text{int}}} \tag{2.3}$$

where M is the memory pressure and C is the operation count, B is the bandwidth of the digitized data, N_{stream} is the number of antenna date stream or visibility data stream, N_{pol} is the number of polarizations, N_{bit} is the number of bits in one sample, N_{beam} is the number of beams or pixels to be generated and N_{int} is the number of samples to integrate.

For the raw-voltage method, the N_{stream} is N_{ant} and the integration happens outside the process. For the visibilities method, the N_{stream} is the number of baselines, thus $N_{\text{ant}} * (N_{\text{ant}} - 1)$ and the integration happens inside the process to lower the size of the visibility. Other than these differences, the rest of the parameters are the same for both methods. In this comparison the memory pressure is defined as the minimum memory requirement for the process, so the memory pressure ratio of the row-voltage method to the visibilities method $\frac{M_{\text{raw}}}{M_{\text{vis}}}$ comes down to $\frac{2}{N_{\text{ant}}-1}$. As it can be seen from the equation, the memory pressure of the raw-voltage method is always lower than the visibilities method if there are more than 3 antennas. The operation count is defined as the minimal number of operations needed to finish the process. The operation count ratio of the raw-voltage method to the visibilities method $\frac{C_{\text{raw}}}{C_{\text{vis}}}$ is $\frac{2N_{\text{int}}}{N_{\text{ant}}-1}$. This expression indicates that the ratio depends on the number of the antenna and

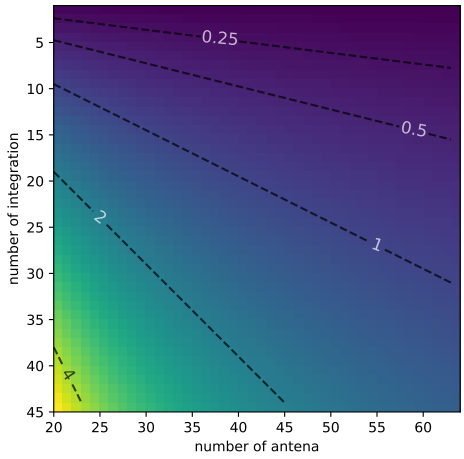

Figure 2.1: The ratio of the raw-voltage method to the visibilities method in operation count as a function of the number of time samples to be integrated and the number of antennas. Darker color means in that combination of integration and antenna, raw-voltage method requires fewer operations than correlation process does. The contour labeled as 1 indicates that in those combinations (e.g, 45 antennas and 22 integration), both processes have the same operation count.

the number of samples to be integrated as illustrated in Figure 2.1. The raw-voltage method has its advantage in operation count when the number of antennas goes up while the visibilities method catches up when the number of samples to be integrated goes up (e.g. when high time resolution is not required). These two scenarios indicate that these two methods are both useful in different circumstances, albeit in the perspectives of memory pressure and operation count, the raw-voltage method is best for high-time-resolution science with an array made out of a large number of antennas.

2.3 MeerKAT

2.3.1 Array configuration and backends

MeerKAT is an interferometric array located in Northern Cape, South Africa. It is the most powerful and state-of-the-art radio telescope in the Southern Hemisphere on its own, but also acts as a SKA precursor and will be integrated into SKA1 Mid later (Swart and Dewdney, 2020). In its current configuration, it consists of 64 dishes with a diameter of 13.5 meters with an offset Gregorian design. This structure provides an unblocked optical path that allows multiple receivers to be housed on a rotatable platform in front of the sub-reflector as shown in Figure 2.2.

There are 44 dishes of the array placed in the dense inner core with a diameter of 1 kilometer and the remaining dishes sit sparsely in the outer region. They can form a shortest baseline of 29 meters and the longest baseline of 8 kilometers. The outputs of the receivers are digitized in the “D-engine” on the above-mentioned platform and then transmitted back via optical fiber to the nearby Karoo Array Processor Building (KAPB, The green square in Figure 2.3).

In the KAPB, the digitized signals are first transmitted to the correlator/beamformer (CBF) which consists of F-engines, X-engines and B-engines. The F-engines split the signals into a certain number of frequency channels using a polyphase filter-bank. The product will then be distributed to various

Figure 2.2: A MeerKAT dish. Between the main (big) reflector and the sub-reflector is the rotatable receiver platform. Credit: idia.ac.za

engines and user-supplied equipment (USE). The X-engines create visibilities through the correlation on pairs of antennas for the Science Data Processor (SDP). The B-engine is the MeerKAT's own beamformer that currently forms 1 coherent beam for the pulsar timing (PT) USE. The Breakthrough Listen (BL) USE performs radio technosignature search. The filterbanking beamformer (FBF) USE forms a larger number of coherent beams for the transient search (T) USE and accelerated pulsar search (APS) USE. The inputs and outputs of the signals are illustrated in Figure 2.4.

2.3.2 Large science projects

Some of the ongoing and planned science projects for MeerKAT are: The LADUMA (Looking at the Distant Universe with the MeerKAT Array) project (Holwerda, Blyth and Baker, 2012) aims to detect neutral atomic hydrogen at the wavelength of 21 cm. The high sensitivity of MeerKAT makes it possible to perform ultra-deep surveys and its result can be used to constrain the fueling models in the evolution of galaxies.

The MeerTIME (pulsar timing with MeerKAT) project (Bailes et al., 2020) takes advantage of the high sensitivity of MeerKAT to perform timing of over 1000 pulsars. The result of the project can be used to test theories of gravity and search for the gravitational wave background.

The MIGHTEE (MeerKAT International GHz Tiered Extragalactic Exploration) survey project (Jarvis et al., 2016) performs ultra-deep surveys on four extragalactic fields to provide radio continuum and polarisation information. It tries to study the evolution of AGN, the evolution of neutral hydrogen and the properties of cosmic magnetic fields, providing an early evaluation of the similar projects that will carry out with the upcoming SKA.

The TRAPUM (Transients and pulsars with MeerKAT) project (Stappers and Kramer, 2016) is a

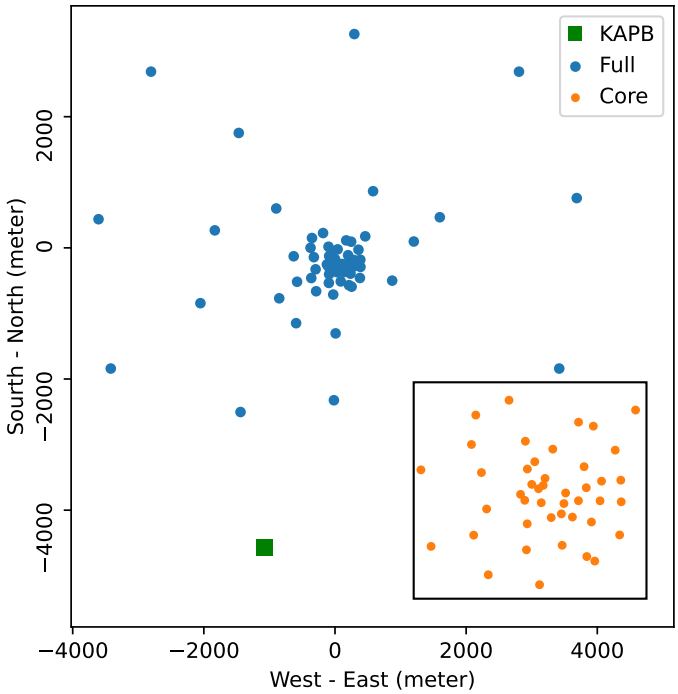

Figure 2.3: The distribution of MeerKAT dishes. The dishes are plotted by their East North Up coordinates which are centered at the reference point of the array (-30:42:39.8, 21:26:38.0). The blue dots indicate the position of all dishes, the orange dots indicate the position of the core dishes in a zoom-in window. The green square indicates the position of the Karoo Array Processor Building.

survey for high time resolution sciences including but not limited to increasing the number of pulsars of all kinds to perform population studies. It surveys multiple globular clusters for millisecond pulsars as they are unique laboratories to test gravitational theories. Another important plan is to search for pulsars in Galactic center for studying the interaction between the supermassive blackhole Sgr A* and its environment. Other plans include timing pulsars to detect gravitational waves and searching for fast transients such as RRATs and FRBs .

2.3.3 Beamforming Approaches

The antenna distribution of MeerKAT is designed to support a wide range of sciences. The inner core of dishes should provide sufficient UV coverage that is very important for high dynamic range imaging to reveal weak features. Large beams can be formed using the core for wide field transient search while keeping the data rate at a modest level. The outer dish components build up long baselines for high spatial resolution imaging or provide localization of a transient detection. To meet these requirements, both the inner core and outer components are distributed according to a Gaussian UV-distribution (shown in Figure 2.3) which is not optimized for visibility beamforming, thus for fast transient science cases, it performs beamforming by applying delays to raw voltages.

In contrast, other interferometric arrays that are highly regular such as a square array with evenly placed antennas create a large number of redundant baselines. This allows the usage of an optimized

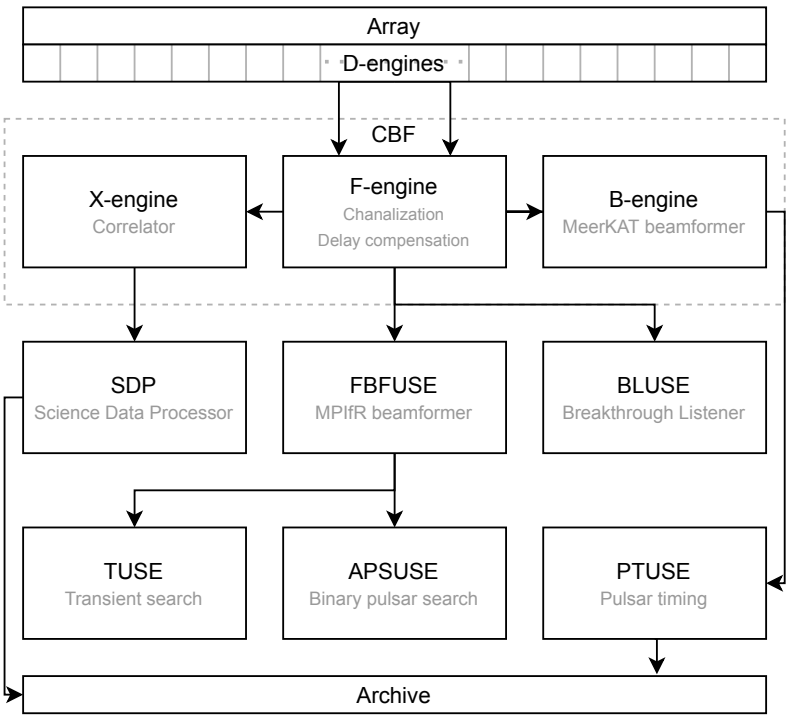

Figure 2.4: The input and output of the signals in MeerKAT

inverse Fourier transform procedure that would dramatically reduce the amount of data needed to be processed so that the image or beams can be formed much rapidly. In this way, one can obtain a great number of beams while retaining high time resolution, which has been demonstrated by CHIME and HIRAX (Newburgh et al., 2016). Obviously, one needs to consider how an even or sparse sampling of the UV plane affects the observation and science applications.

2.3.4 A transient search system

The MeerKAT S-band project

The S-band project (Kramer et al., 2016) is a collection of contributions to MeerKAT from the Max-Planck-Institut für Radioastronomie to greatly enhance the array's capacity in various aspects. It consists of a suite of 64 S-band receivers covering from 1.75 to 3.50 GHz, a total power beamformer (FBFUSE), a computing cluster for binary pulsar searching (APSUSE). Aside from the receivers, other components are available to other observational frequencies such as L, UHF bands.

The science goal for this project is to perform deeper and wider pulsar and transient searches, to observe the molecular diffuse interstellar medium and to carry out very-long-baseline interferometry. The high time and spatial resolution and wide field of view capability of the S-band project have made MeerKAT an excellent tool for pulsar and transient search which is detailed in the TRAPUM project introduced in Section 2.3.2. Furthermore, S-Band is an ideal observational frequency for methylidyne molecular lines, which are a useful probe of diffuse molecular material in translucent clouds. With the high sensitivity of MeerKAT and the S-band receivers, a deep survey on CH in the Southern Galaxy

and extragalactic sources can be achieved. MeerKAT will also be a great addition to the European VLBI network (EVN) thanks to its sensitivity and site location. The L-band and S-band observational frequencies are valuable in resolving the detailed structures in the extended emission of jets of AGN.

FBFUSE

The filterbanking beamformer user-supplied-equipment (FBFUSE) (Barr, 2018) is a total power beamformer developed and built by Max-Planck-Institut für Radioastronomie for MeerKAT. It subscribes the channelized products from the F-engine then invokes Mosaic (introduced in Chapter 3) to generate tilings and calculate the weights polynomials periodically to form directional beams. The beamformed data are transmitted back to the MeerKAT internal network and are subscribed by the TUSE and APSUSE. A more detailed description and illustration of these processes are presented in Chapter 3.

The delay compensation to the channelized data is achieved using the software package PSRDADA_CPP[2]. FBFUSE consists of 32 dedicated GPU servers connected to the MeerKAT internal network with 40-GbE interfaces. Each node contains 2 CPUs with 10 cores, 2 Terabyte SSD storage, 384 Gigabyte RAM and 2 GPUs. PSRDADA_CPP takes advantage of the DP4A hardware instruction in the Nvidia GPUs to perform integer summation instead of the floating pointing operation, resulting in a factor of 4 performance improvement. The default configuration of FBFUSE is capable of generating 1760 beams with 32 antennas and 960 beams with 64 antennas assuming every 16 samples are integrated before the beamforming process.

In this chapter, I described the requirements for large-scale fast transient surveys and suggest that beamformed observations with interferometry are an effective approach to carry out such surveys. In the next chapter, I introduce the general idea of beamforming and its different implementations. To realise this technique in general interferometric arrays, I developed a software package called Mosaic to fulfill the beamforming procedure and tiling generation. The aforementioned features of beamforming are demonstrated with practical applications in the MeerKAT telescope.

[2] https://github.com/ewanbarr/psrdada_cpp

CHAPTER 3

Beamforming with MeerKAT

This chapter is based on a paper submitted to and accepted at the time of writing by Journal of Astronomical Instrumentation with the title "Wide field beamformed observation with MeerKAT".

The full list of authors is: Weiwei Chen, Ewan Barr, Ramesh Karuppusamy, Michael Kramer, Benjamin Stappers

Contents

3.1 Introduction

Radio pulsars are now accepted as spinning neutron stars and have become important tools for testing fundamental physics. For instance, the binary pulsar system J0737-3030A/B serves as an excellent

natural laboratory for testing theories of gravity (Kramer, 2004) and the discovery of massive pulsars has constrained models of the density of nuclear matter (Demorest et al., 2010; Antoniadis et al., 2013b). Recently, the discovery of Fast Radio Bursts (FRBs) has provided new tools for the study of the Universe at cosmic distances (Lorimer et al., 2007) and the measurement of the cosmic baryonic density (Macquart et al., 2020b). While over 500 FRBs have now been discovered (Petroff et al., 2016b; The CHIME/FRB Collaboration et al., 2021b), the nature of the progenitors is unclear. An increase in the number of FRBs and pulsars, or the discovery of new unknown transient phenomena, motivates the continuation of time domain searches in signals of astronomical origins.

Traditionally, large single dish telescopes have been employed in pulsar and transient searches, despite their small fields of view (FoV) being a major drawback in large surveys. Often, multi-beam receivers or phased array feeds (PAFs) augment single-dish telescopes to increase the FoV, thereby increasing the survey speed (Smits et al., 2009). For instance, the 13-beam receiver on the Parkes radio telescope (Staveley-Smith et al., 1996), the 7-beam on the Arecibo Telescope (Cordes et al., 2006) and 19-beam receiver on FAST Han et al., 2021 have increased the FoV by a factor of 10 and a similar increase in survey speed when compared to single-beam receivers. Other than the increase in FoV, precise localisation is key to the unambiguous association of the FRBs to their host galaxy (see e.g. Macquart et al., 2020b). Similarly, good initial localisation of newly discovered pulsars greatly reduces the time required to converge on an accurate timing model, with which tests of fundamental physics can be done. Lastly, multi-beam observations have become highly desirable for the best FRB and pulsar searches, as they allow for robust discrimination against terrestrially generated RFI.

The seemingly non-convergent requirements of large FoV and a relatively high spatial resolution at sensitivities rivaling large single-dishes are best addressed by radio interferometers comprised of many small dishes. Digital technology has also evolved to allow the generation of thousands of synthetic beams on sky with which the instantaneous FoV can be increased. However, the interferometrically synthesised beam is more complex than its single dish counterpart. Beam shape and the subtleties thereof are also crucial to any source localisation that follows, as evident in the initial localisation of the first repeating FRB (Spitler et al., 2014). This problem is exacerbated in the synthesised beam from an interferometer; the beam shape depends on time and the telescope altitude-azimuth positions. When several such beams are used to tile a given region in sky, the resulting FoV changes continually over the course of an astronomical observation. These intricacies have to be fully characterised for any successful fast radio transient survey. To this end, we develop a method to model the synthesised beam shapes and the aforementioned FoV variation.

We apply these techniques to the MeerKAT interferometer (Camilo, 2018) and present results of simulations and actual observations. MeerKAT is a 64-dish interferometer in the Northern Cape of South Africa, with baselines of up to ~ 8 km and a collecting area of $\sim$9161 m^2. This facility serves as a test bed for our beam generation and beam-packing methods. At the time of writing, the MeerKAT telescope provides one synthesized beam as an observatory facility. Through the use of an externally funded and developed total power beamformer (Barr, 2018), the FoV of beamformed observations can be improved by generating up to 1000 beams on the sky with high time and spatial resolution while achieving sensitivity on par with large single dishes.

The remainder of this paper is organised as follows. We begin with some background on digital beamforming in §3.2. The beam shape, tiling technique to increase FoV and the change in FoV are discussed in the context of multi-beam observations in §3.3. Observations using such a beamformer must be carefully planned to account for the time, frequency and array configuration dependence of the synthesised beam and these aspects are discussed in §3.4 as a case study for the MeerKAT telescope.

In §3.4, we also present a demonstration of the beamformer that makes use of these techniques. We conclude by summarising this work in §3.5.

3.2 Digital Beamforming

Beamforming modifies the spatial response of an array of sensors, resulting in an enhanced sensitivity in a particular direction. In the case of observations with a radio interferometer, this is done by the phase coherent summation of the voltages (see e.g. Van Veen and Buckley, 1988) from the individual receptors. The process can be expressed as

$$F(\theta, \phi) = \sum_{n=1}^{N} f(t_{ref} - \tau_n) w(\tau_n). \tag{3.1}$$

The result of the summation, $F(\theta, \phi)$ in Equation 3.1, represents a directional beam at the desired pointing direction $\mathrm{u}(\theta, \phi)$, with a gain equivalent to the aggregate gain of N antennas. t_{ref} is the time at the array reference, and τ_n is the difference between arrival times of wavefronts from $u(\theta, \phi)$ at antenna n and the array reference. Coherence is achieved by referencing the voltages of antenna n, $f(t_{ref} - \tau_n)$, to the array reference, through the application of delay correction $w(\tau_n)$. The delay τ_n is a function of $u(\theta, \phi)$ and the relative position of the antenna $r_n(x, y, z)$ in the array centered at the array reference as written in equation:

$$\tau_n = \frac{u(\theta, \phi) \cdot r_n(x, y, z)}{c} \tag{3.2}$$

where c is the speed of light. The delay τ_n only represents the geometric delay, any other delays in the system (e.g. instrumental delays) are not included.

Beamforming can be implemented in multiple ways. Here we will only discuss digital beamforming and assume that an initial stage in which the "coarse" delay (the integer sample delay) and the "fine" delays (sub-sample delays) to the phase center are corrected for, leaving only the differential delays between the phase center and the directional beams remaining. These differential delays may be corrected for in either the time domain, through the application of a non-symmetric finite impulse response (FIR) filter (see e.g. Frost, 1972), or in the frequency domain following Fourier shift theorem. In the latter approach, the corrections may be applied directly to the voltages from the receptors or to the cross-correlations of those voltages, the so-called "visibilities" see e.g. Roy, Chengalur and Pen, 2018.

When dealing directly with the voltages from the receptors, compensation for a delay τ in the time domain can be made by a phase shift of $e^{-j\omega\tau}$ in the Fourier domain:

$$\int_{-\infty}^{\infty} f(t-\tau) e^{-j\omega t} dt = e^{-j\omega\tau} \int_{-\infty}^{\infty} f(t') e^{-j\omega t'} dt' , \tag{3.3}$$

where $t' = t - \tau$. For broadband signals, it is first necessary to Fourier transform the voltages from each receptor such that the delays can then be compensated in the form of a frequency-dependent phase shift $e^{-j\omega\tau}$, often referred to as a "weight". While the approaches in the time domain and Fourier domain are analogous, delay compensation in the Fourier domain is used in the majority of modern radio interferometers as it allows for the reuse of the F–stage (Fourier transform) or X–stage (correlator)

in an FX correlator. The choice of whether to use visibility-based or voltage-based beamforming is dependent on the science goals of an observation and the computational power available.

As discussed in Roy, Chengalur and Pen (2018), to achieve the same FoV and time resolution with voltage and visibility beamforming, the visibility method has a higher instantaneous memory requirement than the voltage method by a factor of $\frac{N_{ant}-1}{2}$, where N_{ant} is the number of antennas. This is due to the fact that in the case of visibility beamforming one must integrate over all baselines in the array whereas in the case of voltage beamforming one must only integrate over all antennas in the array. The difference in computational cost between the two methods depends strongly on number of samples that are integrated in the correlator. For beamformers designed to produce high time resolution data (e.g. for instruments performing pulsar and fast transient searches) it is thus in general preferable to use voltage beamforming. If the time resolution required from the beamformer is such that $N_{int} > \frac{N_{ant}-1}{2}$ then visibility beamforming is computationally cheaper. It should be noted that this only holds for arrays without redundant baselines. For arrays with redundant baselines, exploitation of the redundancy can reduce the cost of visibility beamforming. This paper focuses on applications that use voltage beamforming and that apply delay corrections via phase shifting in the Fourier domain.

3.3 Multi-beam Observations

As noted in the introduction, multi-beam beamformers can greatly enhance the scientific capabilities of an interferometer through increasing point-source survey speed. However, to be effective in such surveys, care must be taken during observation planning as the survey speed and completeness is dependent on the ever-changing shape of the synthesised beams and the tiling of those beams on the sky. In this section, we discuss the simulation of the synthesised beam shape and the generation of efficient tiling patterns.

We can decompose the problem of efficient multi-beam observations into three components:

- Determination of the synthesised beam shape
- Packing of the beams to generate a tiling
- Time-dependent evolution of the tiling pattern

To solve this problem, we have developed Mosaic[1], a pure Python software package that implements tools to characterize the beam shape and generate efficient tilings.

3.3.1 Beam shape simulation

Provided with an arbitrary set of antenna positions and a source position, the Mosaic package uses a sparse discrete Fourier transform approach to recover the point spread function (PSF, also known as the synthesized beam) of the array with a user-defined spatial resolution and FoV. The PSF is frequency dependent and the decision of which frequency to use for an observation is usually dictated by source and science goals. As such, frequency selection is handled on a case-by-case basis. By default, Mosaic weights each antenna in the array equally during the generation of the PSF. However, in real observations, the performance of the antennas and the quality of the calibration applied may

[1] https://github.com/wchenastro/mosaic

vary. This results in non-uniform amplitude and phase responses across all antennas, causing the true PSF of the observation to differ from the simulation. To allow for more realistic PSF simulations, MOSAIC accepts individual complex weights for each antenna. Manipulation of these weights allows the user to implement various apodization schemes (see e.g. Mort et al., 2016).

Due to the generally poor instantaneous UV coverage of interferometers, the shape of the PSF is often complex. As illustrated in Figure 3.1, the region bounded by a certain response level may be irregular. However, for the purposes of later tessellation of beams in a tiling, it is helpful to approximate it as an ellipse. In this way, the beam shape is represented as a pair of semi-major, a, and semi-minor, b, axis lengths and the orientation of the beam, θ, as shown in Figure 3.1. However, a single set of semi-axes and angle neglects the variation of the beam shape at different response levels. For this reason, MOSAIC produces a series of contours for the synthesized beam at different response levels. For each response level, the beam is approximated by fitting an ellipse to the respective contour, using an algorithm derived from Fitzgibbon, Pilu and Fisher (1999). In the end, this set of approximations is interpolated over to construct a smooth model of the beam shape as a function of response level that can be quickly looked-up during tiling.

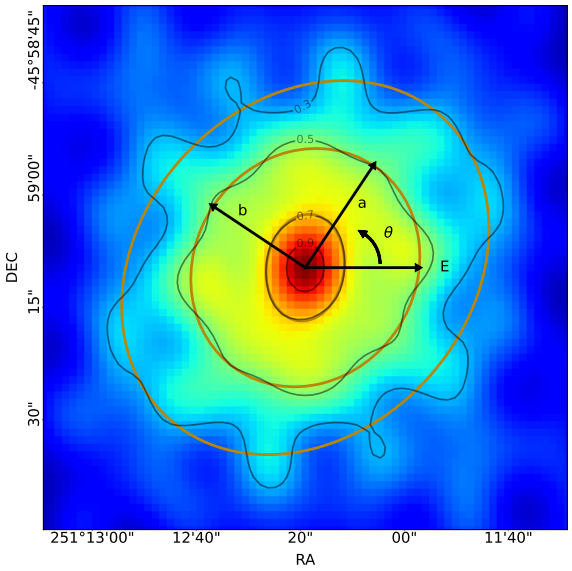

Figure 3.1: Beam shape approximation: The background shows a simulated PSF for a MeerKAT observation using 54 equally weighted antennas. The orange ellipses represent the approximations of the beam at 30%, 50% and 70% response levels as determined by the modelling procedure (see text). The semi-major, a, and semi-minor, b, axes and orientation angle, θ, of the modelled beam at the 50% response level are also indicated. The orientation angle is measured from the east of the image plane. Black closed lines show the corresponding true contours of the PSF at the 30%, 50%, 70% and 90% response levels.

3.3.2 Beam tiling

With the beam shape approximated as a set of ellipses at different response levels, an efficient tessellation can be achieved through hexagonal packing. The sensitivity profile of the tiling is determined by the separation of the beams. Different science goals often require a different uniformity

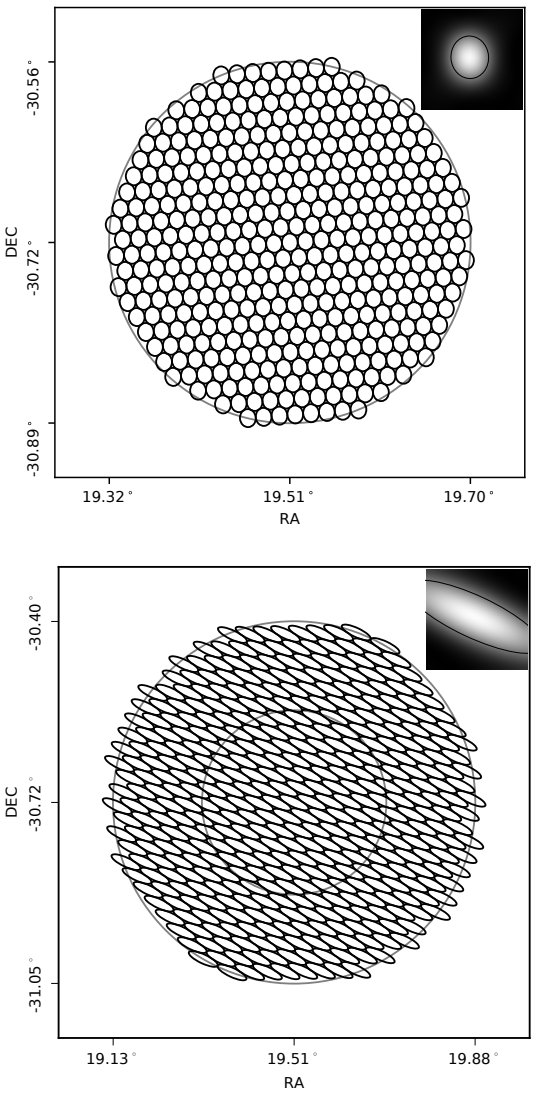

Figure 3.2: Beam shape variety and tiling: The PSF, fitted beam shape and tiling configuration for the inner 44 antennas of the MeerKAT array when pointing at zenith (top, with 405 beams) and near the horizon (bottom, with 409 beams). The inner circle of the bottom panel is the size of the tiling of the top panel. The sky coverage of the tiling on the bottom is noticeably larger than the one on top due to the shallower projection angle of the array when observing at lower elevation.

of sensitivity, as such the separation of the beams may be tuned by setting an "overlap ratio" parameter. This parameter determines the response level at which neighbouring beams intersect in the tiling pattern. For example, an overlap ratio of 50% implies that the beams intersect at their fitted half-power points.

There are two methods to tile the beams depending on whether the user requires a fixed overlap (constant minimum sensitivity) or a fixed boundary of the tiling (constant FoV). In the case of fixed

overlap, the tiling is created as follows:

1. The tiling code retrieves the semi-axes and orientation from the beam shape model, according to the required overlap ratio.
2. The user selects either a circular (as seen in Figure 3.2) or hexagonal bounding box and the tiling code calculates a possible radius or circumradius using the semi-axes and desired number of beams.
3. Twice this radius is used as a side length to create a square tiling of beams. Assuming the horizontal and vertical semi-axes of the beams are a and b (i.e. using an initial tiling frame in which $\theta = 0$), to form a tessellation in the square tiling, beams in the same row are separated by $2a$ and neighbouring rows are vertically offset by $\sqrt{3}b$ and horizontally offset by a.
4. The tiling is rotated by the orientation angle, θ, obtained from step 1 such that tiled beams now have their true orientation in the image plane.
5. Beams are filtered to retain only those which lie inside the bounding area chosen in step 2.
6. If the absolute difference between the required number of beams and the number inside the bounding box is larger than a user-defined tolerance, the code will update the assumed bounding radius calculated in step 2 and re-run the subsequent steps. This is repeated until the desired tolerance is achieved.

If the user requires a fixed bounding box for the tiling, the following steps are used:

1. The user specifies a bounding box in the form of a circle, hexagon, ellipse, arbitrary polygon or annulus.
2. The tiling module calculates a possible overlap ratio according to the scale of the bounding box and the desired number of beams. For the case of circles and hexagons, the area of the bounding box is used as a prior in this calculation, while for other shapes, the distance between the furthest point of the boundary and the tiling center is used as the prior.
3. The code retrieves the corresponding semi-axes and orientation angle from the beam model according to the overlap obtained from the step 2.
4. It creates a square tiling and rotates it like in the steps 3 and 4 of the fixed overlap method, the only difference is that the side length is two times the distance between the furthest boundary point and the center of the tiling.
5. The code filters the beams by which lie inside the specified boundary. For a polygonal boundary, the determination of whether a beam lies inside the boundary is done using an implementation[2] of Shimrat (1962). For an annulus boundary, the beams inside the outer boundary and inner boundary are determined separately, with only beams which lie inside the outer boundary but not the inner boundary being retained. The annulus boundary is especially useful when combined with another tiling having the same size of the inner boundary of the annulus but with different overlap ratios as this allows for variable overlap ratios in a single pointing.

[2] https://wrf.ecse.rpi.edu/Research/Short_Notes/pnpoly.html

6. For this method, it is unlikely that the difference between the number of beams required and the number of beams inside the boundary is within the defined threshold in the first tiling attempt. The module tries to increase or decrease the overlap ratio to reduce the difference by performing an optimization routine with the overlap ratio as the free parameter. However, as discussed in section 3.3.1, the semi-axes and orientation can change with different overlap ratios. Therefore, it is necessary to obtain a new set of semi-axes and orientation angle whenever the overlap ratio is changed. This is also the reason for interpolating a smooth model in the last step of beam shape simulation so that the tiling module can obtain the beam shape in a specific overlap ratio quickly during the optimization routine without re-evaluating the PSF in every tiling attempt.

Two examples of generated PSFs for MeerKAT (discussed further in Section 3.4) and the corresponding circular tiling pattern are shown in Figure 3.2. There are two important caveats to note here. First, we assume the desired tiling covers a sufficiently small solid angle, such that the shape of all beams in the tiling can be reasonably approximated by the beam shape at the centre of the tiling. In the case of large tiling areas where non-isoplanactic effects become important, it is recommended that the tiling area be split into multiple sub-tilings such that each sub-tiling has a locally correct beam shape. Secondly, we assume that the synthesised beam may always be reasonably approximated by an ellipse at some response level. This assumption does not necessarily hold for all array configurations and response levels. Furthermore, the auto-optimized overlap ratio in a fixed boundary tiling is hard to predict due to the variable orientation angle of the beam at different response levels. As such, when a specific minimum sensitivity is required across the tiling pattern, it is encouraged to perform *a priori* simulations of the tiling locally using Mosaic to ensure the result is acceptable.

3.3.3 Tiling evolution

In the beam tiling process described above, the generated tiling is valid for a single array configuration, frequency and epoch. When tracking positions that are not in a fixed frame with respect to the array, there are two important effects that alter the tiling. The first is the array projection, whereby the instantaneous UV coverage of the array changes with the position of the source, thus changing the PSF and therefore also the approximated beam shape. The second is parallactic angle rotation whereby beams with fixed celestial coordinates will orbit the array boresight due to the rotation of the Earth. These effects are shown in Figure 3.3. This changing of both beam shape and position results in tilings becoming inefficient over time as the beams become more or less overlapped and the sampling of the desired tiling region becomes less uniform. The magnitude of this effect can be simulated. However, the metric by which one evaluates the efficiency of the tiling is necessarily dependent on the goal of the observation. For example, a targeted point source observation with a relatively small extent may oversample the search region to allow for longer observations that are not as sensitive to the changing beam shape and orientation. Alternatively, a blind point source survey may optimise for survey speed by defining a maximum observation duration during which the tiling can remain above some efficiency threshold. For the purpose of demonstrating the effects of tiling evolution, in this article, we define tiling efficiency as the fraction of the tiling area which is neither oversampled nor undersampled. This idea is illustrated in the images on the right of Figure 3.3. Here we treat all beams as their approximated ellipses and sample the tiling pattern to find regions covered by only one beam (shown in green), more than one beam (a proxy for excess overlap ratio or oversampling, shown in red), no beams (a proxy for undersampling, shown in blue).

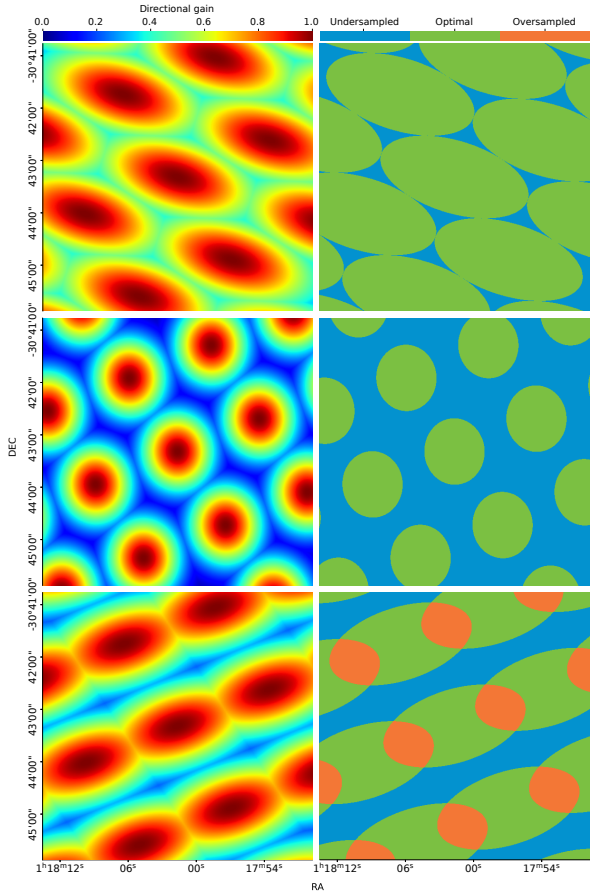

Figure 3.3: Overlap evolution through time: The images on the left are the simulated direction gain of the array throughout the tiling. The images on the right are the profile of the beams with their widths plotted at their 50% power level. The top row shows the situation at the start of the observation with an optimized tiling and an hour angle of 285°. The middle row shows the situation 6 hours later with an hour angle of 15°, large gaps exist between the beams. The bottom row shows the situation 10 hours after the start of the observation with an hour angle of 60° when the beams are overlapped with each other at a high ratio while large gaps exist at the same time. These simulations all have the same field of view.

In practice, it is incumbent on the observer to simulate the evolution of the tiling efficiency over the course of an observation to make decisions on if and when re-tilings should occur. Re-tilings result in all beams changing their tracking positions and thus may be problematic for observation types that require unbroken integrations on specific positions, such as coherent pulsar searches. The rate of change of the tiling efficiency and its impact on observations is explored in greater depth in Section 3.4.3. The techniques described above are implemented in Mosaic for arbitrary arrays. Below we look specifically at beamforming with the MeerKAT array and discuss Mosaic's deployment as part of the multi-beam beamformer.

3.4 Multi-beam observations with MeerKAT

3.4.1 The FBFUSE beamformer

To support time domain pulsar and fast transient discovery at MeerKAT, the Max–Planck–Institute for Radio Astronomy has developed a multi-beam beamformer capable of forming of the order of 1000 total power beams using the full MeerKAT array. This beamformer, known as FBFUSE (Filterbanking Beamformer User Supplied Equipment, Barr, 2018), provides the data products required by the TRAPUM experiment (Stappers, 2016) to perform target searches for new pulsars, by the MeerTRAP project (Sanidas et al., 2018) to perform real-time commensal searches for fast radio transients and by the MeerKAT Galactic Plane Survey (MGPS) to perform a wide-field survey for pulsars in the Galactic plane at L-band and S-band Kramer et al., 2016. The technical details of the FBFUSE instrument will be addressed elsewhere. Here we will focus only on how the Mosaic software is used as part of FBFUSE and the implications of the effects described in Section 3.3 on observations.

The delay compensation chain for observations with FBFUSE is shown in Figure 3.4. Voltages sampled at individual antennas are first propagated to the MeerKAT F-engines where channelisation is performed. The F-engines compensate for the geometric delay to the source under observation through first a coarse delay correction prior to channelisation and then a fine phase correction post channelisation. The channelised voltages from the F-engines are then transmitted via an Ethernet network to the FBFUSE instrument, where complex gain correction provided by the MeerKAT Science Processor sub-system is applied to correct for the instrumental delays among the streams from all antennas at all frequencies (depending on the telescope and observation configuration, this correction can also be applied inside the F-engines). At this stage, a direct summation of the voltages from each antenna would result in a coherent beam at the telescope phase centre. To produce tilings of off-boresight beams, FBFUSE invokes Mosaic to generate both an efficient tiling of beams on the sky and the corresponding delay polynomials required to re-phase the channelised voltage data to each beam position. FBFUSE uses calibration solutions provided by MeerKAT's Science Data processing (SDP) system (Jonas and MeerKAT Team, 2016).

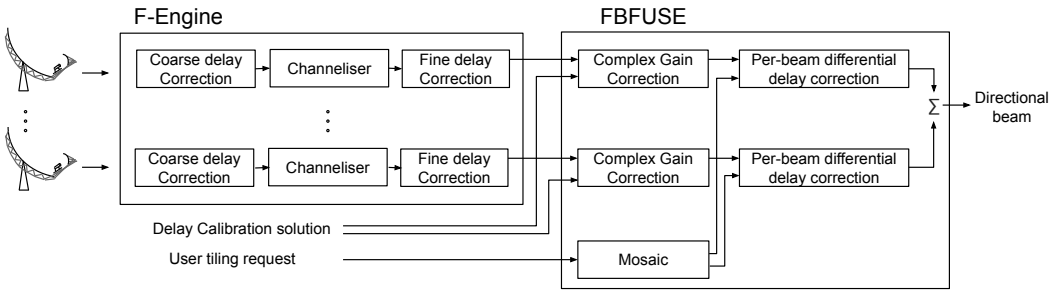

Figure 3.4: Delay compensation chain for FBFUSE observations: The voltages from individual antennas first go through the F-engine where they are coarse delay corrected, channelized using a polyphase filterbank and fine delay corrected. After the F-engine, the voltages are all phased with reference to the telescope phase centre (usually the boresight pointing position). In FBFUSE a per-beam differential delay compensation calculated by Mosaic is applied to the voltage to form coherent beams at sky positions defined by the tilings being used.

The tiling and delay pipeline used in Mosaic is shown in Figure 3.5 and is described below:

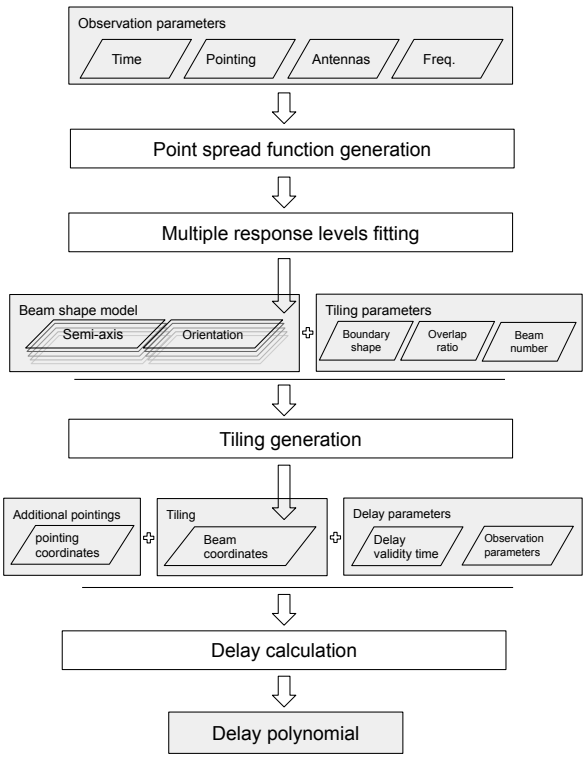

Figure 3.5: Beamforming procedure. Process units are in white boxes and the grey boxes are inputs or outputs to or from the process units. The beam shape model is a table of semi-axis and angles indexed by response level.

- **Beam shape simulation:** FBFUSE retrieves the observer requests and provides Mosaic with the desired epoch of observation, the current MeerKAT array configuration and the observing frequency. Using these, Mosaic simulates the PSF at the array phase centre accordingly. A beam model is constructed by fitting ellipses to the contours of the PSF at different response levels.

- **Tiling generation:** FBFUSE retrieves one or more predefined tiling configurations requested by the observer which include the number of beams in each tiling, the shape of the tiling boundary, their overlap ratio or the boundary size and the central position of the tiling. As noted above, for an optimal gain response the beams should be tiled around the array boresight where the directional gain of the antennas is maximised. However, for more flexibility, Mosaic supports the generation of an arbitrary number of off-boresight tilings to support observations in which there are multiple extended sources of interest within the telescope FoV. With the requested tiling configurations, Mosaic derives the corresponding semi-axes and the orientation angle from the beam model and generates a set of beam positions in equatorial coordinates. At this stage, the observer may also specify independently tracking beams not in a tiling to cover known point sources within the FoV.

- **Delay polynomial generation:** For each of the beam coordinates b_i generated in the preceding step, the geometric delay terms $d_{b_i}(t)$, are calculated. Additionally, the geometric delay to the array phase centre, $d_{\circ}(t)$, is calculated. As the data received by FBFUSE have already

undergone delay correction to the array phase centre, it is the differential delay between each beam position and array phase centre, $\delta d_{b_i}(t) = d_{b_i}(t) - d_\circ(t)$, that is required by FBFUSE to produce coherent beams. The delay values, $\delta d_{b_i}(t)$, are calculated for each beam and a first order polynomial is fit to the values. FBFUSE periodically invokes Mosaic to calculate new polynomials which are evaluated inside the beamformer to produce and update weights. The minimal weight update interval (MWUI) is defined as the length of the time before the position error of the beam caused by the rotation of the earth, becomes as large as 1% of the diameter of the beam (corresponding to a 0.028% loss of sensitivity for a Gaussian beam). The length of MWUI is shorter if the distance between the beam and the boresight is larger and the size of the beam is smaller. Therefore, MWUI is calculated considering the beam is formed at the edge of the primary beam with the longest baseline (7697.58 meters). The value of MWUI is 481 ms for the abovementioned situation, while in a practical MeerKAT observation, 100 ms is used to compensate for the change of the beam shape during the interval. In the meantime, the delay polynomial is produced in every 2 seconds.

3.4.2 Point source survey speed

The point-source survey speed achievable with beamformed observations with MeerKAT is dependent on the array configuration, sensitivity of the individual antennas, beamforming efficiency and the total number of beams that can be produced. We estimate the survey speed figure of merit (FoMSS) using a modified version of equation (3) of Cordes (2009):

$$FoMSS = B\frac{\Omega_{\text{beam}}}{N_{sa}}\left(\frac{f_c A_e}{mT_{\text{sys}}}\right)^2 \sum_{i=1}^{N_{beam}} g_i^2, \tag{3.4}$$

where B is the bandwidth of the receiver, N_{beam} is the number of synthesized beams, Ω_{beam} is the field of view of a single synthesized beam, N_{sa} is the number of sub arrays, A_e is the effective collecting area of the array, f_c is the fraction of A_e that is available, m is the threshold of signal-to-noise ratio (S/N) for detection, T_{sys} is the system temperature and g_i is the fraction of the peak of the primary beam gain at the position of synthesised beam i. The model of the primary beam was obtained using the katbeam[3] package which uses a cosine-tapered field model as suggested by Mauch et al. (2020). The gain within a coherent beam was considered constant in this calculation. Currently, the FBFUSE beamformer may only be used in a single MeerKAT subarray making $N_{sa} = 1$.

Figure 3.6 shows the FoMSS for multi-beam observations with MeerKAT under different array configurations, numbers of beams and source elevations. Here we consider a simple array definition based on the incremental inclusion of dishes in order of increasing distance from the array centre. Initially, the FoMSS values increase because of the addition of the core dishes and the integrated FoV of the beams exceeding the FoV of the primary beam (here defined as the FWHM of the primary beam at an arbitrary frequency). However, as more dishes further away from the core are included, the beams become smaller and eventually reach a turning point where they can no longer fill the primary FoV. The array size that maximises the FoMSS for different numbers of beams and source elevations is provided in Table 3.1. For a typical observation using approximately 1000 beams, we find that the optimal number of antennas to use for survey observations is between 37 and 41 depending on the

[3] https://github.com/ska-sa/katbeam

average elevation of observations.

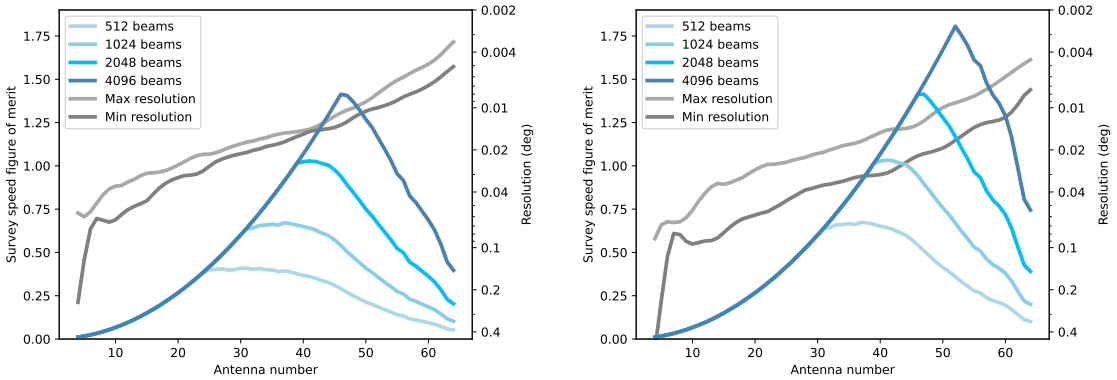

Figure 3.6: Survey speed figure of merit (FoMSS) as a function of array size when the source is at zenith (left) and at an elevation of 30° (right). Antennas are included in the array in order of increasing the distance from the array centre. The FoMSS is shown for four different maximum beam numbers (we note that although the current FBFUSE beamformer can only produce ∼ 1000 beams for the full array, it can produce more for smaller arrays due to the lower computational cost of beamforming with fewer antennas). The maximum and minimum angular resolution of the simulated beam for each array size is shown in gray.

Table 3.1: The array size (in number of antennas included radially from the array centre) required to maximise the survey speed figure of merit (FoMSS) for different numbers of synthesised beams.

	Elevation			
N_{beams}	90°	60°	45°	30°
512	33	33	33	37
1024	37	37	38	41
2048	41	42	44	47
4096	46	48	49	52

3.4.3 Tiling validity

For long duration observations, it may be necessary to re-tile the beams as the current tiling becomes less efficient due to the changes in the beam shape as illustrated in Figure 3.3. It is therefore useful to determine how long before a tiling generated at the start of that observation drops below some pre-defined efficiency. Here we simulated the beam shape evolution with time for the full MeerKAT array to determine the validity time of a tiling at a given declination.

Simulated observations start at timestamp t_0 with an optimized tiling. The beam shape is then updated with an interval δt (1 minute). At each update, a new beam shape is generated for that epoch and the resultant beams are positioned at the tiling coordinates from t_0. The tiling efficiency

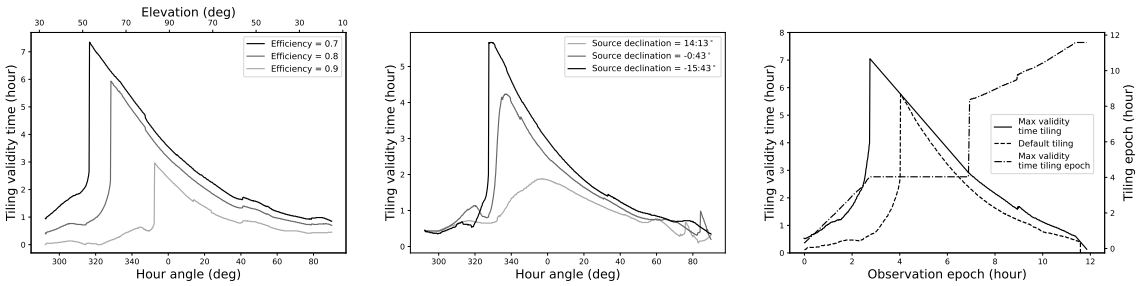

Figure 3.7: Left: The tiling validity time as a function of starting hour angle at various efficiency thresholds for a source that transits through the zenith at MeerKAT. Middle: The tiling validity time for an efficiency 0.8 tiling as a function of starting hour angle for sources at a range of declinations. Right: The maximum validity time as a function of observation epoch for a source transiting through the zenith with an efficiency 0.8 tiling. The solid line is the max validity time that can be achieved when the observation starts with a non-optimal tiling, while the dashed line is the result when starting with an optimal tiling. The dashed-pointed line is the epochs of the non-optimal tiling for difference observation epoch to achieve max validity time (see the last paragraph of section 3.4.3 for an example).

(defined in Section 3.3.3) is then measured. If it exceeds the desired efficiency, the simulation will continue. If the target efficiency is not met anymore, the simulation is stopped and the time since t_0 is recorded as the tiling validity time. The process then repeats with a new simulation starting at time $t_1 = t_0 + \delta t$. This process is continued until the source drops below 10° in elevation. The simulated validity time with different efficiency thresholds is plotted in the left panel of Figure 3.7. This shows the validity time of the tiling as a function of the hour angle for a source that transits through the zenith at MeerKAT. The simulation shows that the validity time has a sharp peak before the source reaches the zenith, then gradually decreases for the rest of the simulation, with the peak of the validity time occurring earlier for lower efficiency thresholds.

The middle panel of Figure 3.7 shows the tiling validity for a range of source declinations. Here we see that declinations that result in lower-elevation source transits have shorter validity times. This can be understood by considering that at lower elevations the beams have a higher degree of asymmetry and as such the rotation of these beams will have a larger effect on the tiling efficiency.

If we start an observation in which the tiling is initially non-optimal but transitions into an optimal configuration with time, the "max validity time" should be longer than the scenario in which the observation starts with an optimal tiling. This can be seen by simulating the max validity time using the same source of the left panel of Figure 3.7 with a tiling efficiency of 0.8. The virtual observation started at 6 am with a duration of 12 hours. The duration was divided into 720 timestamps. The simulation started at timestamp t_0 and calculated a corresponding beam shape, based on which a tiling c_{t_0} was also generated. Then the simulation moved to t_{-1} which was the closest timestamp before t_0 (if existing). The beam shape of timestamp t_{-1} was calculated and it was put into tiling c_{t_0} for the evaluation of the tiling efficiency. If the tiling efficiency was above the threshold, the simulation would continue to move to timestamp t_{-n} where $n = 2, 3, 4, ...$, otherwise, the simulation would move to timestamp t_{+1}. Similarly, a new beam shape was generated and put into the tiling c_{t_0} for efficiency evaluation. If the threshold is not reached, the simulation would move to t_{+n}, otherwise, the optimal validity time for timestamp t_0 is $t_{+n-1} - t_{-n+1}$. In this manner, the simulation iterated all timestamps and the result is plotted in the right panel of Figure 3.7. The solid line in the plot is the max validity time starts with a non-optimal tiling against the timestamps, while the dashed line is the validity time

starts with an optimal tiling. As can be seen from the comparison, the former approach produces a longer validity time than the latter and moves the sharp jump earlier. Additionally, the dash-dotted line indicates the best tiling for a given timestamp. For example, the best tiling to achieve a long validity time for timestamp 8-hour is the tiling generated from the beam shape near timestamp 9-hour. The straight line from 2.7-hour to 6.9-hour indicates that the tiling generated at the beam shape of the 4-hour timestamp produces the overall best validity time for that period.

3.4.4 A beamformed observation of 47 Tucanae

We carried out two observations using the MeerKAT MPIfR multi-beam system to test and verify the beamforming and tiling system.

MeerKAT observations

At 06:00 UTC on May 2, 2020, a 4-hour observation of the globular cluster 47 Tucanae (NGC 104) was made. A total of 56 antennas were used with the majority being in the MeerKAT core. The observing band was centered at 1.284 GHz with a bandwidth of 865 MHz which was divided into 256 channels. During the observation, the source went from an hour angle of -33.4° to 26.8°. Mosaic was invoked to produce a tiling of 264 beams with an overlap ratio of 0.7. The tiling covered a region of approx. 0.45° in R.A. and 0.14° in declination. Additionally there were 24 tracking beams constantly pointing at 24 of the known pulsars in the cluster. The packing of the tiling on the cluster is plotted in the central panel of Figure 3.8 overlying an optical image of 47 Tucanae. Another 440-s observation on the pulsar PSR J1644-4559 was carried out at 11:00 UTC on Dec 1, 2020 with 54 antennas and an overlap ratio of 0.996 to verify the beam shape.

Beamforming Efficiency

The first test was to check the efficiency of the beamforming process as it is the foundation of other applications. If the weight calculation during the beamforming process is incorrect or not accurate enough, the signal from the known pulsars might not be detectable because the antenna data are combined out of phase. To assess this situation, we folded the data of the tracking beams using the corresponding ephemerides of each pulsar. The average profiles for six of these pulsars are plotted in the left and right panels of Figure 3.8 with their positions labeled in the central panel. The average profiles shown are a close match to those obtained by Freire (2000) and Ridolfi (2017).

To determine the efficiency of the beamforming process, we compared the signal-to-noise ratio (S/N) between the incoherent beam and the coherent beams. For the phased addition of N voltages with uncorrelated noise, the signal power increases as N^2 while the noise power increases as N. As such, the S/N of the observed pulsars in the coherent beam should scale as N. For the incoherent beam, the power in each antenna is first detected and then summed. Here the r.m.s. of the noise increases as $\sqrt{N}$ and as such the S/N of the observed pulsars in the incoherent beam should scale as $\sqrt{N}$. The ratio of S/Ns between the coherent to incoherent beam should thus be $N/\sqrt{N} = \sqrt{N}$. Note that the primary beam gain scaling is the same for both the incoherent and coherent beams for a given position in the primary beam and as such the position of the pulsars in the FoV has no impact on the coherent to incoherent S/N ratio. For an ideal beamformer, the expected gain from the incoherent beam to the coherent beam for this observation with 56 antennas should be $\sqrt{56} = 7.48$.

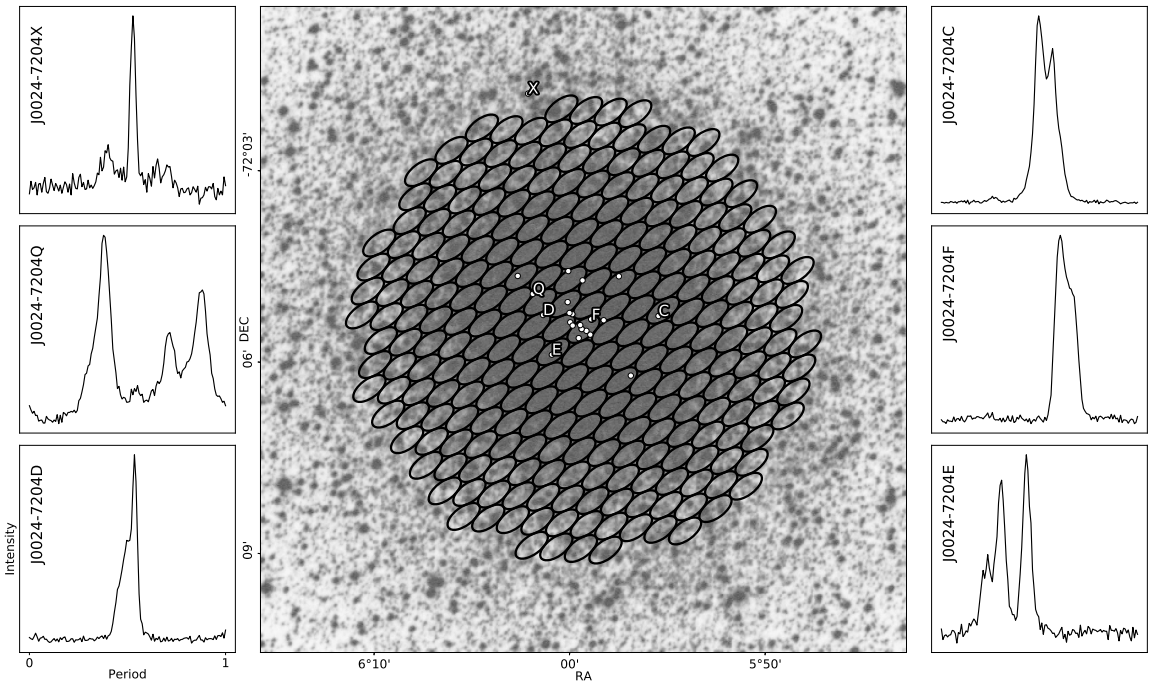

Figure 3.8: Profiles of selected pulsars and the tiling pattern used for observation of 47 Tucanae. In the central panel, the background is an optical image of 47 Tucanae obtained from the STScI Digitized Sky Survey (Lasker, 1994), the ellipses are the tiling of the coherent beams at the start of the observation and the white dots indicate the positions of the known pulsars in the cluster. The average profiles in the left and right panels are folded from the tracking beams on the pulsars whose locations are indicated by their letter designation in the central panel.

We folded the incoherent beams and the coherent beams of the pulsar J0024−7204C, J0024−7204D and J0024−7204E using DSPSR[4] and compared their S/N listed in Table 3.2. The S/N were measured using the `pdmp` tool in the PSRCHIVE[5] software package. It estimates and subtracts the baseline of the data, then uses a matched filter to determine the width of the pulse and calculate the S/N. To account for imperfect folding ephemerides, `pdmp` optimizes over both period and dispersion measure (the integrated free electrons column density between the observer and the source). The efficiency of the beamforming process is then calculated as:

$$\text{Efficiency} = \frac{1}{\sqrt{N}} \frac{\text{S}/N_{\text{coherent}}}{\text{S}/N_{\text{incoherent}}} \tag{3.5}$$

The incoherent beam is more susceptible to contamination by RFI and variations in the system noise of individual antennas. For a coherent beam, these effects are partially mitigated as they sum out of phase during the coherent beamforming (so-called "phase-washing"). This effect can lead to the efficiency of the beamforming being overestimated. The high efficiencies seen here demonstrate that the calculation of the weights is accurate enough to achieve high coherency.

[4] http://dspsr.sourceforge.net
[5] http://psrchive.sourceforge.net

Table 3.2: The S/N of pulsars C, D and F in the coherent and incoherent beams and the derived beamforming efficiency. The efficiency is calculated using Equation 3.5. We note that the incoherent beam is more affected by RFI than the coherent beams which can lead to boosted beamforming efficiencies when using this method.

	J0024−7204C	J0024−7204D	J0024−7204F
$S/N_{\text{incoherent}}$	82	25	35
S/N_{coherent}	642	177	270
Efficiency	105%	94%	103%

Verification of the simulated beam shape

The second test was the verification of the simulated beam shape by comparing it to the power distribution of the sky derived from the observation data of PSR J1644−4559. First, we simulated the beam shape of the array pointed to the source at the planned observation time. Then we observed the source with a very high overlap ratio tiling to densely sample the PSF as illustrated in the left panel of Figure 3.9. The beamformed data were folded and analysed to obtain the S/N measurements of the pulsar in each beam. The observed beams are represented by ellipses with colors normalized by their S/N and plotted in the right panel of Figure 3.9 according to their sky position. The comparison shows the power distribution of the sky is in high agreement with the simulated PSF including the complex structure at the outer region of the beam shape. This also further confirms the correctness of the weighting calculations and the tiling generation. We note that there is a small position offset of ~0.8 arcsecond in the beamformed data probably due to a minor phasing error.

Tracking the change of the beam shape and the tiling

The third test performed was the verification of the change of the beam shape and the tiling by tracking variations in S/N of 47 Tucanae pulsars in multiple beams. There was no re-tiling during the four-hour observation, so the efficiency of the tiling was expected to vary due to the changes of the beam shape as a function of time as discussed in Section 3.3.3 and illustrated in Figure 3.3. As a result, the relative distances between a pulsar and the surrounding beams also change which manifests in their S/N. By simulating the evolution of the tiling, we can predict the trend of the change of the S/N of those beams and verify them with the data.

To perform this test, the observation was divided into four, one-hour segments and the surrounding beams of each pulsar were folded using the known ephemeris. To mitigate temporal variations due to interstellar scintillation, the S/N observed in the surrounding beams was normalised by the S/N in the corresponding tracking beam pointing directly to the respective pulsar. To reduce the effect of the changing PSF over the wide observing bandwidth, only the band between 1.4–1.5 GHz was used. The positions of the pulsar in the PSF of each of the surrounding beams were used to predict their respective S/Ns. The results for the beams surrounding PSR J0024−7204F (beams 25, 26, 36 and 48) are plotted in Figure 3.10. To account for the changing parallactic angle, the average PSF over each one-hour segment was used. In all cases the PSFs were generated at a reference frequency of 1.45 GHz.

The result from the observation is in overall agreement with the expected tiling evolution. Though

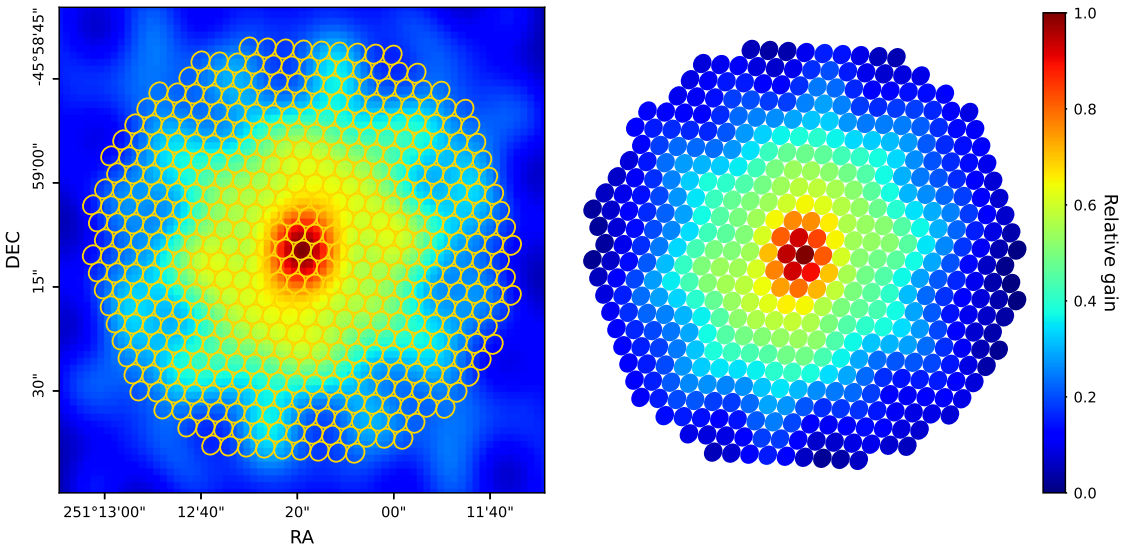

Figure 3.9: Verification of the beam shape: The image on the left is the simulated PSF covered by a tiling. An overlap ratio of 0.996 was used for the purpose of supersampling the PSF. The image on the right is the power distribution of the sky based on a real observation beamformed using the same tiling, array configuration and boresight pointing. The ellipses represent the beams and the color is normalized according to their S/N with the colour bar representing the relative gain of the beam.

the trend of the S/N mostly follows the expected evolution, there is apparently an offset in amplitude between the two. This is likely due to the fact that we do not account for uncertainties in our S/N estimation, scintillation of the source due to propagation through the interstellar medium, and imperfect antenna weighting which leads to differences between the modelled and actual synthesised beam of the array. Despite the offsets in amplitude, the overall agreement between the expectation and the observation indicates that the tiling is correctly generated and implemented in the sky. It also suggests that the simulated PSF can largely represent the telescope gain on the sky and provides a verification of the evolutionary behaviour of the tiling shown in Figure 3.3.

Localization of a point source using multiple beams

With the tiling verified, the position of a pulsar can be estimated using the S/N of its detections in multiple beams. As a demonstration of this capability, we have estimated the position of a pulsar in 47 Tucanae using a Markov Chain Monte Carlo method and compared them with the known pulsar position. To fit the position, we first assume that the pulsar is at an arbitrary position x inside multiple beams N_i, where i is the index of the beam. If the S/N of a beam centered on the pulsar is R_P, then in an ideal situation, the S/N of the beam N_i would be $R_{N_i} = R_P \times P_{N_i}(x)$ where $P_{N_i}(x)$ is the sensitivity of the beam N_i at position x. The values of R_{N_i} can be measured on the observational data and the function $P_{N_i}(x)$ can be constructed with a model of the sensitivity of the beam, e.g. the PSF. With those, the fitting algorithm generates samples of x and evaluates them for multiple beams. A similar method has been proposed by Obrocka, M., Stappers, B. and Wilkinson, P. (2015) which uses multiple tied-array beams and spectral information to estimate the position of a transient source. We fitted the positions of PSR J0024−7204F with this method. The localization results and their

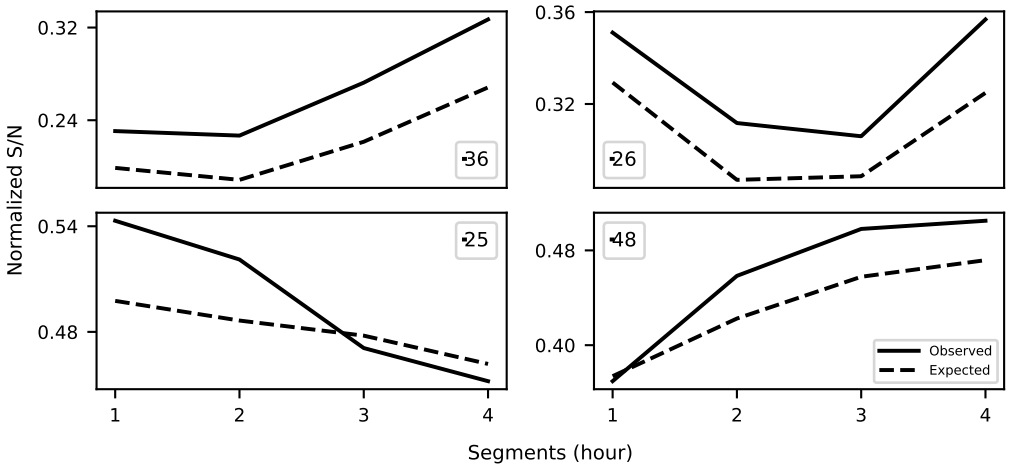

Figure 3.10: The change of the observed S/N (solid line) and expected value (dashed line) for the beams surrounding the position of PSR J0024−7204F, i.e. beams 25, 26, 36 and 48. The corresponding beams are noted in each panel.

95% credible intervals are listed in Table 3.3. The known position of the pulsar is 00:24:03.8554(1), -72:04:42.8183(1), which is taken from the ATNF pulsar catalog[6] (`psrcat`, Manchester et al., 2005)

Table 3.3: The localizations of PSR J0024−7204F in each of the corresponding four, hour-long segments with their 95% credible intervals.

Segment	RA	DEC
1	$00{:}24{:}03.8^{+1.7}_{-1.7}$	$-72{:}04{:}44.6^{+8.6}_{-7.6}$
2	$00{:}24{:}03.7^{+1.8}_{-1.8}$	$-72{:}04{:}43.1^{+10.0}_{-8.9}$
3	$00{:}24{:}03.7^{+1.8}_{-1.8}$	$-72{:}04{:}42.6^{+11.3}_{-9.0}$
4	$00{:}24{:}03.8^{+1.7}_{-1.7}$	$-72{:}04{:}43.9^{+9.9}_{-7.5}$

The localization of the pulsar with multiple beams is largely good. Again, here the observed offsets are most likely due to the aforementioned limitations in our ability to accurately model the PSF. To mitigate the effects of interstellar scintillation, we limit the bandwidth used for localization to 100 MHz. A reduced bandwidth leads to a decrease in S/N which affects the quality of the localization. Nevertheless, these results show that the localization of any detection can be improved (within the size of the beam). In general, better S/N produces better localization. It is also beneficial if the true position of the source lies inside the region where the absolute derivative of the PSF is large, as the predicted S/N changes rapidly there, leading to smaller uncertainties in the estimated localization. A more complete approach would be to use a time and frequency dependent PSF modelling that accounts for the source spectrum and scintillation. This will be addressed in the forthcoming Bezuidenhout et al. in prep.

[6] https://www.atnf.csiro.au/research/pulsar/psrcat/

3.5 Summary and Outlook

In the first part of the paper, we described a general beamforming approach applicable to modern interferometers with a large number of receiving elements. This enables wide field, high time and spatial resolution observations with the sensitivity of all elements coherently combined. To explore how multi-beam observations using this approach can be conducted, a software package called Mosaic has been developed. The package provides tools to simulate and model the beam shape, generate optimized tiling patterns, and predict the evolution of the tiling through time with the choice of performing a re-tile automatically when specific criteria are met.

In the second part of the paper, we discussed practical applications for the aforementioned techniques by applying them to the MeerKAT telescope. It described how beamforming is implemented on MeerKAT and its use during observations. To demonstrate the planning of a multi-beam observation, the validity times of the tilings in different array configurations and source positions are provided.

Finally, we provide the result of real observations using the MPIfR-developed FBFUSE beamformer. These demonstrate the capability of the system to observe multiple pulsars simultaneously with the expected sensitivity and show a high level of agreement between the simulated beam shape and the reconstructed beam shape obtained from a high overlap ratio observation. The consistency between the predicted and observed S/N in each beam around the pulsar location, allowing for arcsecond position determination, demonstrates that the complete system from beamforming to PSF determination and tiling operates as expected for MeerKAT.

The MeerKAT telescope has been using Mosaic and FBFUSE to carry out multi-beam science observations since 2019. Three principal science programs rely on the systems presented in this paper. The Transients and pulsars with MeerKAT (TRAPUM) survey is a pulsar search targeting globular clusters, unassociated FERMI LAT sources, nearby galaxies and miscellaneous high-energy sources. The TRAPUM project seeks to discover millisecond and binary pulsar systems that can be used to answer questions about fundamental physics, the pulsar emission mechanism and stellar evolution. The survey uses various configurations depending on the exact sources and science goals of each different target class. Typically TRAPUM observations use between 277 and 480 beams depending on the observing frequency used. For observations requiring the widest FoV, the MeerKAT core is used, while for observations of targets with small extents (e.g. globular clusters) the full array is used. Currently, TRAPUM operates at L-band (856 – 1712 MHz) and U-band (544 – 1088 MHz) with plans to include S-band observations when the receivers become available (Kramer et al., 2016).

Complementing the TRAPUM project is the 3000-hour MPIfR Galactic Plane Survey (MGPS). This project consists of three parts: a shallow L-band Galactic plane survey, a deep, but limited latitude range, an S-band Galactic plane survey and an ultra-deep 200-hour survey of the region around Sgr A*. The MGPS survey seeks to greatly increase the number of known pulsars in the Galactic field with an emphasis on the discovery of relativistic binaries. Additionally, the Galactic centre portion of the search has the strongest chance to detect a pulsar in orbit around Sgr A*. The MGPS survey uses the MeerKAT core with 480 beams (Padmanabh et al. in prep.) Discoveries from the TRAPUM and MPGS project are made public via the project webpage[7].

More TRAnsients and Pulsars (MeerTRAP) is a project to search for fast transients commensally with other MeerKAT science programs. It performs real-time, GPU-based, time-domain searches for short duration transients such as FRBs and rotating radio transients (RRaTs). It is planned that

[7] http://trapum.org/discoveries.html

upon the detection of a new interesting source, the MeerTRAP project will provide a trigger to the transient buffer implemented in the beamformer. This allows for robust localisation and polarisation analysis for discovered transients. A demonstration of the system has been made through observations of FRB 121102 (Caleb et al., 2020). Due to its nature as a commensal project, MeerTRAP has a diverse array of configurations. Typically it uses the MeerKAT core with 480 or 864 beams depending on the configuration on the MeerKAT F-engines.

The upcoming SKA-mid (Swart and Dewdney, 2020) will be a similar array to MeerKAT with an increased number of antennas and longer baselines. Therefore, the projects mentioned above are demonstrating capabilities envisaged for SKA-mid but at a smaller scale. Furthermore, the challenges and solutions that we discussed in this paper or encounter in those projects could be applicable for this next generation interferometric array.

3.6 Acknowledgment

We thank for the help from the commission group and committee of MeerKAT and the help from the TRAPUM group. We thank for the help from Benjamin Hugo to the development of the Mosaic and a useful conversation on localisation with Vivek Venkatraman Krishnan. We also thank Tim Sprenger for the idea on calculating the validity time of a tiling and Jason Wu for the help with the observations. We thank the STScI digitized sky survey produced at the Space Telescope Science Institute for the optical image of 47 Tucanae. The work of this paper and the development of Mosaic was funded by BlackHoleCam, the financial support by the European Research Council for the ERC Synergy Grant BlackHoleCam (ERC-2013-SyG, Grant Agreement no. 610058) is gratefully acknowledged. The development of FBFUSE is funded by the Max-Planck-Gesellschaft. Benjamin W. Stappers acknowledges funding from the European Research Council (ERC) under the European Union's Horizon 2020 research and innovation programme (Grant Agreement No. 694745). The MeerKAT telescope is operated by the South African Radio Astronomy Observatory, which is a facility of the National Research Foundation, an agency of the Department of Science and Innovation.

CHAPTER 4

Wide field beamforming observations at MeerKAT

Pulsars have been and continue to be an important tool to explore and study the Universe. Efforts on pulsar and transient surveys are continuing with ever more powerful instruments. In this chapter, I present the ongoing observations enabled by and using the MeerKAT MPIfR beamformer developed as part of this thesis and presented in Chapter 3.

Contents

4.1 TRAPUM

Transients and Pulsars with MeerKAT (TRAPUM) is a project aiming to explore the high time resolution radio sky with the MPIfR beamformer on MeerKAT. It consists predominantly of targeted pulsar surveys of multiple globular clusters, the Galactic center, unassociated FERMI LAT sources, SNRs and PWNe. In the multi-beam search observations, the FBFUSE beamformer takes the raw voltages from all antennas and applies the directional weights calculated by Mosaic (see Chapter 3). Depending on the type of observation, the size of the beam and the target, the number of beams generated varies from 288, 480 and 768. Currently, observations are carried out at L-band centered at 1.284 GHz with a bandwidth of 864 MHz and UHF-band from 544 MHz to 1088 MHz. The beamformed data are distributed in 2048 channels with a time resolution of between 38 and 153 μs. They are multicasted back to the network and subscribed to by the APSUSE cluster (see 2.3.1 for the flow of signals), where an accelerated search pipeline is applied.

4.1.1 Observation Strategies

The TRAPUM project has planned multiple strategies to optimize the pulsar searches in different types of sources or regions. It creates an incoherent beam and a tiling of hundreds of coherent beams simultaneously. The incoherent beam has less sensitivity compared to the coherent beams but with a much larger field of view, it can be used to search for bright and sporadic sources such as giant pulses and FRBs. While each coherent beam has the combined sensitivity of all dishes and high resolving ability so that it can perform a much deeper and high spatial resolution search in crowded regions such as galactic centers and globular clusters.

The great versatility of the beamforming system allows us to tune the choice of beam pattern to the specific science question: for compact regions like globular clusters, we form beams with high overlap to increase the uniformity of the sensitivity and the localization of the detection. For FERMI sources, a low overlap ratio is used to increase the FoV of the observation according to the error bars of the FERMI detection. Regions like Small Magellanic Cloud that have multiple points of interest are covered by multiple separate tilings simultaneously. TRAPUM also follows up newly discovered pulsars. A small number of beams with an extremely high overlap ratio are formed to cover the region around the current known position so that the pulsar can be detected in multiple beams. Then the S/N of these beams can be used to improve the localization, which is demonstrated in Chapter 3.

4.1.2 Ongoing surveys

The TRAPUM project plans on surveying multiple globular clusters (GCs) to search for MSPs and exotic binary systems. Globular clusters contain a large fraction of known MSPs as their dense environment is an ideal birthplace (more detailed information in the introduction chapter 1.2.1). The flexible tiling capability of the MPIfR beamformer makes it a well-suited tool to cover these GCs. One can, depending on the scientific goals, create a tiling with the appropriate overlap to adequately enclose the optical circumference of the GCs or choose a higher overlap ratio to just cover the central region. Besides the tiling, we can time a large number of pulsars simultaneously by forming individual beams to cover all the known pulsars in the clusters with the sensitivity of all dishes combined while the traditional timing observation usually only forms 1 beam. For example, in the work of Ridolfi et al. (2021) that I co-authored, a tiling of 288 beams at an overlap ratio of 0.7 was implemented over a circular area of 2 arc minutes in radius, covering the cluster NGC 6624 as shown in Figure 4.1. In the figure, the central ellipses are the scales of a beam at the top, middle and bottom of the band, formed by the MeerKAT's own beamformer (B-engine, 2.3.1). With the tiling generated by the MPIfR beamforming platform from the TRAPUM observation (small ellipses in the same figure), we were able to localize the pulsars within a synthesized beam (solid gray ellipse) with a semi-axis ranging from 8 to 11 arcseconds (Ridolfi et al., 2021). The data of these observations are searched for pulsars using PULSAR MINER[1].

Targeted searches on SNRs, PWNe and unidentified FERMI gamma-ray sources are also being carried out in the TRAPUM project. The pulsars inside SNRs, PWNe are valuable sources for studying the interaction between the pulsar and its environment. The radio emission of the pulsar is also an important part of the multi-wavelength study of these sources. Unidentified FERMI gamma-ray sources could contain a large number of pulsars (Parkinson et al., 2016) and half of the discovered pulsars of the FERMI sources are MSP, thus performing deep target searches around these sources

[1] https://github.com/alex88ridolfi/PULSAR_MINER

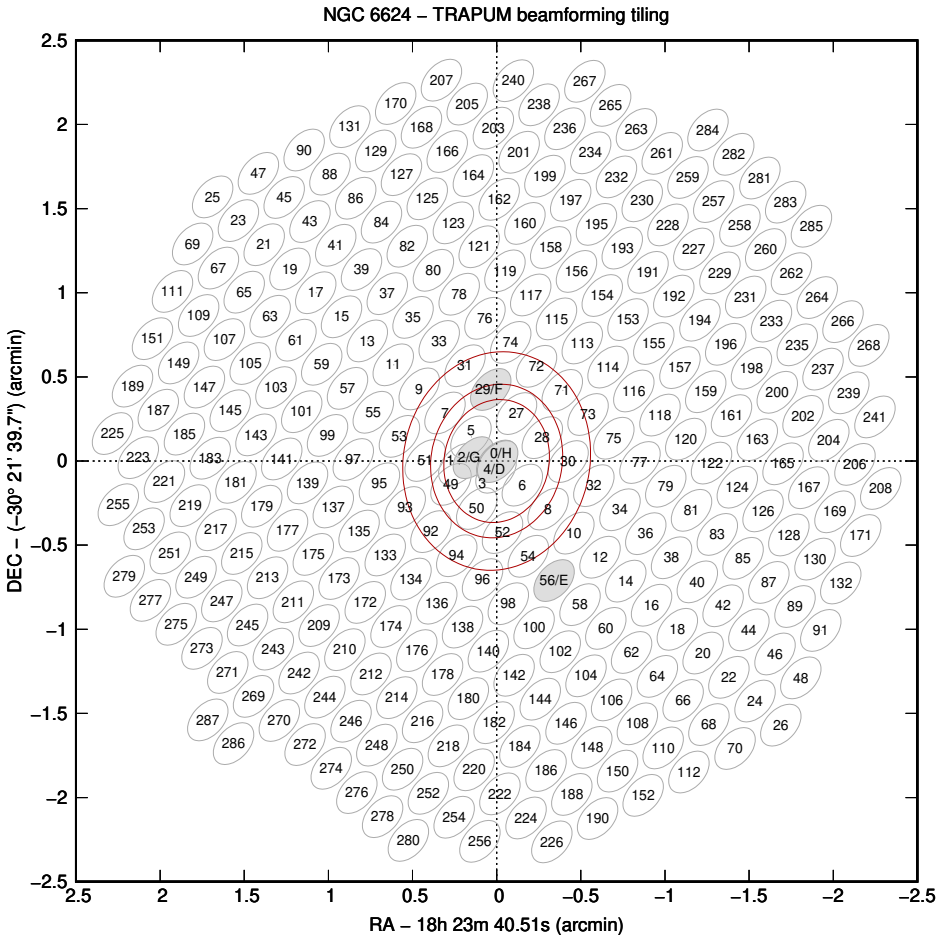

Figure 4.1: This is a tiling of a TRAPUM observation on NGC6624. It consists of 288 beams with 80% overlap, formed from 60 antennas. The beams in solid gray color indicate some of the pulsars in this cluster. The central ellipses represent a single beam at its half power response at the top, center and bottom of the band. It is provided by MeerKAT itself for pulsar timing, formed from 42 antennas from the core of the dishes.
(Ridolfi et al., 2021)

could yield promising results. As MeerKAT process higher sensitivity than Parkes, it is worthwhile to re-survey nearby galaxies in the Southern Hemisphere for extra-galactic pulsars and transients. For example, one of the most nearby galaxies, the Small Magellanic Cloud (SMC) is expected to contain a sample of radio pulsars detectable from Earth (Titus et al., 2020). Various observations on this galaxy have been carried in the TRAPUM project for pulsar searching. Figure 4.3 has shown such observation in the SMC with multiple tiling in a single pointing.

4.1.3 Results

The number of observed targets, the total number of beams per project, the lengths of the observations so far are listed in Table 4.1 and plotted in Figure 4.4. The TRAPUM project started over one year ago and at the time of writing, it has discovered 36 pulsars in various globular clusters (Ridolfi et al.,

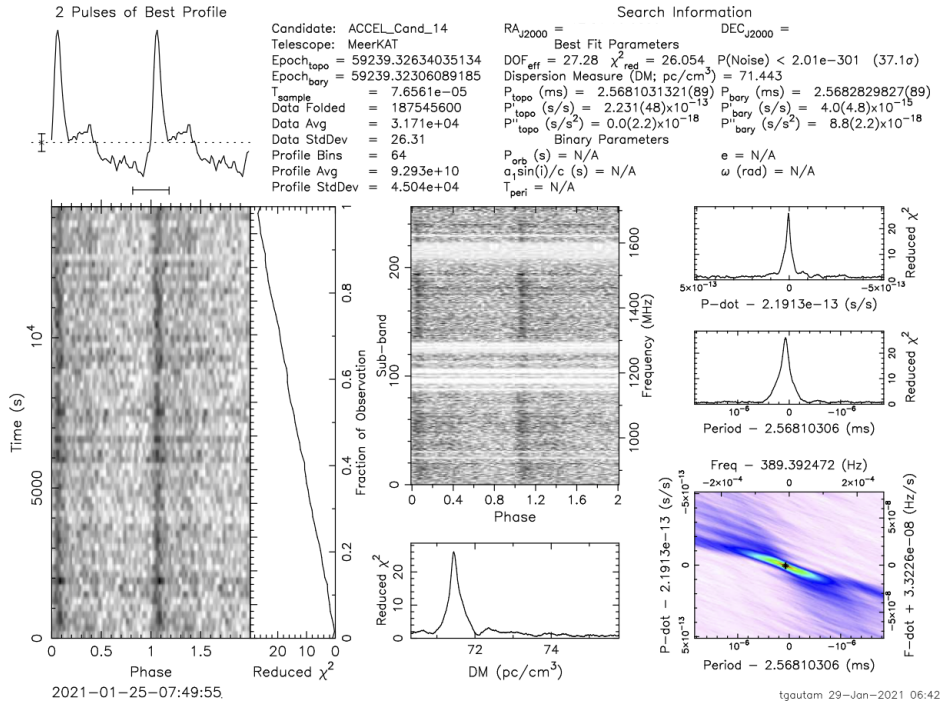

Figure 4.2: The discovery of the first millisecond pulsar PSR J1721-1936B in NGC 6342 in a TRAPUM observation (Gautam et al., in preparation). The profiles on the upper left panel are the average profiles of two consecutive rotation periods, folded from the filter bank data using `prepfold` command of the software package PRESTO (Ransom, 2001). The lower left panel is a time versus phase plot and the top middle panel is a frequency versus phase version. The bottom middle panel is the margin of the optimized DM. The two panels on the upper right are the margins of the optimized period derivative and period. The lower right panel is a period derivative versus period plot.

2021). Particularly, this project has discovered 13 pulsars in the cluster NGC 1851, while only one pulsar was discovered in this cluster in previous surveys with other telescopes. The PSR J1823-3021K has a period of 2497.896 seconds, if its association with cluster NGC 6624 is confirmed, it will be the slowest known pulsar discovered in a globular cluster. Also PSR J1721-1936B is the first millisecond pulsar in NGC 6342 (see Figure 4.2). There are 11 pulsars from unassociated FERMI sources which come from the LAT 8-year Source Catalogue (4FGL) (Abdollahi et al., 2020). Three of these pulsars were previously observed to have gamma-ray emission and an optical counterpart. The combination of those two properties is a strong indicator for redback systems (Salvetti et al., 2015), an important tool for studying stellar and binary evolution. With the detection in radio, the orbit of this system can be solved. This allows us to fold the gamma-ray photons to study the high energy emission of the pulsar (Clark et al., 2021). There are also 3 pulsars from Small Magellanic Cloud. The full list of discoveries is published in a webpage of the project [2].

[2] http://trapum.org/discoveries.html

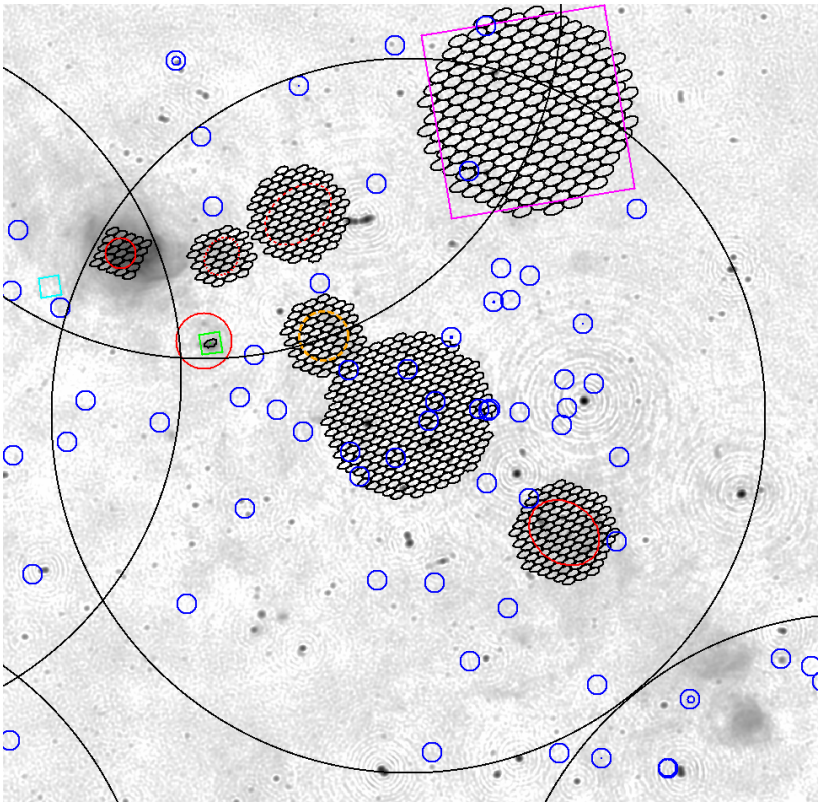

Figure 4.3: TRAPUM nearby galaxies observations on the Small Magellanic Cloud. This plot shows that multiple tilings can be created in a single pointing to cover multiple separated regions or individual sources. The solid large circles are individual pointings. the small black ellipses are individual beams. The blue circles are High-mass X-ray Binaries from Haberl and Sturm (2016), the yellow dashed circles are Supernova remnant (SNR) candidates from Titus et al. (2019), the red and rad dashed circles are SNR and SNR candidates from Maggi et al. (2019), the green square is a pulsar wind nebula, the pink squares are radio pulsars, the cyan square is an x-ray only pulsar. The plot is by courtesy of Emma Carli.

Table 4.1: The total number of beams, observation lengths and unique target count at the time of writing for different survey projects of TRAPUM and MGPS.

Target	Total number of beams	Total hours of observations	Unique target count
Globular cluster	16345	156	20
FERMI	58883	42	93
Galatic plane (MGPS)	767840	251	1499
Nearby Galaxy	3528	16	20

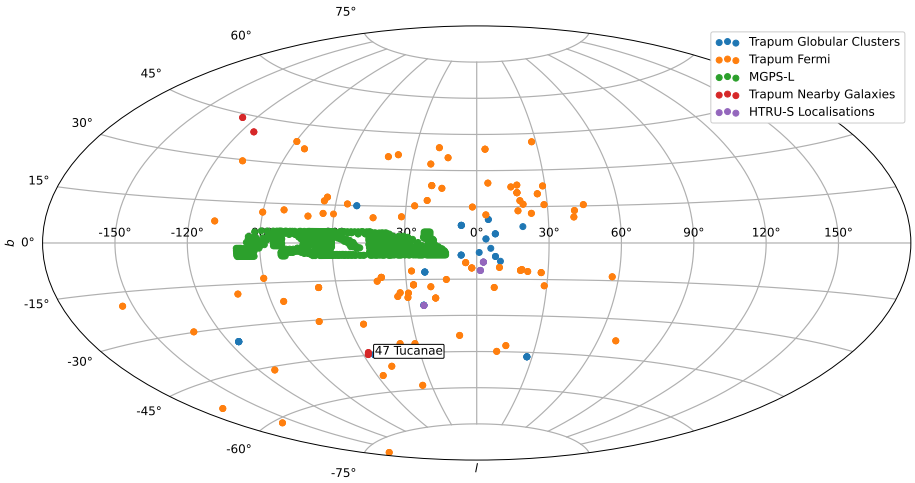

Figure 4.4: The TRAPUM and MGPS survey pointings that have already been observed at the time of writing. Each dot in the plot represents a single pointing with one or multiple tilings of synthesized beams. Individual synthesized beams are not plotted. The "HTRU-S Localisation" denotes the sources that were originally discovered by HTRU-S, then re-observed and localized by TRAPUM.

4.2 MGPS

The MPIfR Galactic Plane Survey (MGPS) is a project to search pulsars in the Galactic plane at both L-band and S-band. Pulsars are known to be born in supernova explosions. They should be expected in regions of high stellar density, which makes the Galactic plane a favorable place to carry out pulsar surveys. A Galactic survey could discover young and energetic pulsars which could be used to study the stellar and Galactic evolution. Moreover, the Galactic plane is expected to contain samples of relativistic binary systems which can be used to test General Relativity and other gravitational theories. Because such tests require highly relativistic systems and high precision timing (Wex and Kramer, 2020).

Previously, such an effort has been carried out by the Parkes telescope in Parkes multi-beam pulsar survey (Manchester et al., 2001) and HTRU-South low-latitude Galactic plane pulsar survey (Ng et al., 2015; Cameron et al., 2020). Now with the highest sensitivity in the Southern Hemisphere, re-visiting the Galactic plane with MeerKAT will produce a much deeper pulsar survey of the region.

Searching for pulsars orbiting Sgr A* and probing the environment around the Galactic center at S-Band is another important objective of MGPS. The interaction between Sgr A* and its surrounding pulsars provides a unique laboratory to test the theory of General Relativity in the strong-field regime. This is because that pulsar timing provides high-precision measurement of the relativistic effects that are significant near massive blackholes (Kramer, 2004). However, the higher free electron density toward the Galactic center poses challenges to the previous survey because of the dispersion and scattering effects (Lazio and Cordes, 1998; Cordes and Lazio, 2002). Observing these regions with S-band receivers, we can obtain a better S/N of the signals. As can be seen from the relationship between the scattering timescale and the observing frequencies: $\tau_{SC} \propto \nu^{-4.4}\mathrm{DM}^{2.2}$, assuming a purely Kolmogorov distribution of inhomogeneities (Romani, Narayan and Blandford, 1986; Bansal et al., 2019), the effects of scattering are less severe at high frequency, thus making it easier to discover

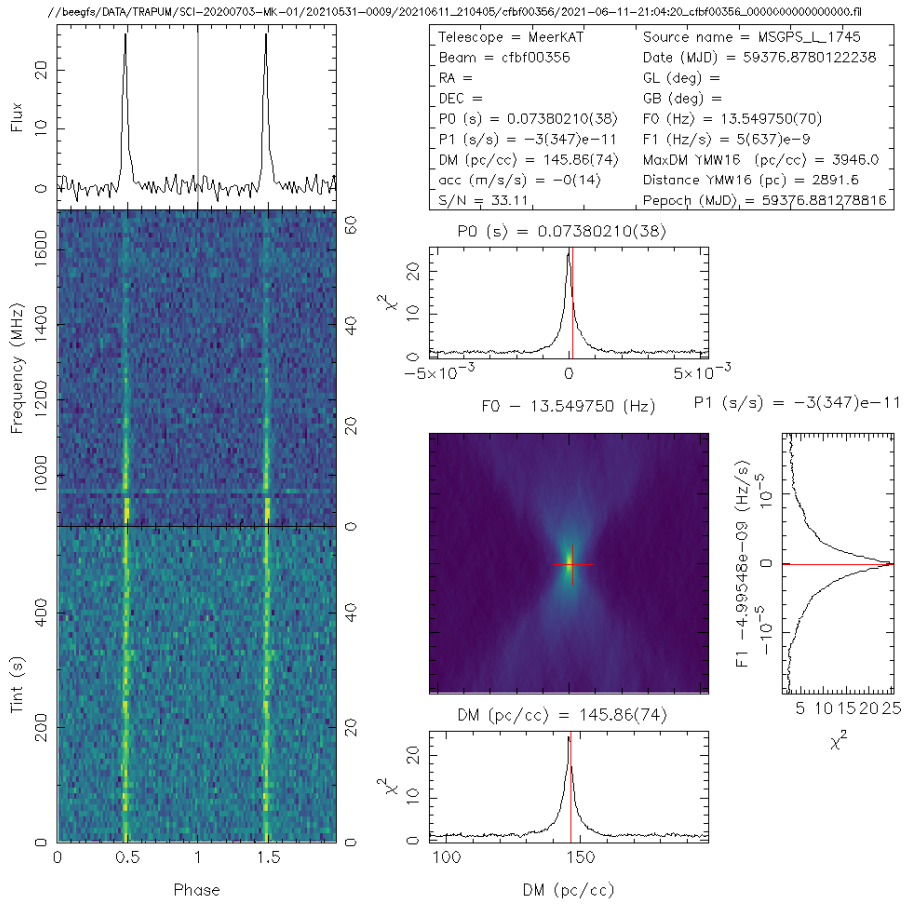

Figure 4.5: Detection of PSR J1212-5838. The profiles on the upper left panel are the average profiles of two consecutive rotation periods, the middle left panel is a frequency versus phase plot, the lower left panel is a time versus phase plot version. The lower middle panel is the margin of the optimized DM. The second panel from the top in the middle is the margins of the optimized period. The middle right panel is the margins of the rotation frequency derivative. The middle panel is the two dimension version of the marginal of the optimized rotation frequency versus its derivative.

sources with high DM and scattering (Lorimer and Kramer, 2004). This survey will form 480 beams with the core array of MeerKAT. The data are searched using PEASOUP[3].

4.2.1 Results

The observed pointing and observation lengths are listed in Table 4.1 and plotted in Figure 4.4. At the time of writing, the MGPS project has discovered 21 pulsars[4] with a large fraction of them being millisecond pulsars. Figure 4.5 is an example of a pulsar detection of this project. In these newly discovered pulsars, PSR J1449-6339 is likely to be a double neutron star system (DNS), because the characteristic of the spin period is similar to other DNSs. For PSR J1208-5936, it is very likely a DNS according to the preliminary determination of its orbit. DNSs are important tools to perform tests on strong-field gravity (see an example in the Introduction 1.2.1).

4.3 MeerTRAP

The Meer(more) TRAnsients and Pulsars (MeerTRAP) is a project to search pulsars and fast transients in the radio sky with the MeerKAT array. One important aspect of the project is that the observations run commensally with almost all MeerKAT observations which provide ample time and sky coverage. During the commensal observation, MeerTRAP independently performs high resolution and real time radio transient search.

MeerTRAP takes data from FBFUSE and performs a single pulse search pipeline in the Transient User Supplied Equipment (TUSE) instrument developed by the MeerTRAP team at the University of Manchester. In the coherent mode, 768 coherent beams are formed by the beamformer inside FBFUSE with the data from 44 dishes of the inner core and multicasted to the MeerKAT internal network to which TUSE subscribes. The real time single pulse search pipeline in the TUSE performs an incoherent de-dispersion process on the beamformed data with a range of DM values. While in the incoherent mode, it combined the data from all the participated antennas to form one incoherent beam with less sensitivity but a much larger field of view.

One of the advantages of the MeerTRAP project is the application of the transient buffer. It is a First-In-First-Out (FIFO) temporary storage for the latest raw voltages from all dishes of the array. This enables the instrument to preserve the original time, frequency and phase resolution of the data stream for a short period of time (30 seconds for the current configuration) so that a raw voltage dump can be triggered whenever a highly rated candidate appears in the realtime search pipeline (Stappers, 2016). The raw voltages can be processed immediately or transferred to permanent storage, in either case, it can be used to improve the sensitivity because it contains the data of the full array, or to make a high spatial resolution image using the longer baselines and even to perform another beamforming process with different tiling strategies.

To date, MeerTrap is an ongoing project and its data are being processed. A target observation focused on the repeated FRB 121102 was successfully carried out to study its periodicity and frequency drifting phenomenon (see Figure 4.6, Caleb et al., 2020). The high sensitivity and wide bandwidth reveal the complex frequency structures of the detected bursts and provide a rare opportunity to study the behaviors of the burst in lower frequencies.

[3] https://github.com/ewanbarr/peasoup
[4] http://trapum.org/discoveries.html

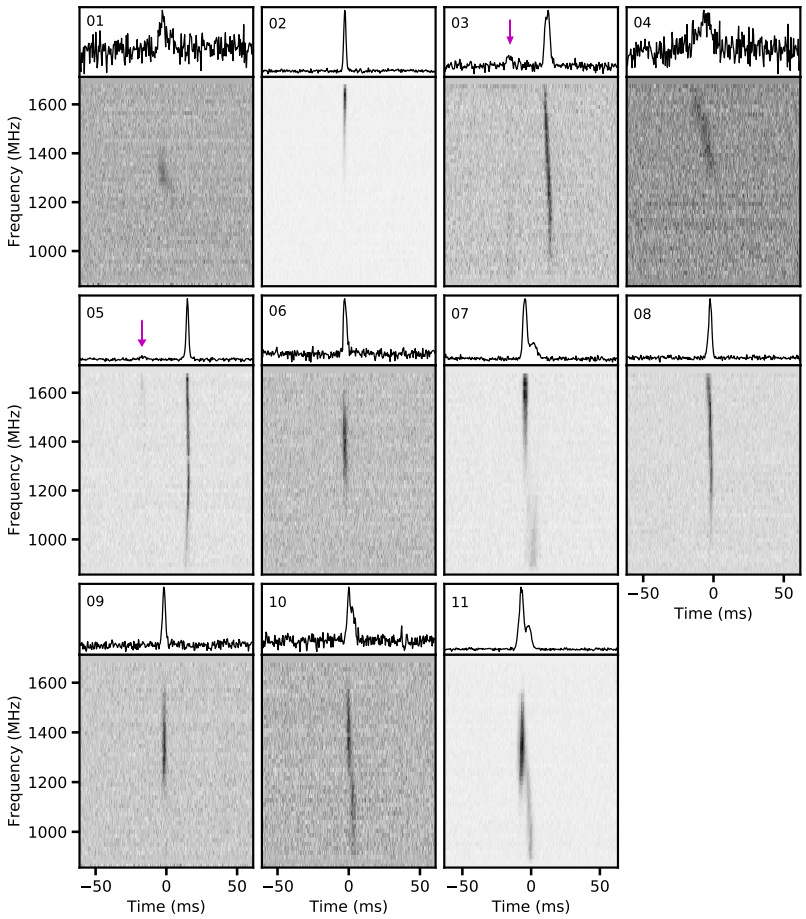

Figure 4.6: Dynamic spectra of the detections of FRB 121102 in the MeerTRAP observation (Caleb et al., 2020). Burst 3 and 5 have been seen to have precursor bursts denoted by the red arrows.

4.4 Deeper Wider Faster

Deeper, Wider, Faster (DWF) is a program utilising over 30 multi-wavelength astronomical instruments or observatories to search for fast transients. In an effort to capture fast transients in different time scales and their counterparts in different wavelengths, the program consists of 4 components: (1) A simultaneous multi-wavelength observation coordination for the same sky region, (2) real-time fast-transient detection with high-performance data processing pipelines and rapid candidate identification algorithms, (3) swift follow-up triggering system for fast optical imaging and high energy instruments, (4) long-term follow up by a greater number of instruments in the global network for evolving events and subsequent comprehensive identification.

MeerKAT has taken part in this global effort and is responsible for covering the radio regime in the South Atlantic region during simultaneous observations (Andreoni and Cooke, 2019). The MPIfR beamformer was used to generate coherent beams during the DWF observations. From Jun 24 to Jun 28 in 2019, there were a series of 5-hour DWF sessions, observing NGC 6101, NGC 6744 and FRB 182924. In these observations, 480 beams were generated around the target region with the full

bandwidth of the L-band receiver, 4096 channels and a sampling rate of 306.24 microseconds. The beamformed data were delivered to a single pulse search pipeline with a de-dispersion threshold up to 5000 pc cm^{-3}. The highly rated candidates from the search pipeline were then transferred to a web server that can be accessed by human inspectors. On the website, the candidates were plotted and organized in a candidate viewing interface.

There were no new detections in the observation of FRB 182924 and other sources. However, during the test period before the DWF sessions, the pipeline successfully picked up the known RRATs such as RRAT J1554-5209 with multiple single pulse detection, demonstrating that the system worked as expected.

4.5 SGR 1935+2154 observations

Soft Gamma-ray Repeater (SGR) 1935+2154 was discovered by Swift's burst Alert Telescope (BAT) and is considered to be associated with the supernova remnant G57.2+0.8 (Gaensler, 2014). This outburst had a soft X-ray spectrum (Lien et al., 2014) and given the low galactic latitude of the source, it is a candidate to be a magnetar. This hypothesis was confirmed by Israel et al. (2016) in their Chandra observation that revealed the source has a 3.25-second spin period. This magnetar is very active with multiple subsequent outbursts detected (e.g. Kozlova et al., 2016) but more than half of a decade after the discovery, there was no continuum or pulsating radio emission detected despite multiple radio observations carried out by VLA, Parkes and GMRT.

In the recent active period of this magnetar, CHIME and the Survey for Transient Astronomical Radio Emission 2 (STARE2) radio telescope both independently detected a very bright radio bust on April 28, 2020 (CHIME/FRB Collaboration et al., 2020; Bochenek et al., 2020). The brightness of this burst has exceeded that of the brightest radio burst ever detected inside the Galaxy by several orders of magnitudes. It is so bright that if this burst were to originate from a nearby galaxy, then to an observer on Earth it would appear like an FRB. The discovery sparked global follow-up observations as it supports the hypothesis that a magnetar's emission, or its interaction near the environment, could be the progenitor for at least a subset of FRBs.

According to the detections from different radio instruments, this magnetar shows a great variety in the emission power, it is clearly important to have a more complete picture of the emission activity through a wider window in the radio regime so that spectra analyses can be performed to test against different emission model. Therefore, a simultaneous multi-wavelength radio observation campaign was carried out from the 11th to the 15th of May 2020 (Bailes et al., 2021). This campaign utilizes telescopes of different types and observation frequencies such as Arecibo in L-band, Effelsberg in L-, S- and C-band, Lofar HBA tied-array beams, MeerKAT's PTUSE, TUSE and imaging backend in L-band twined with the optical wide-field imager MeerLICHT, MK2 in L-band and Northern Cross in 400–416 MHz.

The TUSE backend of MeerKAT performed the MeerTRAP real-time single pulse search during the observation campaign. It invoked the MPIfR beamformer in the process to generate beams with full bandwidth using the data from 40 antennas of the core, creating a tiling of 768 beams with an overlap ratio of 0.25 around the sky region of the magnetar.

There is no credible candidate found from the mentioned radio telescopes with upper fluence limits between 25 mJy and 18 mJy ms. Though there are multiple X-ray bursts that were detected by the Hard X-ray Modulation Telescope (HXMT) when MeerKAT and Effelsberg were observing the source.

So these X-ray bursts do not seem to have corresponding counterparts in the radio observations. The MeerLICHT optical imager also does not detect any continuum or transient source.

The non-detection indicates that the radio emission of the magnetar is highly variable and the X-ray outbursts from this source do not necessarily have associated radio emission. It is also possible that the bursts occurring in the active phase were produced by a different mechanism.

4.6 Conclusion

The wide-field, high time and spatial resolution capability of the MPIfR beamformer has made MeerKAT become a powerful instrument for fast transient surveys. These observations and surveys have shown that my beamforming software works as planned and enables the discovery of 66 pulsars[5]. It also demonstrated that raw-voltage beamforming is a suitable choice for high time resolution science with dense Gaussian-distributed array like MeerKAT.

[5] http://trapum.org/discoveries.html

CHAPTER 5

Searching for giant pulses using Effelsberg telescope

Contents

5.1 Introduction

5.1.1 The phenomenon of Giant pulses

Despite decades of study, a complete picture of the pulsar radio emission mechanism has remained elusive for not a single model can explain various observed properties such as the sub pulse structure (Backer, 1970a), moding (Backer, 1970b), nulling (Backer, 1970c) and so on. One of its mysteries is the phenomenon of giant pulses (GPs): individual pulses that are hundreds of times brighter than the average pulse. Other than the brightness, GPs exhibit various differences compared to normal individual pulses. The distribution of the pulse energies of the GPs closely follows a power law distribution as shown in the top panel of Figure 5.1 (Argyle and Gower, 1972), while the normal pulses follow a Gaussian or exponential distribution as shown in the bottom panel of Figure 5.1 (Hesse and Wielebinski, 1974). They are also much narrower than the average pulse emission envelope and ranges from milliseconds to nanoseconds, indicating a smaller emission region. Some of the giant pulses are confined in a small phase window, which could mean the emission comes from a specific region in the magnetosphere.

These differences prompt a debate on whether the giant pulses and normal pulses are created by the same mechanism. For example, Lyubarsky (2018) proposed that there may be two different emission mechanisms behind the observed pulses: one that mostly occurs on the ordinary pulsars, originating from the polar cap and exhibiting a widened width with decreasing observational frequency. The other mechanism which is shared by a number of giant pulse emitters, mostly manifests in millisecond pulsars that possess a large magnetic field at the light cylinder (B_{LC}). In this situation, emission originates at or beyond the light cylinder and there is very little frequency dependence on the width of the pulse.

More intriguingly, high energy emission has been found to be common among these GP emitters. High energy activity indicating that these pulsars are highly energetic, which is consistent with their relatively high spin-down luminosities (a measure of the loss of a pulsar's rotational energy, hereon referred to as $\dot{E}$). (Cusumano et al., 2003, Romani and Johnston, 2001b). Therefore, several studies focused on the correlation between giant pulse emissions and high energy emissions. The observation of PSR B1821-24 (Romani and Johnston, 2001a), PSR J0218+4232 (Knight et al., 2006a), PSR B0531+21 (Enoto et al., 2021) and some other pulsars shows that the X-ray emission is almost in phase with the giant pulse emission, promoting the idea that the giant pulse is created in the same region where the high density of the pair produces the high energy emission. On the other hand, there is no evidence for a phase correlation between gamma-ray and GP emission (Lundgren et al., 1995; The MAGIC Collaboration et al., 2008).

5.1.2 Emission mechanism of giant pulses

A number of mechanisms have been proposed to explain giant pulses. Here I mainly discuss the models that involve induced Compton scattering and magnetic re-connection.

Induced Compton scattering

Petrova (2004) suggested that the GPs are products of induced Compton scattering off the plasma particles. Highly magnetised particles of high density inside the inner magnetosphere travel along the open magnetic field lines and are accelerated to relativistic speed. The photons of different frequencies

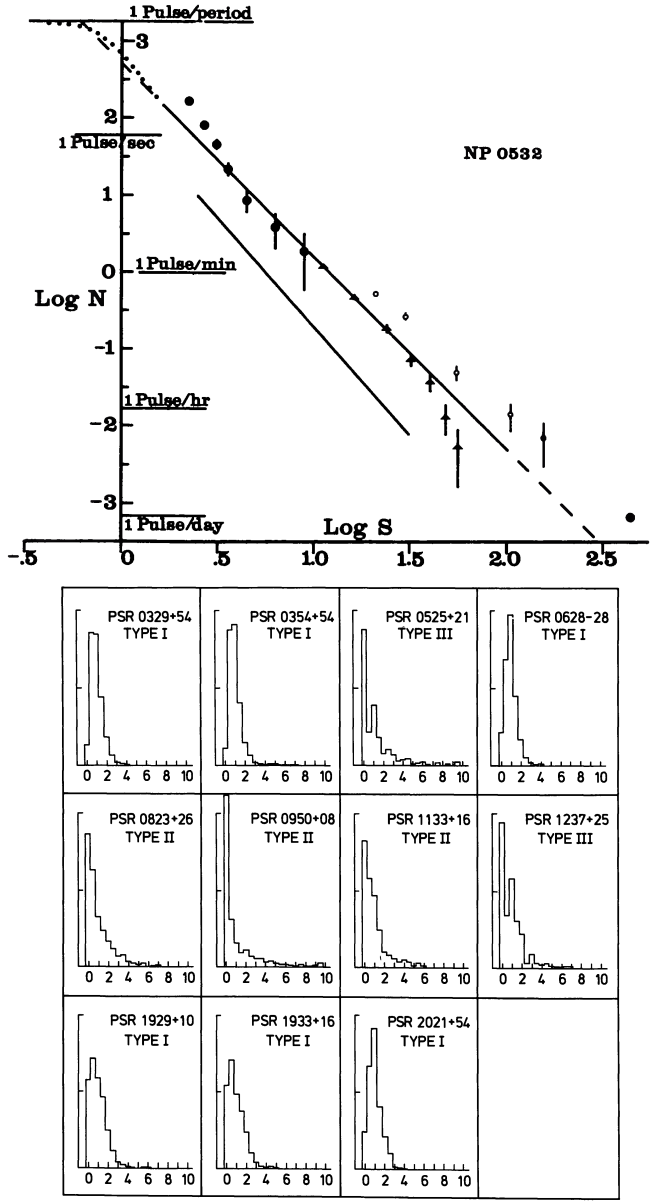

Figure 5.1: Distribution of pulsar energy of normal pulses and giant pulses. The top panel shows the logarithm of the number of giant pulses of PSR B0531+21 per minute above threshold versus the logarithm of the threshold strength in unit of the average pulse strength. the solid line is $\log N = 500 \log S^{-2.5}$ (Argyle and Gower, 1972). The bottom panel shows the pulsar intensity histogram of 11 pulsars. The shape of the histogram follows exponential distribution or binomial distribution or both (Hesse and Wielebinski, 1974).

and emission regions could be transferred to high frequency beams while interacting with these plasma particles through induced Compton scattering (Melrose, 1971) . Numerical simulations show that the efficiency of this beam-to-beam scattering process could significantly amplify the energy of the photons up to 1000 times, which could explain the brightness of the observed giant pulses.

Magnetic re-connection

Istomin (2004) proposed that GPs are created in magnetic field line re-connection events in the pulsar magnetosphere. The region between the null line (defined in Section 1.2.1) and the light cylinder is unstable and thus provides a cradle for magnetic field re-connection. In Istomin's model, the magnetic field lines from different poles connect near this region caused by the turbulence of the plasma near the light cylinder. As the magnetic field line come from the two poles, the connection stimulates electric discharges which accelerate the charged particles. These particles move along the magnetic field lines and multiply themselves. If the density is high enough, an Alfvén wave could be formed through maser amplification.

Another model based on re-connection event is proposed by Lyutikov (2007), stating that the giant pulse could be generated on closed magnetic field lines near the light cylinder, as illustrated in Figure 5.2. This model requires the existence of high density plasma on the closed lines and when the re-connection occurs, high Lorentz factor beams are created from the plasma due to large potential drop along the field lines. While these relativistic beams propagate along the magnetic field, they emit coherent cyclotron Cherenkov radiation through anomalous cyclotron resonance, which could manifest as the observed giant pulse.

There are also models suggested that the plasmoids or "island" in the current sheet could be responsible for the observed "nanoshots". The merger of two big plasmoids (see Figure 1.8) creates several smaller plasmoids in the perpendicular current sheet between the two big ones (see Section 1.2.1). These small plasmoids would again merge in the upstream electric fields, creating a bunch of electric spikes as shown in Figure 5.3. The intervals of these spikes are consistent with the timescale of the nanoshots observed on the Crab pulsar (Philippov et al., 2019; Eilek and Hankins, 2016). Another model proposed by Lyubarsky (2018) suggests that the reconnection occurs when the magnetic islands form or coalesce with each other. The coalescence produces magnetic perturbation, whose amplitude is comparable with the strength of the background field. These magnetic perturbations propagate away in the form of radio waves. In their work, the estimated duration and the flux of these radio waves are comparable with the observed nanoshots from the Crab pulsars.

5.1.3 Giant pulse as a model for Fast radio bursts

The extraordinary brightness of giant pulses makes them observable from other galaxies (McLaughlin and Cordes, 2003; Johnston and Romani, 2003). It has been proposed that a (super) giant pulse from young energetic pulsars in other galaxies could be the origin of Fast Radio Bursts (FRBs), a type of bright, millisecond-duration and extra-galactic radio transient (see Introduction at 1.2.2). Lyutikov, Burzawa and Popov (2016) suggested that the ejected supernova shell could contribute to the high Dispersion Measure (DM) of the FRBs. Another work from Muñoz, Ravi and Loeb (2020) proposed that the periodic super giant pulse from neutron stars could explain the repeated FRBs that show potential periodic occurrences.

Another model is the radio burst from a magnetar, supported by a recent detection of an extremely

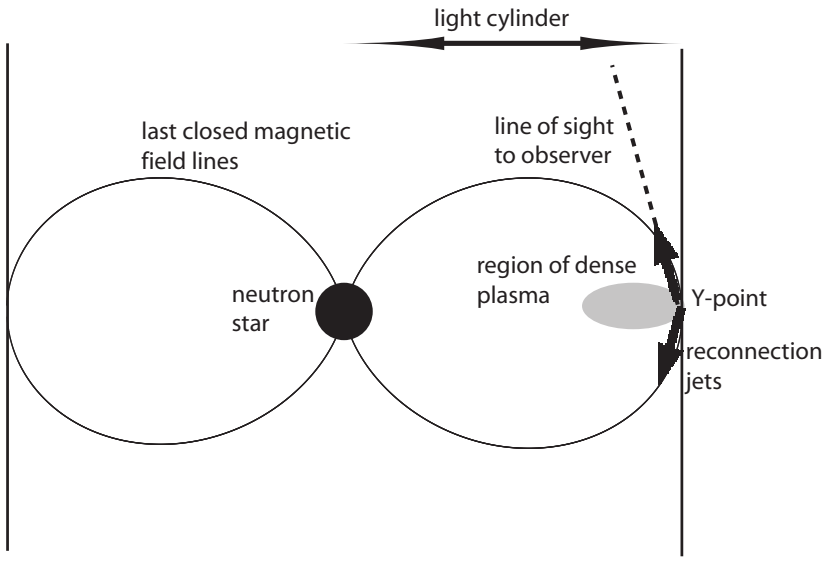

Figure 5.2: Re-connection model for giant pulses. (Lyutikov, 2007)

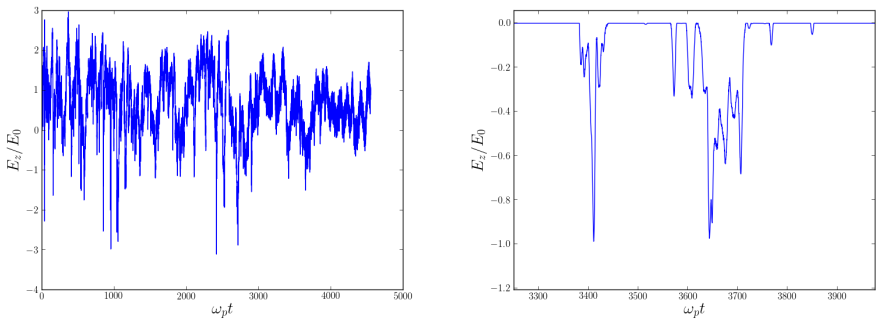

Figure 5.3: On the left is the simulated electric fields created by mergers of plasmoids. A zoom-in version is shown on the right. The Y axis is the normalized reconnection electric field, Ω_p is the background plasma frequency. (Philippov et al., 2019)

bright radio burst from a galactic magnetar (CHIME/FRB Collaboration et al., 2020). Although this event is the brightest radio burst ever detected in the Galaxy, it does not exclude the possibility that some of the current FRBs are extra-galactic GPs because the power distribution of the FRBs and GPs are not fully explored. A larger population of giant pulses could shed light on this situation.

5.2 Searching for giant pulses

This project aims to further increase the population of giant pulse emitters so that we can test and further investigate the relationship between the giant pulse and the high energy emission from pulsars, which could help to solve the puzzle of the creation of giant pulses. In addition, a larger population could help to study the variety of GPs and perform population analyses to check the giant pulse theory for FRBs. Furthermore, the more we understand giant pulses, the more we can study the emission mechanism of pulsars, which is an unsolved enigma since they were discovered.

Previously, there was an attempt to search for giant pulses in Vela-like pulsars (Johnston and Romani, 2002). Their criteria were to search in pulsars with small spin periods and/or small age coupled with high flux density at 1500 MHz and pulsars with high energy emission. They found evidence for potential giant micro-pulses in PSR B1706−44, which are also observed in the Vela pulsar. These occurrences of giant micro-pulses are not aligned with the main pulses, indicating that they may come from a different emission region (Kramer, Johnston and van Straten, 2002). A giant pulse search targeting 18 millisecond pulsars was carried out with the Parkes 64-meter radio telescope using baseband recording and coherent de-dispersion techniques (Knight et al., 2005). They detected strong microsecond-timescale giant pulses from PSR J1823−3021A. Another search targeting millisecond pulsars was carried out by Joshi et al. (2004) using the Giant Metrewave Radio Telescope. They selected millisecond pulsars with a non-thermal high energy emission and a range of B_{LC} as candidates, within which significant large amplitude pulses were found on PSR J0218+4232 and PSR B1957+20. With the 100-meter Green Bank Telescope, Knight et al. (2006b) discovered very short intrinsic duration giant pulses on PSR J0218+4232. Table 5.1 is a list of GP emitters with some of their properties sorted by the strength of the magnetic field at the light cylinder. The values are taken from PSRCAT[1] (Manchester et al., 2005).

5.2.1 Selecting criterion on giant pulse emitter candidates

Figure 5.4 shows all known pulsars plotted on a $\dot{E}$-B_{LC} diagram. As we can see in the figure, there are generally two groups of giant pulse emitters (in triangles) depending on whether they possess high $\dot{E}$ and high B_{LC}. Whether the group with lower $\dot{E}$ and B_{LC} (bottom left) are giant pulse emitters is a matter of debate. Because some of them, such as PSR B0031-07 and PSR B1112+50, do not show a clear power law distribution in the pulse energy (Karuppusamy, Stappers and Serylak, 2011). Moreover, the giant pulse detections of the aforementioned pulsars (Kuzmin and Ershov, 2004; Ershov and Kuzmin, 2003) were only detected in low frequency observations and the flux density at lower frequencies is usually hard to calibrate because of stronger ISM effects and bigger FoV which could include more bright sources at a given time. The other group, however, shows a strong correlation with high energy emission (with symbol ⅄) and is very well constrained in the upper right corner. In

[1] https://www.atnf.csiro.au/research/pulsar/psrcat/

Table 5.1: Current known giant pulse emitters. They are separated into two groups, one is with $B_{LC} > 10^5 G$, the other is not. More discussion about the differences between these two groups is in Section 5.2.1

Pulsar name	Period (ms)	$\dot{E}$ (erg s^{-1})	B_{LC} (G)	γ−ray
B1937+21	1.56	1.1×10^{36}	1.02×10^{6}	Y
B0531+21	33.39	4.5×10^{38}	9.55×10^{5}	Y
B1821-24A	3.05	2.2×10^{36}	7.40×10^{5}	Y
B1957+20	1.61	1.6×10^{35}	3.76×10^{5}	Y
B0540-69	50.57	1.5×10^{38}	3.61×10^{5}	Y
J0218+4232	2.32	2.4×10^{35}	3.21×10^{5}	Y
B1820-30A	5.44	8.3×10^{35}	2.52×10^{5}	Y
B0656+14	384.89	3.8×10^{34}	7.66×10^{2}	Y
B0950+08	253.07	5.6×10^{32}	1.41×10^{2}	N
J1752+2359	409.05	3.7×10^{32}	7.11×10^{1}	N
B0529-66	975.72	6.6×10^{32}	3.97×10^{1}	N
B1133+16	1187.91	8.8×10^{31}	1.19×10^{1}	N
B0031-07	942.95	1.9×10^{31}	7.02×10^{0}	N
B0301+19	1387.58	1.9×10^{31}	4.76×10^{0}	N
B1112+50	1656.44	2.2×10^{31}	4.24×10^{0}	N
B1237+25	1382.45	1.4×10^{31}	4.14×10^{0}	N

this perspective, searching giant pulses in this group is likely to be more efficient than searching the other group.

Since the FERMI Gamma-ray Space Telescope began to operate in 2008, the number of gamma-ray sources has been greatly increased. These new gamma-ray sources contain a large sample of energetic pulsars (Abdo et al., 2010) that are good candidates for GP searches. As such, I used high $\dot{E}$ and high B_{LC} as criteria to select pulsars for potential GP emitters and selected 13 gamma-ray pulsars with radio detection with $\dot{E}$ larger than 0.2×10^{35} $erg\ s^{-1}$ and B_{LC} larger than 0.6×10^5 G (green circles). Of these, 8 have positions that are inside the Effelsberg telescope's field of view.

5.2.2 Effelsberg Observation configuration and data products

Eight observations were carried out with the Effelsberg 100-meter telescope intermittently between May, 11 2019 and June, 7 2020. Table 5.2 lists the source and duration of each observation. The P217mm 7-Beam 21 cm primary focus receiver was used in all observations. After the feed horns receive the astronomical electromagnetic radiation, they are sent into Orthomode transducers (OMTs) that separate the signal into two hands of circular polarization. These two channels of signals are amplified by low noise amplifiers (LNAs) and filtered by a bandpass so that only the component between 1210 MHz and 1570 MHz are retained. In the next stage, the signals are down converted to intermediate frequencies (IF) of 80 MHz to 200 MHz by a mixer with a local oscillator (LO). This down-conversion process is also called superheterodyne which transfers the original signal to another signal regime that is often much easier to process. These down converted signals are sampled

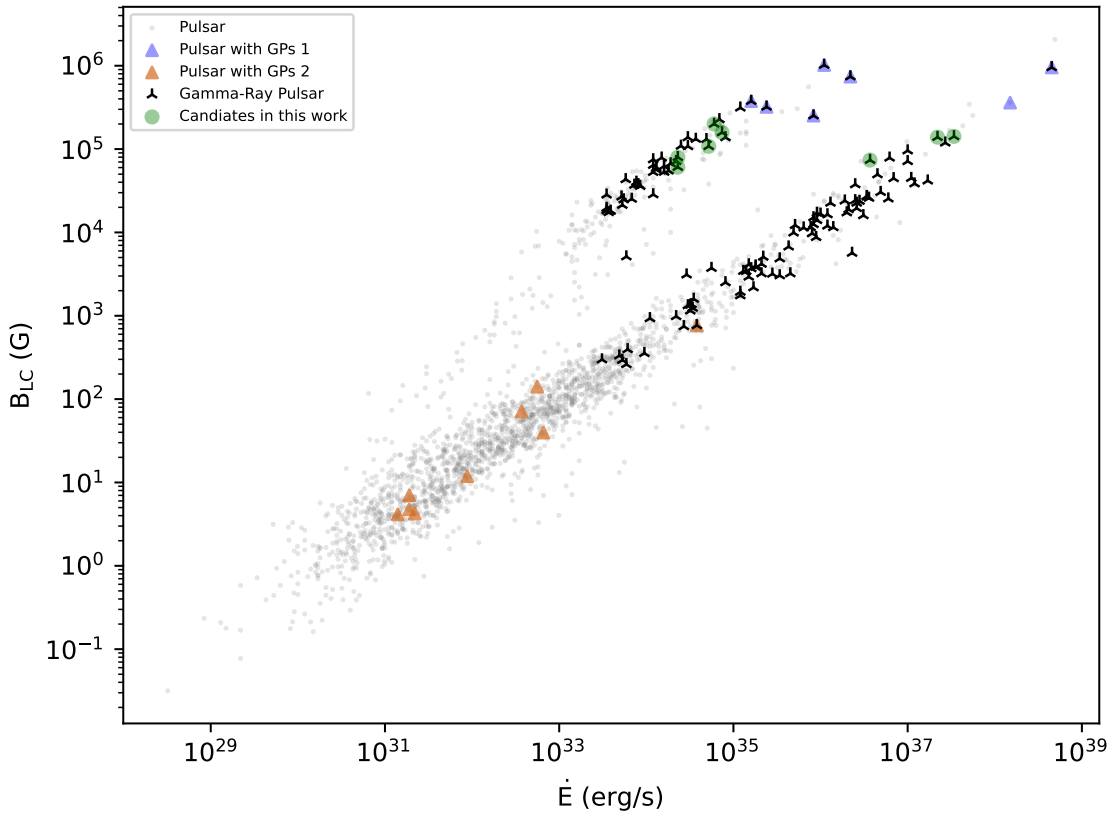

Figure 5.4: Known giant pulse emitters and observation candidates. All the known pulsars are plotted in gray by their B_{LC} against $\dot{E}$. The ones in blue are one group of the known giant pulse emitters with high B_{LC} and high $\dot{E}$, the ones in dark orange are the other group of know giant pulse emitters that have lower B_{LC} and $\dot{E}$, the ones in black are pulsars with high energy emission and the ones in green are the selected candidates for the search.

Table 5.2: Source list

Pulsar name	Period (ms)	DM (pc cm^{-3})	$\dot{E}$ (erg s^{-1})	B_{LC} (G)	T_{obs} (hour)
J1816+4510	3.19	38.89	5.2×10^{34}	1.08×10^{5}	1.8
J1833−1034	61.88	169.50	3.4×10^{37}	1.42×10^{5}	2.3
J1843−1113	1.84	59.96	6.0×10^{34}	2.00×10^{5}	1.4
J1952+3252	39.53	45.01	3.7×10^{36}	7.38×10^{4}	3.0
J2215+5135	2.60	69.20	7.4×10^{34}	1.58×10^{5}	3.0
J2229+6114	51.62	204.97	2.2×10^{37}	1.39×10^{5}	2.5
J1741+1351	3.74	24.20	2.3×10^{34}	6.07×10^{4}	3.0
J2339−0533	2.88	8.72	2.3×10^{34}	7.97×10^{4}	2.5

as baseband data covering a frequency range of 0 ~ 320 MHz. This process also goes through a digital backend where analog to digital conversion (ADC) and packetization is done. The ADC has a sampling time of 1.5625 nanoseconds (corresponding to a sampling rate of 640 MHz) and is centered at 1.36 GHz with two polarizations. The resulting data rate for 8-bit digitisation and two polarisations is 1380 MB/s, which is captured and stored as 10s-long data files on a high performance storage system.

The sensitivity and SEFD of this receiver system[2] are 1.55 K/Jy and 15 Jy. The baseband data of the observation were kept after the observation until it was converted to filterbank files.

5.2.3 Data reduction and search pipelines

DSPSR

I first created a pipeline to perform the search using DSPSR[3] (van Straten and Bailes, 2011), a Digital Signal Processing library for pulsar data. It reads data from data files and splits them into a user-specified number of channels. Then the channelized data go through a coherent de-dispersion process using the DM value of the pulsar to remove both the inter-channel and intra-channel dispersion. After that, all dispersion delays are removed, and the pulsar signal is aligned in phase. In the next step, DSPSR slices the dedispersed and channelised data into files containing individual pulses according to the pulsar's period. These individual pulses are then tested against the user's criterion such as a threshold for S/N and the ones that pass are output as candidates. The candidates are in the format of pulsar archive files which can be processed and plotted by PSRchive[4] (van Straten et al., 2010), a tool for manipulating the pulsar archive files for manually visual inspection.

Before searching for giant pulses on the observed pulsars of this project, I carried out an experiment on a known giant pulse emitter B1937+21 to assess the performance of the DSPSR pipeline. During the test, I noticed that the number of detection is very sensitive to any variation in the DM. For example, the DM value of PSR B1937+21 from Desvignes et al. (2016) is 71.0237 cm^{-3} pc with which DSPSR picked up significantly fewer candidates compared to the result of McKee et al. (2019). After trying a range of DM values with DSPSR on this data, I discovered that a DM value of 71.0179 cm^{-3} pc is more optimal for the observational data we used. That is because the detection mechanism of DSPSR evaluates the combined power of all channels, while the power of the signal in each channel is no longer aligned in phase if an inappropriate DM value is used. The misalignment will smear the signal and decrease the S/N of the detection.

Slight variation of the DM is not uncommon for pulsars (You et al., 2007; Cordes, Shannon and Stinebring, 2016) because of the continual changes of the interstellar environment between the observer and the pulsar and it normally does not have a large effect on the average profile of the pulsar. However, this smearing effect is only negligible when its scale is much less than the width of the targeted structures. Giant pulse search is very susceptible to this effect because most of the observed width of a giant pulse is at the scale of microseconds or less. If a signal is relatively bright and still visible even with the deviated DM value, we can use the program `pdmp` of the PSRCHIVE package, which searches in a range of DM values and Barycentric periods to locate the best values that produce the highest S/N for the pulse. Then we use this optimized value to perform the search again on the

[2] https://eff100mwiki.mpifr-bonn.mpg.de/doku.php?id=information_for_astronomers:rx:p217mm
[3] http://dspsr.sourceforge.net/
[4] http://psrchive.sourceforge.net/

same data. However, there is the possibility that the giant pulse is completely smeared out due to the deviation of the DM, then a single pulse search approach is required.

Heimdall

In order to account for the effect described above, I created another pipeline[5]to perform single pulse searches using Heimdall[6] (Walsh and Lynch, 2018). This pipeline is to address two possible causes of the DM variation. One is that the pulsar could be poorly timed and the DM value is not accurate enough. The other one is the ephemeris could be outdated as some of the gamma-ray pulsars are not routinely timed or due to the change of the interstellar environment. Heimdall is a transient detection package with GPU acceleration and has been used to carry out dispersed single pulse searches using a match box filter and an efficient de-dispersion technique. On completion of the search process, the pipeline reports the DM and the S/N of a candidate. This is different from DSPSR which highly depends on the accuracy of the DM and period of the pulsar, whereas Heimdall does not require prior information on periodicity and the DM is a free parameter. We make use of a feature in Heimdall where the search can be restricted to a range of DMs. The process therefore repeats for a series of different DM values within a given range. For each DM value trial, the de-dispersed data is searched using match box filters with widths ranging from 2^0 bin to 2^{12} bins where each bin corresponds to 8 μs. For each candidate, Heimdall records the corresponding S/N of the detection, the detection position in the filterbank file, the DM used in the search and the number of detection associated with the same event. With the detection position translated to a timestamp, each candidate can be located in the original baseband file. Then the candidates can be verified by checking the existence of a bright detection at the location using DSPSR which can output the candidates in the unit of pulsar period so that the phase of the bright detection can be obtained.

Pipeline

The baseband data were first transferred to the processing server, where they were converted to filterbank files using `digifil`, a program included in the DSPSR package. Every four baseband files were converted to a filterbank to decrease the number of pulses whose data lies between two baseband files. The outputted filterbank files were split into 128 channels, integrated every 2 samples, polarization scrunched and stored in 8bit format. Each channel is coherently de-dispersed to remove the delays within the channel. Only the delay between the channels remains. Heimdall performs the search on the filterbank files with a given range of DM values and widths of match-filter boxes.

An RFI mitigation process is carried out to reduce the number of false candidates. It first flags the channels that are known for being affected by a constant RFI origin and the part of the channels that are known for less sensitivity in the band pass. Then the process detects and inspects the bright channels of a candidate and labels them as RFI if the power of the candidate is concentrated in only a few channels and wider than a pre-defined threshold.

The candidate plots (see Figure 5.6 for an example) were visually inspected by eye and the one with high S/N went through a manual check using DSPSR. The whole pipeline is illustrated in Figure 5.5.

[5] https://github.com/wchenastro/gpsearch
[6] https://sourceforge.net/p/heimdall-astro/wiki/Home/

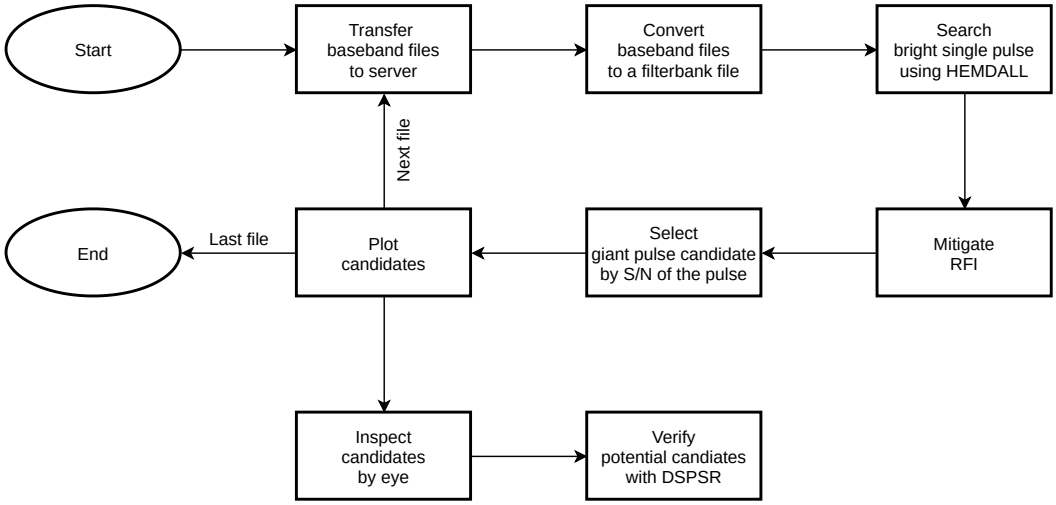

Figure 5.5: The single pulse search pipeline.

5.3 Result

5.3.1 Completeness test on the search using heimdall

Before working on the newly observed pulsars, we use the heimdall pipeline to search on the observational data of pulsars known to be giant pulse emitters, such as B1937+21. In the work of McKee et al. (2019), the observed emission rate of the giant pulse from this pulsar is 1.4×10^{-4} per rotation, which indicates there would be roughly 404 giant pulses emitted during the 1.5-hour observation. With the DM value optimized according to the brightest pulse, DSPSR picked up 408 giant pulses from the data of a 1.25-hour observation, which is consistent with the above prediction. To evaluate the completeness of the Heimdall search in the perspective of detection capability, we used Heimdall to search on the same data and got a number of 309 candidates. There are two possible reasons for the lesser number of candidates picked up by Heimdall: one is that Heimdall uses 4 times the number of channels as DSPSR for each chunk of data, which results in a lower time resolution; another one is that the early version of the pipeline converts two baseband data files into a single filterbank file which would lose a number of potential giant pulse between two filterbank files in the de-dispersion process.

5.3.2 Search result

During an average of 2.4-hours of observation on each pulsar, no pulse meeting the threshold of S/N was detected. The upper limits of the emission rate of the giant pulse for these pulsars are listed in Table 5.3.

In general, the sensitivity of the search depends on the RFI situation during the observation, various effects from the interstellar medium, the configuration and capability of the instruments, the intrinsic width and energy of the source and so on. It is also possible that the giant pulse emissions of these

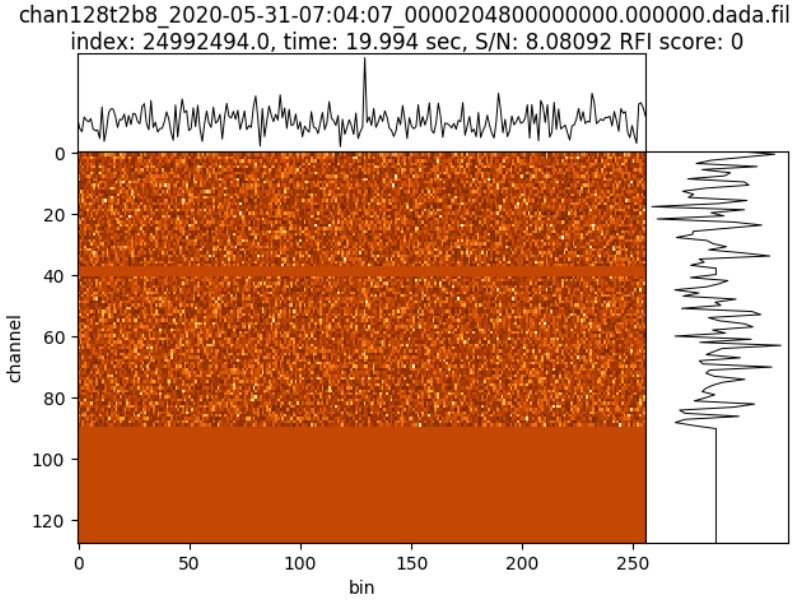

Figure 5.6: An example of Heimdall candidate, the lower channels were zapped to remove the RFI.

pulsars have a time-dependent occurrence rate. For example, Singal and Vats (2012) reported that the number of detected giant pulses from PSR B0950+08 vary significantly even in neighboring days. Non-regular emission rates are also observed in some of the repeating FRBs (Oppermann, Yu and Pen, 2018). Here we focus on the search sensitivity in the function of the assumed intrinsic widths of the giant pulse and the DM of the pulsar. The affected width W of a single pulse relates to the intrinsic width of the pulse, the error from the de-dispersion process and the effect of the ISM. It can be calculated as:

$$W = \sqrt{W_{\rm int}^2 + t_{\rm samp}^2 + \Delta t_{\rm DM}^2 + \tau_{\rm s}^2}, \tag{5.1}$$

Where $W_{\rm int}$ is the intrinsic width of the pulse, $t_{\rm samp}$ is the sampling interval of the receiver. $\Delta t_{\rm DM}^2$ is the time scale of dispersion effect inside a single channel, can be calculated as $\Delta t_{\rm DM} = 8.3 \cdot DM \frac{\Delta\nu}{\nu^3}\ \mu$s but because the data have been coherently de-dispersed while being converted to the filterbank files, so this term is considered zero assuming a correct DM value was used. The time scale of scattering $\tau_{\rm s}$ can be calculated using the fitted relation between $\tau_{\rm s}$ and DM from (Krishnakumar et al., 2015):

$$\tau_{sc}(\rm ms) = 3.6 \times 10^{-6} DM^{2.2}(1 + 1.94 \times 10^{-3} DM^{2.0}) \tag{5.2}$$

Note that 5.2 was obtained by fitting the observational data centered at a frequency of 327 MHz. To make it applicable for our observation centered at 1370MHz, the result needs to be scaled in frequency using the scaling law $\tau_{sc} \propto \nu^{-\alpha}$. We use $\alpha = 4.4$ as suggested in Krishnakumar et al. (2015). They also mentioned that there is a large spread in the fractional residual of the fit due to uncertainties. The

minimum detectable flux density of a single pulse S_{min} is:

$$S_{min} = \frac{T_{\rm sys}}{G\sqrt{n_{\rm p}\,\Delta\nu\,W}} \times S/N_{\rm min} \tag{5.3}$$

Where $T_{\rm sys}$ is the system temperature (K), G is the gain of the telescope (K/Jy), the result of $T_{\rm sys}/G$ can also be described as system equivalent flux density (SEFD). The $n_{\rm p}$ is the number of polarization, $\Delta\nu$ is the bandwidth of the receiver, W is the width of the pulse and $S/N_{\rm min}$ is the threshold of the detection. For the P217mm 7-Beam receiver centered at the frequency of 1.408 GHz of the Effelsberg telescope, the SEFD is 15 Jy, $\Delta\nu$ is 320 MHz and we use $S/N_{\rm min}$ of 7.5.
The minimum detectable flux for each pulsar has been listed in table 5.3

Table 5.3: Some of the derived properties of the observed pulsars. $\tau_{\rm s}$ is the scattering time scale derived from (Krishnakumar et al., 2015), $t_{\rm scin}$ and SBW are the scintillation time scale and bandwidth obtained from NE2001 model, $W_{\rm eff}$ is the effective width, $S_{\rm min}$ is the minimum detectable flux density, $R_{\rm up}$ is the derived upper limit of the giant pule emission rate from this work.

Pulsar name	$\tau_{\rm s}$ (μs)	$t_{\rm scin}$ (s)	SBW (MHz)	$W_{\rm eff}$ (μs)	$S_{\rm min}$ (Jy)	$R_{\rm up}$ (s^{-1})
J1816+4510	0.081	488.900	1.523	1.146	4.441	1.520×10^{-4}
J1833−1034*	29.880	18.750	0.002	29.902	0.869	1.210×10^{-4}
J1843−1113	0.427	140.300	0.179	1.220	4.304	1.980×10^{-4}
J1952+3252	0.140	203.600	0.203	1.151	4.430	0.926×10^{-4}
J2215+5135	0.754	0.400	261.800	1.370	4.062	0.926×10^{-4}
J2229+6114	66.000	0.007	58.750	66.010	0.585	1.110×10^{-4}
J1741+1351	0.016	1358.000	31.040	1.143	4.447	0.926×10^{-4}
J2339−0533	0.001	40.850	1090.000	1.143	4.447	1.130×10^{-4}

* The recorded baseband data of J1833−1034 was corrupted, the candidates picked up by the pipeline were not reliable.

5.4 Discussion

Here we discuss the possible reasons and implications why we did not find new giant pulse emitters.

Scintillation and scattering

Scattering is large for pulsars with high DM (Krishnakumar et al., 2015), which could affect the S/N of detection. The multiple propagation paths of the emission caused by scattering screens (see Equation 5.2) could broaden the width of pulses (Williamson, 1972; Cordes and Lazio, 2001), particularly at low frequencies. Giant pulses also have been observed to be affected (Lundgren et al., 1995; Bhat, Tingay and Knight, 2008). It is shown in Table 5.3 that most of the pulsars, except two, have a scattering time scale $\tau_{\rm s}$ shorter than the sampling time (0.8 microsecond), indicating that the ISM scattering may not have a strong broadening effect on these observations. However, as can be seen from the

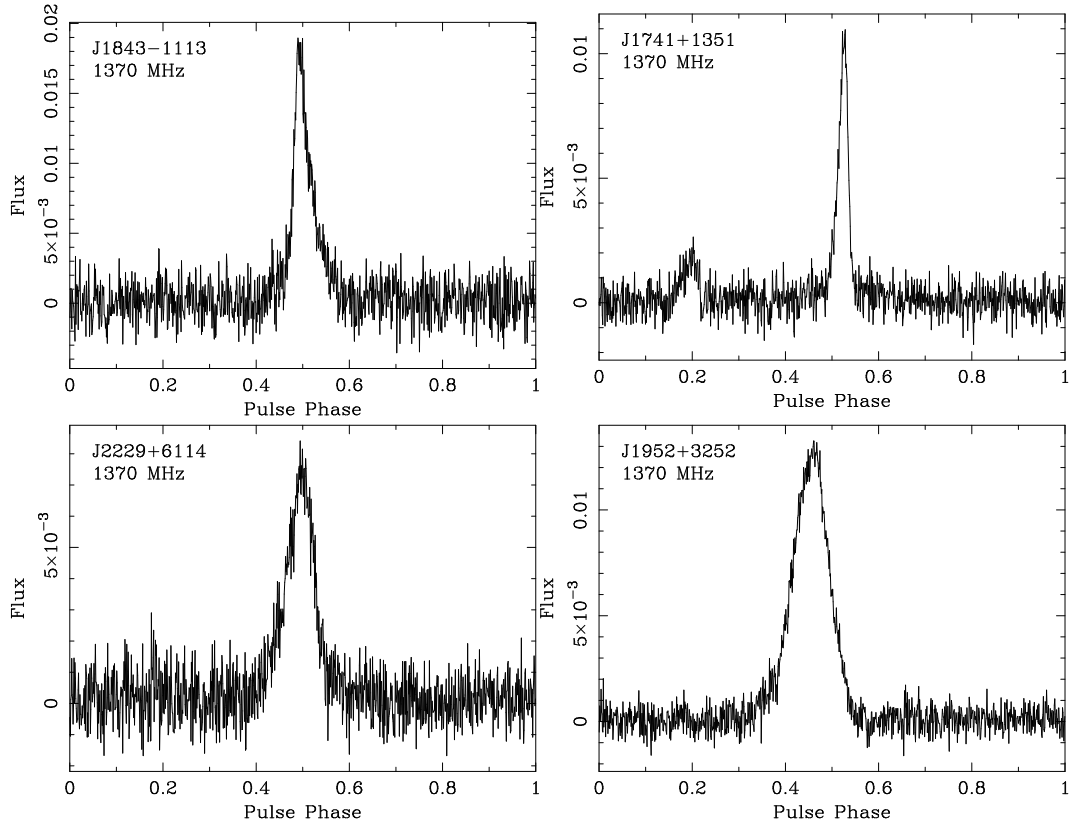

Figure 5.7: Profiles of pulsars obtained from our observations.

result of Krishnakumar et al. (2015), the large uncertainties of the relation between DM and scattering scale imply the actually scattering scale could deviate from the derived results up to two orders of magnitudes, thus the effect of scattering could not be completely ruled out.

The time scale t_{scin} and scintillation bandwidth (SBW) of scintillation could also affect the search for narrow pulses. I calculated them using the software package PYNE2001[7] which is an implementation of NE2001 Galactic free electron density model (Cordes and Lazio, 2002). The result for each pulsar is listed in Table 5.3. It can be seen that either the scintillation time scale or the bandwidth is less than the observational length and bandwidth, suggesting that the scale of scintillation does not have a significant effect on the pulsar signal. The average profiles of four observed pulsars in this thesis have been shown in Figure 5.7.

If the intrinsic width of the potential giant pulse is much narrower (such as the "nanoshots" from the Crab pulsar (e.g. Jessner, A. et al., 2010; Hankins, Eilek and Jones, 2016)) than the sampling time, it is still possible to detect the giant pulse. Because there are events where giant pulses with nanoseconds duration were detected in clusters that span for a couple of microseconds (Jessner, A. et al., 2010). So if other pulsars emit groups of nanoshots in similar timescale and brightness like those from the Crab pulsar, they would likely be detected by our observation.

[7] https://github.com/v-morello/pyne2001

Table 5.4: The scaled by distance flux density of Crab giant pulses and the expected detection.

	Scaled_Crab_flux (Jy)	Expected detection
J1816+4510	23.2	518
J1833-1034	39.1	662
J1843-1113	151.1	402
J1952+3252	42.4	863
J2215+5135	57.2	863
J2229+6114	17.3	719
J1741+1351	237.2	863
J2339-0533	779.3	719

Eclipsing

Two eclipse events happened during the observations of two pulsars. The first, PSR J2215+5135 is a "redback" system (Broderick et al., 2016) that consists of a millisecond pulsar and a low mass companion. The period of this system is 4.15 hours and the pulsar went through superior conjunction near the end of the first hour of the 3 hours observation. PSR J1816+4510 exists in a binary system with a metal-rich companion (Kaplan et al., 2013). The period of this system is 8.66 hours and the pulsar went through superior conjunction near the second part of the first hour of the 1.83 hours observation. From the orbital period of these two pulsars and the observation duration, the effects of the eclipse events might not be significant for PSR J2215+5135, but will reduce the amount of potential giant pulses for PSR J1816+4510.

Non-detection

The expected rate of giant pulse emission of these pulsars can be estimated if we assume they emit a similar population of giant pulses like the Crab pulsar. In the work of Karuppusamy, Stappers and van Straten (2010), the authors published a distribution of the giant pulse intensity as shown in Figure 5.8. According to the slope of the power-law distribution (-2.79±0.01 for the main pulse phase, -3.06±0.06 for the interpulse (defined in Introduction 1.2.1) phase), the total detections of giant pulses in the main pulse phase with flux density above 110 Jy is 1727 for their 6-hour observation. If the Crab pulsar was placed at the positions of the observed pulsars in this thesis, the aforementioned flux density is scaled in inverse-square-law with distances. I calculated these scaled flux densities and list them in Table 5.4. The expected detection above these scaled flux densities scaled by the observational time, are also listed. As can be seen from the table, all the scaled flux densities are larger than the S_{min} of the observations reported in this thesis, indicating that if these pulsars emit giant pulses like those from the main phase of Crab pulsar, the telescope should have detected them. The non-detection could indicate that these pulsars do not emit or emit less giant pulsars like the ones from Crab pulsars. The upper limit of the potential giant pulses emission rate for these observed pulsars, using Crab pulsar as the reference, is $1727 \div 6$ hour ≈ 0.08 s^{-1} for various flux density thresholds listed in the Table 5.4.

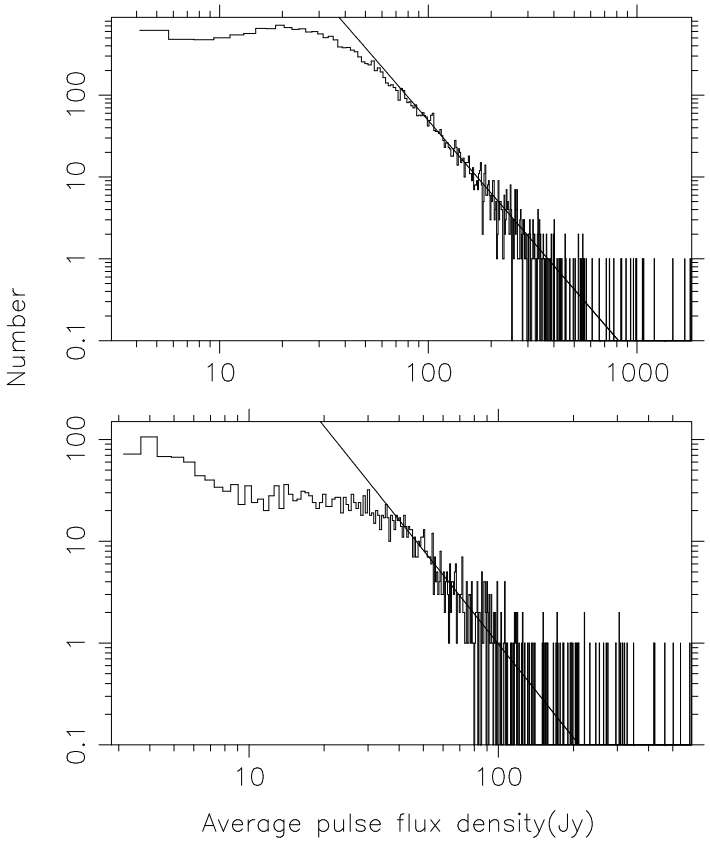

Figure 5.8: Distribution of the flux density of Crab giant pulses. Both axes are in a logarithmic scale. The top panel are the distribution in the Main phase with a slope of -2.79±0.01, and the bottom panel is the distribution in the interpulse with a slope of -3.06±0.06. (Karuppusamy, Stappers and van Straten, 2010)

5.5 Summary and Conclusion

In an attempt to search for giant pulses, we chose 8 pulsars with high magnetic fields at the light cylinder, high spin-down luminosities and high energy emission. Each pulsar was observed with Effelsberg telescope for 1 to 3 hours and the data was searched using a pipeline based on Heimdall. No giant pulse with significant S/N was detected. The search pipeline has been tested on the observational data of PSR B1937+21 and yielded the expected number of detection. We calculated the possible influences from the interstellar medium and showed that they are not significant to most of the pulsars we observed.

We believe the reason for the non-detection of the search is either that these pulsars do not emit individual pulse with a brightness higher than the minimum detectable flux density of our observation, or that high B_{LC}, high energy emission may not be a sufficient condition for giant pulse emission or the relationship between them is not as strong as expected.

Some of the pulsars searched for giant pulses in this project are also in the field of view of other telescopes. For example, J1833−1034, J1843−1113, J1952+3252, J1741+1351 and J2339−0533 are observable with MeerKAT. Searching with telescopes that have higher sensitivity increase the possibility of detection if the pulsar is a giant pulse emitter. The upcoming Ultra Broadband Receiver

(UBB) for the Effelsberg telescope would also provide a better detection capability for giant pulses than the current setup. That is because other than the upgrade on the sensitivity (see Equation 5.3), the wider bandwidth offers wider windows for pulsars with deep spectrum indices.

CHAPTER 6

Conclusion

6.1 Summary

I reviewed the development of radio astronomy from an instrumental perspective. The recent fast transient discoveries have indicated that one of the big challenges of current radio observations is to make efficient fast transient surveys with accurate localizations. This is the primary driver for a new kind of observation mode: multi-beam observation with interferometers, which I have detailed in this thesis. A general electronic beamforming technique is explained and the corresponding challenges and observational strategies are proposed to enable optimized multi-beam observations. I developed a software package called "Mosaic" to enable the adoption of the above-mentioned techniques for interferometric arrays. It provides an interferometric pattern simulator and a characterizer, an optimized tiling generator and a beamforming weights calculator. As an attestation of my work, these implementations are put into application for MeerKAT, a state of the art interferometric array. The integration of my development in MeerKAT's beamforming platform is described and illustrated. The transient search capability of such platform is simulated. With the Mosaic package deployed in the MPIfR beamformer, the verification of the implementation and the performance of the multi-beam localization is also provided. MeerKAT has been carrying out multiple fast transient surveys and targeted searches since 2020. At the time of writing, a total of 66 pulsars have been discovered, with many of them being millisecond pulsars and with arcsecond localization. These discoveries have proven the viability of the mentioned techniques and my developments, showing the capacity for larger scale applications.

The phenomenon of giant pulses from pulsars has baffled scientists for a long time. In the meantime, a number of giant pulse emitters shared some similar properties, such as high energy emission and a high magnetic field near the light cylinder. I tried to investigate the relationship between the giant pulse emission and these properties by selecting pulsars with high energy emission and a high magnetic field near the light cylinder as observation candidates. I developed a single pulse search pipeline based on Heimdall. The pipeline has been tested against the data of the known giant pulse emitters to insure its search completeness. After observation and data reduction, no giant pulse from these pulsars has been detected by the pipeline and the corresponding rate limits were calculated. The effects of the interstellar medium and the stellar eclipses have been put into consideration, though they should not pose as great obstacles to these pulsars if there are indeed giant pulse emissions. Thus, I concluded that during our observations, these pulsars did not emit bright giant pulses that are detectable by the

observing telescope. We discovered that the condition of high magnetic field at the light cylinder and high energy emission may not be sufficient for the occurrence of giant pulses.

6.2 Outlook

The fast radio transient sky has been showing its abundances since a growing number of wide-field interferometers have been put into service. The campaign of fast transient surveys will reach its first climax with the participation of the upcoming SKA. It is a multinational effort in pooling resources to construct the largest telescope ever constructed in human history. The mid-frequency (350 MHz ~ 1.54GHz) component of this project is called "SKA-mid" which in phase 1 consists of about 200 dishes with a diameter of 15 meters and an offset Gregorian mount. It can be assumed that these dishes could generate a similar response to the current MeerKAT dishes. In fact, as a precursor of SKA, the entire MeerKAT array will operate as the core of the SKA-mid. Given these similarities, the current beamforming solution for MeerKAT should be applicable to SKA-mid. The Mosaic package itself does not assume a particular configuration of the array and most inputs are parameterized so that it should be portable for a larger infrastructure. However, one of the challenges of SKA-mid is the calibration of the large sky area in real time, as the maximum baseline of SKA-mid is 18-times longer than MeerKAT. From a computing perspective, how the significant increase of the data rate could affect the efficiency of the current solution should also be put into consideration.

The giant pulses search does not find any giant pulse could be due to that the giant pulse emission of these pulsars is not bright enough or clustered which has been observed in some emitters. Therefore a natural extension of this work is to observe these pulsars or similar candidates with telescopes of higher sensitivity and spend longer observational time on an individual pulsar. Also, having a larger sample, the suggested correlation with B_{LC} could be proven wrong.

6.3 Improvement

Though the beamforming techniques developed in this thesis have been put to test and verified by the real science surveys, they are the first step toward a larger scale application. The goal of the MPIfR beamformer is to form thousands of beams.

Whether the current implementation of the beamforming routine can still produce a tiling and calculate the beamforming weights in a relatively short instant when the number of the beam is massively increased remains to be evaluated. On the other hand, the current implementation prioritizes functionality rather than efficiency which means there is still room to improve when a bottleneck is reached.

The different performance between raw-voltage beamforming and visibility beamforming is presented in the thesis and the raw-voltage method is considered to be better for high time resolution science for a large number of receiving elements. While the visibility method still has its big advantage in the field of view when the requirement for the time resolution is not so strict. Furthermore, the visibility method could take advantage of numerous hardware-accelerated FFT algorithms. The MPIfR's S-band system also includes a correlator, hence the usage of visibility beamforming or the combination of two methods could be explored in the future.

The beamformed observation of 47 Tucanae is part of the globular cluster surveys of the TRAPUM project. The data were used to test the performance of the mentioned implementation in the thesis,

only the known pulsars in this cluster were folded and inspected. The search for new sources was not performed yet. Furthermore, this cluster was observed in both L-band and UHF-band which could provide a wide emission spectrum of the potential sources. For this reason, a search for new sources in this cluster will be a top priority for future work.

The localization of the pulsar with multiple overlapping beams is a demonstration of the capability of the mentioned beamforming techniques. While the result is largely good, it is an oversimplified approach. The instrumental error, the scale of the interstellar medium engagement and turbulence, the error estimation of the localization routine, the frequency-dependent PSF variation, the spectrum of the pulsar and so on should be put into account in future enhancement of the work presented here.

Bibliography

Abdo, A. A. et al. (2010), *The First Fermi Large Area Telescope Catalog of Gamma-ray Pulsars*, ApJS **187** 460, arXiv: 0910.1608 [astro-ph.HE] (cit. on p. 73).

Abdollahi, S. et al. (2020), *Fermi Large Area Telescope Fourth Source Catalog*, ApJS **247**, 33 33, arXiv: 1902.10045 [astro-ph.HE] (cit. on p. 58).

Abramovici, A. et al. (1992), *LIGO: The Laser Interferometer Gravitational-Wave Observatory*, Science **256** 325 (cit. on p. 9).

ALMA Partnership et al. (2015), *The 2014 ALMA Long Baseline Campaign: First Results from High Angular Resolution Observations toward the HL Tau Region*, ApJ **808**, L3 L3, arXiv: 1503.02649 [astro-ph.SR] (cit. on p. 19).

Andreoni, I. and J. Cooke (2019), "The Deeper Wider Faster Programme: Chasing the Fastest Bursts in the Universe", *Southern Horizons in Time-Domain Astronomy*, ed. by R. E. Griffin, vol. 339 135, arXiv: 1802.01100 [astro-ph.IM] (cit. on p. 63).

Antoniadis, J. et al. (2013a), *A Massive Pulsar in a Compact Relativistic Binary*, Science **340**, ISSN: 0036-8075, eprint: https://science.sciencemag.org/content/340/6131/1233232.full.pdf, URL: https://science.sciencemag.org/content/340/6131/1233232 (cit. on p. 11).

Antoniadis, J. et al. (2013b), *A Massive Pulsar in a Compact Relativistic Binary*, Science **340** 448, arXiv: 1304.6875 [astro-ph.HE] (cit. on p. 34).

Archibald, A. M. et al. (2018), *Universality of free fall from the orbital motion of a pulsar in a stellar triple system*, Nature **559** 73, arXiv: 1807.02059 [astro-ph.HE] (cit. on p. 10).

Argyle, E. and J. F. R. Gower (1972), *The Pulse-Height Distribution for NP 0532*, ApJ **175** L89 (cit. on pp. 68, 69).

Arons, J. and E. T. Scharlemann (1979), *Pair formation above pulsar polar caps: structure of the low altitude acceleration zone.*, ApJ **231** 854 (cit. on p. 13).

Asseo, E., R. Pellat and M. Rosado (1980), *Pulsar radio emission from beam plasma instability*, ApJ **239** 661 (cit. on p. 12).

Backer, D. C. (1970a), *Correlation of Subpulse Structure in a Sequence of Pulses from Pulsar PSR 1919+21*, Nature **227** 692 (cit. on p. 68).

– (1970b), *Peculiar Pulse Burst in PSR 1237 + 25*, Nature **228** 1297 (cit. on p. 68).

– (1970c), *Pulsar Nulling Phenomena*, Nature **228** 42 (cit. on p. 68).

Bailes, M. et al. (2020), *The MeerKAT telescope as a pulsar facility: System verification and early science results from MeerTime*, PASA **37**, e028 e028, arXiv: 2005.14366 [astro-ph.IM] (cit. on pp. 9, 28).

Bailes, M. et al. (2021), *Multi-frequency observations of SGR J1935+2154*, MNRAS, arXiv: 2103.06052 [astro-ph.HE] (cit. on p. 64).

Bannister, K. W. et al. (2019), *A single fast radio burst localized to a massive galaxy at cosmological distance*, Science **365** 565, arXiv: 1906.11476 [astro-ph.HE] (cit. on p. 18).

Bansal, K. et al. (2019), *Scattering Study of Pulsars below 100 MHz Using LWA1*, ApJ **875**, 146 146, arXiv: 1903.03457 [astro-ph.HE] (cit. on p. 60).

Barr, E. D. (2018), "An S-band Receiver and Backend System for MeerKAT", *Pulsar Astrophysics the Next Fifty Years*, ed. by P. Weltevrede et al., vol. 337 175 (cit. on pp. 31, 34, 42).

Basu, A. et al. (2019), *CMB foreground measurements through broad-band radio spectro-polarimetry: prospects of the SKA-MPG telescope*, Monthly Notices of the Royal Astronomical Society **488** 1618, ISSN: 0035-8711, eprint: https://academic.oup.com/mnras/article-pdf/488/2/1618/28944049/stz1637.pdf, URL: https://doi.org/10.1093/mnras/stz1637 (cit. on p. 1).

Bhandari, S. et al. (2018), *The SUrvey for Pulsars and Extragalactic Radio Bursts - II. New FRB discoveries and their follow-up*, MNRAS **475** 1427, arXiv: 1711.08110 [astro-ph.HE] (cit. on p. 24).

Bhandari, S. et al. (2020), *The Host Galaxies and Progenitors of Fast Radio Bursts Localized with the Australian Square Kilometre Array Pathfinder*, ApJ **895**, L37 L37, arXiv: 2005.13160 [astro-ph.GA] (cit. on p. 24).

Bhat, N. D. R., S. J. Tingay and H. S. Knight (2008), *Bright Giant Pulses from the Crab Nebula Pulsar: Statistical Properties, Pulse Broadening, and Scattering Due to the Nebula*, The Astrophysical Journal **676** 1200, URL: https://doi.org/10.1086%2F528735 (cit. on p. 79).

Bhattacharya, D. and E. P. J. van den Heuvel (1991), *Formation and evolution of binary and millisecond radio pulsars*, Phys. Rep. **203** 1 (cit. on p. 9).

Boccardi, B. et al. (2017), *Radio observations of active galactic nuclei with mm-VLBI*, A&A Rev. **25**, 4 4, arXiv: 1711.07548 [astro-ph.HE] (cit. on p. 19).

Bochenek, C. D. et al. (2020), *A fast radio burst associated with a Galactic magnetar*, Nature **587** 59, arXiv: 2005.10828 [astro-ph.HE] (cit. on pp. 16, 64).

Broderick, J. W. et al. (2016), *Low-radio-frequency eclipses of the redback pulsar J2215+5135 observed in the image plane with LOFAR*, Monthly Notices of the Royal Astronomical Society **459** 2681, ISSN: 0035-8711, eprint: https://academic.oup.com/mnras/article-pdf/459/3/2681/8107078/stw794.pdf, URL: https://doi.org/10.1093/mnras/stw794 (cit. on p. 81).

Caleb, M. et al. (2020), *Simultaneous multi-telescope observations of FRB 121102*, Monthly Notices of the Royal Astronomical Society **496** 4565, ISSN: 0035-8711, eprint: https://academic.oup.com/mnras/article-pdf/496/4/4565/33503296/staa1791.pdf, URL: https://doi.org/10.1093/mnras/staa1791 (cit. on pp. 53, 62, 63).

Cameron, A. D. et al. (2020), *The High Time Resolution Universe Pulsar Survey - XVI. Discovery and timing of 40 pulsars from the southern Galactic plane*, MNRAS **493** 1063, arXiv: 2001.01823 [astro-ph.HE] (cit. on p. 60).

Camilo, F. (2018), *African star joins the radio astronomy firmament*, Nature Astronomy **2** 594 (cit. on p. 34).

Chatterjee, S. et al. (2017), *A direct localization of a fast radio burst and its host*, Nature **541** 58, arXiv: 1701.01098 [astro-ph.HE] (cit. on p. 19).

Chen, A. Y. and A. M. Beloborodov (2014), *ELECTRODYNAMICS OF AXISYMMETRIC PULSAR MAGNETOSPHERE WITH ELECTRON-POSITRON DISCHARGE: A NUMERICAL EXPERIMENT*, The Astrophysical Journal **795** L22, URL: https://doi.org/10.1088/2041-8205/795/1/l22 (cit. on p. 13).

Cheng, K. S., C. Ho and M. Ruderman (1986), *Energetic Radiation from Rapidly Spinning Pulsars. I. Outer Magnetosphere Gaps*, ApJ **300** 500 (cit. on p. 13).

CHIME/FRB Collaboration et al. (2018), *The CHIME Fast Radio Burst Project: System Overview*, ApJ **863**, 48 48, arXiv: 1803.11235 [astro-ph.IM] (cit. on p. 24).
CHIME/FRB Collaboration et al. (2020), *A bright millisecond-duration radio burst from a Galactic magnetar*, Nature **587** 54, arXiv: 2005.10324 [astro-ph.HE] (cit. on pp. 12, 16, 64, 72).
Clark, C. J. et al. (2021), *Einstein@Home discovery of the gamma-ray millisecond pulsar PSR J2039-5617 confirms its predicted redback nature*, MNRAS **502** 915, arXiv: 2007.14849 [astro-ph.HE] (cit. on p. 58).
Cognard, I. et al. (1996), *Giant Radio Pulses from a Millisecond Pulsar*, ApJ **457** L81 (cit. on p. 15).
Contopoulos, I. (2019), *Current closure in the pulsar magnetosphere*, MNRAS **482** L50, arXiv: 1809.09064 [astro-ph.HE] (cit. on p. 15).
Contopoulos, I., D. Kazanas and C. Fendt (1999), *The Axisymmetric Pulsar Magnetosphere*, The Astrophysical Journal **511** 351, URL: https://doi.org/10.1086/306652 (cit. on p. 13).
Cordes, J. M. (2009), *Survey Metrics*, SKA Memo **109**, URL: https://www.skatelescope.org/uploaded/26865_109_Memo_Cordes.pdf (cit. on pp. 25, 44).
Cordes, J. M. and T. J. W. Lazio (2002), *NE2001.I. A New Model for the Galactic Distribution of Free Electrons and its Fluctuations*, arXiv e-prints, astro-ph/0207156 astro, arXiv: astro-ph/0207156 [astro-ph] (cit. on pp. 15, 16, 60, 80).
Cordes, J. M. and T. J. W. Lazio (2001), *Anomalous Radio-Wave Scattering from Interstellar Plasma Structures*, The Astrophysical Journal **549** 997, URL: https://doi.org/10.1086%2F319442 (cit. on p. 79).
Cordes, J. M. and M. A. McLaughlin (2003), *Searches for Fast Radio Transients*, The Astrophysical Journal **596** 1142, URL: https://doi.org/10.1086/378231 (cit. on p. 7).
Cordes, J. M., R. M. Shannon and D. R. Stinebring (2016), *FREQUENCY-DEPENDENT DISPERSION MEASURES AND IMPLICATIONS FOR PULSAR TIMING*, The Astrophysical Journal **817** 16, URL: https://doi.org/10.3847/0004-637x/817/1/16 (cit. on p. 75).
Cordes, J. M. et al. (2006), *Arecibo Pulsar Survey Using ALFA. I. Survey Strategy and First Discoveries*, The Astrophysical Journal **637** 446, URL: https://doi.org/10.1086/498335 (cit. on p. 34).
Cusumano, G. et al. (2003), *The phase of the radio and X-ray pulses of PSR B1937+21*, A&A **410** L9, eprint: astro-ph/0309580 (cit. on p. 68).
Daugherty, J. K. and A. K. Harding (1982), *Electromagnetic cascades in pulsars.*, ApJ **252** 337 (cit. on p. 12).
Davies, J. G., B. Anderson and I. Morison (1980), *The Jodrell Bank radio-linked interferometer network*, Nature **288** 64 (cit. on p. 18).
Demorest, P. B. et al. (2010), *A two-solar-mass neutron star measured using Shapiro delay*, Nature **467** 1081, arXiv: 1010.5788 [astro-ph.HE] (cit. on p. 34).
Deshpande, A. A. and J. M. Rankin (1999), *Pulsar Magnetospheric Emission Mapping: Images and Implications of Polar Cap Weather*, The Astrophysical Journal **524** 1008, URL: https://doi.org/10.1086/307862 (cit. on p. 9).
Desvignes, G. et al. (2016), *High-precision timing of 42 millisecond pulsars with the European Pulsar Timing Array*, MNRAS **458** 3341, arXiv: 1602.08511 [astro-ph.HE] (cit. on p. 75).
Deutsch, A. J. (1955), *Radio Emission from Astronomical Bodies*, Leaflet of the Astronomical Society of the Pacific **7** 137 (cit. on p. 12).
Eilek, J. A. and T. H. Hankins (2016), *Radio emission physics in the Crab pulsar*, Journal of Plasma Physics **82**, 635820302 635820302, arXiv: 1604.02472 [astro-ph.HE] (cit. on p. 70).

Enoto, T. et al. (2021), *Enhanced x-ray emission coinciding with giant radio pulses from the Crab Pulsar*, Science **372** 187, arXiv: 2104.03492 [astro-ph.HE] (cit. on p. 68).

Ershov, A. A. and A. D. Kuzmin (2003), *Detection of Giant Pulses from the Pulsar PSR B1112+50*, Astronomy Letters **29** 91, arXiv: astro-ph/0212529 [astro-ph] (cit. on p. 72).

Event Horizon Telescope Collaboration et al. (2019), *First M87 Event Horizon Telescope Results. I. The Shadow of the Supermassive Black Hole*, ApJ **875**, L1 L1, arXiv: 1906.11238 [astro-ph.GA] (cit. on p. 18).

Falcke, Heino and Rezzolla, Luciano (2014), *Fast radio bursts: the last sign of supramassive neutronhttps://www.overleaf.com/project/5e42753b2ef81c00013cd320 stars*, A&A **562** A137, URL: https://doi.org/10.1051/0004-6361/201321996 (cit. on p. 16).

Fish, V. L., M. Shea and K. Akiyama (2020), *Imaging black holes and jets with a VLBI array including multiple space-based telescopes*, Advances in Space Research **65** 821, arXiv: 1903.09539 [astro-ph.IM] (cit. on p. 19).

Fitzgibbon, A., M. Pilu and R. B. Fisher (1999), *Direct least square fitting of ellipses*, IEEE Transactions on Pattern Analysis and Machine Intelligence **21** 476 (cit. on p. 37).

Foster, R. S. and D. C. Backer (1990), *Constructing a Pulsar Timing Array*, ApJ **361** 300 (cit. on p. 9).

Freire, P. C. (2000), *The Pulsars in 47 Tucanae*, PhD thesis: - (cit. on p. 47).

Freire, P. C. C. (2013), "The pulsar population in Globular Clusters and in the Galaxy", *Neutron Stars and Pulsars: Challenges and Opportunities after 80 years*, ed. by J. van Leeuwen, vol. 291 243, arXiv: 1210.3984 [astro-ph.GA] (cit. on p. 10).

Frost, O. L. (1972), *An algorithm for linearly constrained adaptive array processing*, Proceedings of the IEEE **60** 926 (cit. on p. 35).

Gaensler, B. M. (2014), *GRB 140705A / SGR 1935+2154: Probable association with supernova remnant G57.2+0.8.*, GRB Coordinates Network **16533** 1 (cit. on p. 64).

Gil, J., Y. Lyubarsky and G. I. Melikidze (2004), *Curvature Radiation in Pulsar Magnetospheric Plasma*, ApJ **600** 872, arXiv: astro-ph/0310621 [astro-ph] (cit. on p. 12).

Ginsburg, I. et al. (2016), *Detecting stars at the galactic centre via synchrotron emission*, MNRAS **455** L21, arXiv: 1509.06251 [astro-ph.GA] (cit. on p. 2).

Goldreich, P. and W. H. Julian (1969), *Pulsar Electrodynamics*, ApJ **157** 869 (cit. on pp. 12, 13).

Gu, W.-M. et al. (2016), *A Neutron Star-White Dwarf Binary Model for Repeating Fast Radio Burst 121102*, ApJ **823**, L28 L28, arXiv: 1604.05336 [astro-ph.HE] (cit. on p. 16).

Haberl, F. and R. Sturm (2016), *High-mass X-ray binaries in the Small Magellanic Cloud*, A&A **586**, A81 A81, arXiv: 1511.00445 [astro-ph.GA] (cit. on p. 59).

Han, J. L. et al. (2021), *The FAST Galactic Plane Pulsar Snapshot survey: I. Project design and pulsar discoveries*, Research in Astronomy and Astrophysics **21** 107, URL: https://doi.org/10.1088/1674-4527/21/5/107 (cit. on p. 34).

Hankins, T. H. (1971), *Microsecond Intensity Variations in the Radio Emissions from CP 0950*, ApJ **169** 487 (cit. on p. 24).

Hankins, T. H., J. A. Eilek and G. Jones (2016), *The Crab Pulsar at Centimeter Wavelengths. II. Single Pulses*, ApJ **833**, 47 47, arXiv: 1608.08881 [astro-ph.HE] (cit. on p. 80).

Hankins, T. H. et al. (2003), *Nanosecond radio bursts from strong plasma turbulence in the Crab pulsar*, Nature **422** 141 (cit. on pp. 14, 24).

Harding, A. K. et al. (2008), *High-Altitude Emission from Pulsar Slot Gaps: The Crab Pulsar*, ApJ **680** 1378, arXiv: 0803.0699 [astro-ph] (cit. on p. 13).

Heintz, K. E. et al. (2020), *Host Galaxy Properties and Offset Distributions of Fast Radio Bursts: Implications for Their Progenitors*, ApJ **903**, 152 152, arXiv: 2009.10747 [astro-ph.GA] (cit. on p. 16).
Hesse, K. H. and R. Wielebinski (1974), *Pulse Intensity Histograms of Pulsars*, A&A **31** 409 (cit. on pp. 68, 69).
Hezaveh, Y. D. et al. (2016), *Detection of Lensing Substructure Using ALMA Observations of the Dusty Galaxy SDP.81*, ApJ **823**, 37 37, arXiv: 1601.01388 [astro-ph.CO] (cit. on p. 19).
Högbom, J. A. (1974), *Aperture Synthesis with a Non-Regular Distribution of Interferometer Baselines*, A&AS **15** 417 (cit. on p. 18).
Holwerda, B. W., S. .-.-L. Blyth and A. J. Baker (2012), "Looking at the distant universe with the MeerKAT Array (LADUMA)", *The Spectral Energy Distribution of Galaxies - SED 2011*, ed. by R. J. Tuffs and C. C. Popescu, vol. 284 496, arXiv: 1109.5605 [astro-ph.CO] (cit. on p. 28).
Israel, G. L. et al. (2016), *The discovery, monitoring and environment of SGR J1935+2154*, Monthly Notices of the Royal Astronomical Society **457** 3448, ISSN: 0035-8711, eprint: https://academic.oup.com/mnras/article-pdf/457/4/3448/18510260/stw008.pdf, URL: https://doi.org/10.1093/mnras/stw008 (cit. on p. 64).
Istomin, Y. N. (2004), "Origin of Giant Radio Pulses", *Young Neutron Stars and Their Environments*, ed. by F. Camilo and B. M. Gaensler, vol. 218 369 (cit. on p. 70).
Jansky, K. G. (1933a), *Electrical Disturbances Apparently of Extraterrestrial Origin*, Proceedings of the Institute of Radio Engineers **21** 1387 (cit. on p. 1).
Jansky, K. G. (1933b), *Electrical phenomena that apparently are of interstellar origin*, Popular Astronomy **41** 548 (cit. on p. 3).
– (1933c), *Radio Waves from Outside the Solar System*, Nature **132** 66 (cit. on p. 3).
Jarvis, M. et al. (2016), "The MeerKAT International GHz Tiered Extragalactic Exploration (MIGHTEE) Survey", *MeerKAT Science: On the Pathway to the SKA* 6, arXiv: 1709.01901 [astro-ph.GA] (cit. on p. 28).
Jenet, F. et al. (2009), *The North American Nanohertz Observatory for Gravitational Waves*, arXiv e-prints, arXiv:0909.1058 arXiv:0909.1058, arXiv: 0909.1058 [astro-ph.IM] (cit. on p. 9).
Jessner, A. et al. (2010), *Giant pulses with nanosecond time resolution detected from the Crab pulsar at 8.5 and 15.1 GHz*, A&A **524** A60, URL: https://doi.org/10.1051/0004-6361/201014806 (cit. on p. 80).
Johnston, S. and R. W. Romani (2002), *A search for giant pulses in Vela-like pulsars*, MNRAS **332** 109, eprint: astro-ph/0201378 (cit. on p. 72).
Johnston, S. and R. W. Romani (2003), *Giant Pulses from PSR B0540-69 in the Large Magellanic Cloud*, The Astrophysical Journal **590** L95, URL: https://doi.org/10.1086/376826 (cit. on p. 70).
Jonas, J. and MeerKAT Team (2016), "The MeerKAT Radio Telescope", *MeerKAT Science: On the Pathway to the SKA* 1 (cit. on p. 42).
Joshi, B. C. et al. (2004), "Giant Pulses in Millisecond Pulsars", *Young Neutron Stars and Their Environments*, ed. by F. Camilo and B. M. Gaensler, vol. 218 319, arXiv: astro-ph/0310285 [astro-ph] (cit. on p. 72).
Kaplan, D. L. et al. (2013), *A Metal-rich Low-gravity Companion to a Massive Millisecond Pulsar*, ApJ **765**, 158 158, arXiv: 1302.2492 [astro-ph.SR] (cit. on p. 81).
Karuppusamy, R., B. W. Stappers and M. Serylak (2011), *A low frequency study of PSRs B1133+16, B1112+50, and B0031-07*, A&A **525**, A55 A55, arXiv: 1010.5877 [astro-ph.GA] (cit. on p. 72).

Karuppusamy, R., B. W. Stappers and W. van Straten (2010), *Giant pulses from the Crab pulsar. A wide-band study*, A&A **515**, A36 A36, arXiv: 1004.2803 (cit. on pp. 81, 82).

Kinkhabwala, A. and S. E. Thorsett (2000), *Multifrequency Observations of Giant Radio Pulses from the Millisecond Pulsar B1937+21*, ApJ **535** 365, eprint: astro-ph/9910134 (cit. on p. 14).

Knight, H. S. et al. (2005), *A Search for Giant Pulses from Millisecond Pulsars*, ApJ **625** 951, eprint: astro-ph/0502203 (cit. on p. 72).

Knight, H. S. et al. (2006a), *Green Bank Telescope Studies of Giant Pulses from Millisecond Pulsars*, The Astrophysical Journal **640** 941, URL: https://doi.org/10.1086/500292 (cit. on p. 68).

– (2006b), *Green Bank Telescope Studies of Giant Pulses from Millisecond Pulsars*, ApJ **640** 941, eprint: astro-ph/0512341 (cit. on p. 72).

Kozlova, A. V. et al. (2016), *The first observation of an intermediate flare from SGR 1935+2154*, Monthly Notices of the Royal Astronomical Society **460** 2008, ISSN: 0035-8711, eprint: https://academic.oup.com/mnras/article-pdf/460/2/2008/8117029/stw1109.pdf, URL: https://doi.org/10.1093/mnras/stw1109 (cit. on p. 64).

Kramer, M., S. Johnston and W. van Straten (2002), *High-resolution single-pulse studies of the Vela pulsar*, MNRAS **334** 523, arXiv: astro-ph/0203126 [astro-ph] (cit. on p. 72).

Kramer, M. et al. (2007), *Polarized radio emission from a magnetar*, Monthly Notices of the Royal Astronomical Society **377** 107, ISSN: 0035-8711, eprint: https://academic.oup.com/mnras/article-pdf/377/1/107/5766018/mnras0377-0107.pdf, URL: https://doi.org/10.1111/j.1365-2966.2007.11622.x (cit. on p. 11).

Kramer, M. et al. (2016), "The MeerKAT Max-Planck S-band System", *MeerKAT Science: On the Pathway to the SKA* 3 (cit. on pp. 30, 42, 52).

Kramer, M. (2004), "Millisecond Pulsarsas Tools of Fundamental Physics", *Astrophysics, Clocks and Fundamental Constants*, ed. by S. G. Karshenboim and E. Peik, vol. 648 33 (cit. on pp. 11, 34, 60).

Kramer, M. and D. J. Champion (2013), *The European Pulsar Timing Array and the Large European Array for Pulsars*, Classical and Quantum Gravity **30**, 224009 224009 (cit. on p. 9).

Krishnakumar, M. A. et al. (2015), *SCATTER BROADENING MEASUREMENTS OF 124 PULSARS AT 327 MHZ*, The Astrophysical Journal **804** 23, URL: https://doi.org/10.1088%2F0004-637x%2F804%2F1%2F23 (cit. on pp. 78–80).

Kuzmin, A. D. and A. A. Ershov (2004), *Giant pulses in pulsar <ASTROBJ>PSR B0031-07</ASTROBJ>*, A&A **427** 575, arXiv: astro-ph/0408008 [astro-ph] (cit. on p. 72).

Lasker, B. M. (1994), "Digitization and Distribution of the Large Photographic Surveys", *American Astronomical Society Meeting Abstracts #184*, vol. 184, American Astronomical Society Meeting Abstracts 35.01 (cit. on p. 48).

Lazio, T. J. W. and J. M. Cordes (1998), *Hyperstrong Radio-Wave Scattering in the Galactic Center. II. A Likelihood Analysis of Free Electrons in the Galactic Center*, ApJ **505** 715, arXiv: astro-ph/9804157 [astro-ph] (cit. on p. 60).

Lee, K. J. (2016), "Prospects of Gravitational Wave Detection Using Pulsar Timing Array for Chinese Future Telescopes", *Frontiers in Radio Astronomy and FAST Early Sciences Symposium 2015*, ed. by L. Qain and D. Li, vol. 502, Astronomical Society of the Pacific Conference Series 19 (cit. on p. 9).

Liebling, S. L. and C. Palenzuela (2016), *Electromagnetic luminosity of the coalescence of charged black hole binaries*, Phys. Rev. D **94**, 064046 064046, arXiv: 1607.02140 [gr-qc] (cit. on p. 16).

Lien, A. Y. et al. (2014), *GRB 140705A: Swift-BAT refined analysis of a possible newly discovered SGR 1935+2154.*, GRB Coordinates Network **16522** 1 (cit. on p. 64).

Lorimer, D. R. and M. Kramer (2004), *Handbook of Pulsar Astronomy*, vol. 4 (cit. on p. 62).
Lorimer, D. R. et al. (2007), *A Bright Millisecond Radio Burst of Extragalactic Origin*, Science **318** 777, arXiv: 0709.4301 (cit. on pp. 16, 24, 34).
Lorimer, D. R. (2008), *Binary and Millisecond Pulsars*, Living Reviews in Relativity **11** 8, ISSN: 1433-8351, URL: https://doi.org/10.12942/lrr-2008-8 (cit. on p. 10).
Lundgren, S. C. et al. (1995), *Giant Pulses from the Crab Pulsar: A Joint Radio and Gamma-Ray Study*, ApJ **453** 433 (cit. on pp. 68, 79).
Luo, Q. and D. B. Melrose (1995), *Curvature maser emission due to field line torsion in pulsar magnetospheres*, MNRAS **276** 372 (cit. on p. 12).
Lyne, A. and F. Graham-Smith (2012), *Pulsar Astronomy*, 4th ed., Cambridge Astrophysics, Cambridge University Press (cit. on p. 8).
Lyubarsky, Y. (2018), *Radio emission of the Crab and Crab-like pulsars*, Monthly Notices of the Royal Astronomical Society **483** 1731, ISSN: 0035-8711, eprint: https://academic.oup.com/mnras/article-pdf/483/2/1731/27098977/sty3233.pdf, URL: https://doi.org/10.1093/mnras/sty3233 (cit. on pp. 14, 68, 70).
Lyutikov, M. (2007), *On generation of Crab giant pulses*, MNRAS **381** 1190, arXiv: 0705.2530 [astro-ph] (cit. on pp. 70, 71).
Lyutikov, M., R. D. Blandford and G. Machabeli (1999), *On the nature of pulsar radio emission*, Monthly Notices of the Royal Astronomical Society **305** 338, ISSN: 0035-8711, eprint: https://academic.oup.com/mnras/article-pdf/305/2/338/18630642/305-2-338.pdf, URL: https://doi.org/10.1046/j.1365-8711.1999.02443.x (cit. on p. 12).
Lyutikov, M., L. Burzawa and S. B. Popov (2016), *Fast radio bursts as giant pulses from young rapidly rotating pulsars*, Monthly Notices of the Royal Astronomical Society **462** 941, ISSN: 0035-8711, eprint: https://academic.oup.com/mnras/article-pdf/462/1/941/18471469/stw1669.pdf, URL: https://doi.org/10.1093/mnras/stw1669 (cit. on pp. 16, 70).
Macquart, J. .-.-P. et al. (2020a), *A census of baryons in the Universe from localized fast radio bursts*, Nature **581** 391, arXiv: 2005.13161 [astro-ph.CO] (cit. on p. 17).
– (2020b), *A census of baryons in the Universe from localized fast radio bursts*, Nature **581** 391, arXiv: 2005.13161 [astro-ph.CO] (cit. on p. 34).
Maggi, P. et al. (2019), *The supernova remnant population of the Small Magellanic Cloud*, A&A **631**, A127 A127, arXiv: 1908.11234 [astro-ph.HE] (cit. on p. 59).
Manchester, R. N. and IPTA (2013), *The International Pulsar Timing Array*, Classical and Quantum Gravity **30**, 224010 224010, arXiv: 1309.7392 [astro-ph.IM] (cit. on p. 10).
Manchester, R. N. et al. (2005), *The Australia Telescope National Facility Pulsar Catalogue*, AJ **129** 1993, eprint: astro-ph/0412641 (cit. on pp. 51, 72).
Manchester, R. N. et al. (2013), *The Parkes Pulsar Timing Array Project*, PASA **30**, e017 e017, arXiv: 1210.6130 [astro-ph.IM] (cit. on p. 9).
Manchester, R. et al. (2001), *The Parkes multi-beam pulsar survey – I. Observing and data analysis systems, discovery and timing of 100 pulsars*, Monthly Notices of the Royal Astronomical Society **328** 17, ISSN: 0035-8711, eprint: https://academic.oup.com/mnras/article-pdf/328/1/17/3116774/328-1-17.pdf, URL: https://doi.org/10.1046/j.1365-8711.2001.04751.x (cit. on p. 60).
Mauch, T. et al. (2020), *The 1.28 GHz MeerKAT DEEP2 Image*, ApJ **888**, 61 61, arXiv: 1912.06212 [astro-ph.GA] (cit. on p. 44).

McCready, L. L., J. L. Pawsey and R. Payne-Scott (1947), *Solar Radiation at Radio Frequencies and Its Relation to Sunspots*, Proceedings of the Royal Society of London Series A **190** 357 (cit. on p. 17).

McKee, J. W. et al. (2019), *A detailed study of giant pulses from PSR B1937+21 using the Large European Array for Pulsars*, MNRAS **483** 4784, arXiv: 1811.02856 [astro-ph.HE] (cit. on pp. 75, 77).

McLaughlin, M. A. and J. M. Cordes (2003), *Searches for Giant Pulses from Extragalactic Pulsars*, The Astrophysical Journal **596** 982, URL: https://doi.org/10.1086/378232 (cit. on pp. 24, 70).

McLaughlin, M. A. et al. (2006), *Transient radio bursts from rotating neutron stars*, Nature **439** 817, arXiv: astro-ph/0511587 [astro-ph] (cit. on p. 24).

Melrose, D. B. (1971), *Induced Compton Scattering by Relativistic Particles*, Ap&SS **13** 56 (cit. on p. 70).

Moore, C. J., R. H. Cole and C. P. L. Berry (2015), *Gravitational-wave sensitivity curves*, Classical and Quantum Gravity **32**, 015014 015014, arXiv: 1408.0740 [gr-qc] (cit. on p. 9).

Mort, B. et al. (2016), *Analysing the impact of far-out sidelobes on the imaging performance of the SKA-LOW telescope*, Monthly Notices of the Royal Astronomical Society **465** 3680, ISSN: 0035-8711, eprint: https://academic.oup.com/mnras/article-pdf/465/3/3680/8576490/stw2814.pdf, URL: https://doi.org/10.1093/mnras/stw2814 (cit. on p. 37).

Muñoz, J. B., V. Ravi and A. Loeb (2020), *Periodic Fast Radio Bursts from Young Neutron Stars*, The Astrophysical Journal **890** 162, URL: https://doi.org/10.3847/1538-4357/ab6d62 (cit. on p. 70).

Muslimov, A. G. and A. K. Harding (2003), *Extended Acceleration in Slot Gaps and Pulsar High-Energy Emission*, ApJ **588** 430, arXiv: astro-ph/0301023 [astro-ph] (cit. on pp. 13, 14).

Narayan, R. (1992), *The Physics of Pulsar Scintillation*, Philosophical Transactions: Physical Sciences and Engineering **341** 151, ISSN: 09628428, URL: http://www.jstor.org/stable/53917 (cit. on p. 6).

Newburgh, L. B. et al. (2016), "HIRAX: a probe of dark energy and radio transients", *Ground-based and Airborne Telescopes VI*, ed. by H. J. Hall, R. Gilmozzi and H. K. Marshall, vol. 9906, Society of Photo-Optical Instrumentation Engineers (SPIE) Conference Series 99065X, arXiv: 1607.02059 [astro-ph.IM] (cit. on p. 30).

Ng, C. et al. (2015), *The High Time Resolution Universe Pulsar Survey - XII. Galactic plane acceleration search and the discovery of 60 pulsars*, MNRAS **450** 2922, arXiv: 1504.08000 [astro-ph.HE] (cit. on p. 60).

Obrocka, M., Stappers, B. and Wilkinson, P. (2015), *Localising fast radio bursts and other transients using interferometric arrays*, A&A **579** A69, URL: https://doi.org/10.1051/0004-6361/201425538 (cit. on p. 50).

Oppermann, N., H.-R. Yu and U.-L. Pen (2018), *On the non-Poissonian repetition pattern of FRB121102*, Monthly Notices of the Royal Astronomical Society **475** 5109, ISSN: 0035-8711, eprint: https://academic.oup.com/mnras/article-pdf/475/4/5109/24111409/sty004.pdf, URL: https://doi.org/10.1093/mnras/sty004 (cit. on p. 78).

Parkinson, P. M. S. et al. (2016), *CLASSIFICATION AND RANKING OFFERMILAT GAMMA-RAY SOURCES FROM THE 3FGL CATALOG USING MACHINE LEARNING TECHNIQUES*, The Astrophysical Journal **820** 8, URL: https://doi.org/10.3847/0004-637x/820/1/8 (cit. on p. 56).

Peebles, P. J. E. and R. H. Dicke (1968), *Origin of the Globular Star Clusters*, ApJ **154** 891 (cit. on p. 10).
Penzias, A. A. and R. W. Wilson (1965), *A Measurement of Excess Antenna Temperature at 4080 Mc/s.*, ApJ **142** 419 (cit. on p. 4).
Petroff, E. et al. (2016a), *FRBCAT: The Fast Radio Burst Catalogue*, PASA **33**, e045 e045, arXiv: 1601.03547 [astro-ph.HE] (cit. on p. 16).
– (2016b), *FRBCAT: The Fast Radio Burst Catalogue*, PASA **33**, e045 e045, arXiv: 1601.03547 [astro-ph.HE] (cit. on p. 34).
Petrova, S. A. (2004), *On the origin of giant pulses in radio pulsars*, A&A **424** 227, URL: https://doi.org/10.1051/0004-6361:20047171 (cit. on p. 68).
Philippov, A. et al. (2019), *Pulsar Radio Emission Mechanism: Radio Nanoshots as a Low-frequency Afterglow of Relativistic Magnetic Reconnection*, The Astrophysical Journal **876** L6, URL: https://doi.org/10.3847/2041-8213/ab1590 (cit. on pp. 13–15, 70, 71).
Ransom, S. M. (2008), "Pulsars in Globular Clusters", *Dynamical Evolution of Dense Stellar Systems*, ed. by E. Vesperini, M. Giersz and A. Sills, vol. 246 291 (cit. on p. 11).
Ransom, S. M. (2001), *New search techniques for binary pulsars*, PhD thesis: Harvard University (cit. on p. 58).
Reber, G. (1944), *Cosmic Static.*, ApJ **100** 279 (cit. on p. 3).
Ridolfi, A. et al. (2021), *Eight new millisecond pulsars from the first MeerKAT globular cluster census*, MNRAS, arXiv: 2103.04800 [astro-ph.HE] (cit. on pp. 56, 57).
Ridolfi, A. (2017), *Long-term timing of pulsars in globular clusters*, PhD thesis: Rheinische Friedrich-Wilhelms-Universität Bonn, URL: http://hdl.handle.net/20.500.11811/7319 (cit. on p. 47).
Romani, R. W., R. Narayan and R. Blandford (1986), *Refractive effects in pulsar scintillation.*, MNRAS **220** 19 (cit. on p. 60).
Romani, R. W. and S. Johnston (2001a), *Giant Pulses from the Millisecond Pulsar B1821-24*, The Astrophysical Journal **557** L93, URL: https://doi.org/10.1086/323415 (cit. on pp. 15, 68).
– (2001b), *Giant Pulses from the Millisecond Pulsar B1821-24*, The Astrophysical Journal **557** L93, URL: https://doi.org/10.1086/323415 (cit. on p. 68).
Roy, J., J. N. Chengalur and U.-L. Pen (2018), *A Post-correlation Beamformer for Time-domain Studies of Pulsars and Transients*, ApJ **864**, 160 160, arXiv: 1808.01088 [astro-ph.IM] (cit. on pp. 35, 36).
Salvetti, D. et al. (2015), *Multi-wavelength Observations of 3FGL J2039.6-5618: A Candidate Redback Millisecond Pulsar*, ApJ **814**, 88 88, arXiv: 1509.07474 [astro-ph.HE] (cit. on p. 58).
Sanidas, S. et al. (2018), "MeerTRAP: A pulsar and fast transients survey with MeerKAT", *Pulsar Astrophysics the Next Fifty Years*, ed. by P. Weltevrede et al., vol. 337 406 (cit. on p. 42).
Shannon, R. M. et al. (2013), *Gravitational-wave limits from pulsar timing constrain supermassive black hole evolution.*, Science **342** 334, arXiv: 1310.4569 [astro-ph.CO] (cit. on p. 9).
Shimrat, M. (1962), *Algorithm 112: Position of Point Relative to Polygon*, Commun. ACM **5** 434, ISSN: 0001-0782, URL: https://doi.org/10.1145/368637.368653 (cit. on p. 39).
Singal, A. K. and H. O. Vats (2012), *GIANT-PULSE EMISSION FROM PSR B0950+08*, The Astronomical Journal **144** 155, URL: https://doi.org/10.1088/0004-6256/144/5/155 (cit. on p. 78).
Smits, R. et al. (2009), *Pulsar science with the Five hundred metre Aperture Spherical Telescope*, A&A **505** 919, arXiv: 0908.1689 [astro-ph.IM] (cit. on p. 34).

Spitkovsky, A. (2006), *Time-dependent Force-free Pulsar Magnetospheres: Axisymmetric and Oblique Rotators*, The Astrophysical Journal **648** L51, URL: https://doi.org/10.1086/507518 (cit. on p. 13).

Spitler, L. G. et al. (2014), *Fast Radio Burst Discovered in the Arecibo Pulsar ALFA Survey*, ApJ **790**, 101 101, arXiv: 1404.2934 [astro-ph.HE] (cit. on p. 34).

Spitler, L. G. et al. (2016), *A repeating fast radio burst*, Nature **531** 202, arXiv: 1603.00581 [astro-ph.HE] (cit. on p. 16).

Stappers (2016), "MeerTRAP: Real Time Commensal Searching for Transients and Pulsars with MeerKAT", *MeerKAT Science: On the Pathway to the SKA* 10 (cit. on pp. 42, 62).

Stappers, B. W. and M. Kramer (2016), "An Update on TRAPUM", *MeerKAT Science: On the Pathway to the SKA* 9 (cit. on p. 28).

Staveley-Smith, L. et al. (1996), *The Parkes 21 CM multibeam receiver*, PASA **13** 243 (cit. on pp. 4, 34).

Sturrock, P. A. (1971), *A Model of Pulsars*, ApJ **164** 529 (cit. on p. 12).

Swart, G. P. and P. Dewdney (2020), "Highlights of the SKA1-Mid Telescope architecture", *Society of Photo-Optical Instrumentation Engineers (SPIE) Conference Series*, vol. 11450, Society of Photo-Optical Instrumentation Engineers (SPIE) Conference Series 114502T (cit. on pp. 27, 53).

Tauris, T. M. and E. P. J. van den Heuvel (2014), *FORMATION OF THE GALACTIC MILLISECOND PULSAR TRIPLE SYSTEM PSR J0337+1715—A NEUTRON STAR WITH TWO ORBITING WHITE DWARFS*, The Astrophysical Journal **781** L13, URL: https://doi.org/10.1088/2041-8205/781/1/L13 (cit. on p. 11).

Taylor, J. H. and J. M. Weisberg (1982), *A new test of general relativity - Gravitational radiation and the binary pulsar PSR 1913+16*, ApJ **253** 908 (cit. on p. 9).

The CHIME/FRB Collaboration et al. (2021a), *The First CHIME/FRB Fast Radio Burst Catalog*, arXiv e-prints, arXiv:2106.04352 arXiv:2106.04352, arXiv: 2106.04352 [astro-ph.HE] (cit. on pp. 16, 24).

– (2021b), *The First CHIME/FRB Fast Radio Burst Catalog*, arXiv e-prints, arXiv:2106.04352 arXiv:2106.04352, arXiv: 2106.04352 [astro-ph.HE] (cit. on p. 34).

Observation of Pulsed γ-Rays Above 25 GeV from the Crab Pulsar with MAGIC (2008), Science **322** 1221, ed. by The MAGIC Collaboration et al., ISSN: 0036-8075, eprint: https://science.sciencemag.org/content/322/5905/1221.full.pdf, URL: https://science.sciencemag.org/content/322/5905/1221 (cit. on pp. 7, 68).

Thompson, A. R. (1982), *The response of a radio-astronomy synthesis array to interfering signals.*, IEEE Transactions on Antennas and Propagation **30** 450 (cit. on p. 19).

Thompson, C. and R. C. Duncan (1995), *The soft gamma repeaters as very strongly magnetized neutron stars - I. Radiative mechanism for outbursts*, Monthly Notices of the Royal Astronomical Society **275** 255, ISSN: 0035-8711, eprint: https://academic.oup.com/mnras/article-pdf/275/2/255/18539652/mnras275-0255.pdf, URL: https://doi.org/10.1093/mnras/275.2.255 (cit. on p. 11).

Tiburzi, C. (2018), *Pulsars Probe the Low-Frequency Gravitational Sky: Pulsar Timing Arrays Basics and Recent Results*, PASA **35**, e013 e013, arXiv: 1802.05076 [astro-ph.IM] (cit. on p. 9).

Titus, N. et al. (2019), *Targeted search for young radio pulsars in the SMC: discovery of two new pulsars*, MNRAS **487** 4332, arXiv: 1906.04592 [astro-ph.HE] (cit. on p. 59).

Titus, N. et al. (2020), *The radio pulsar population of the Small Magellanic Cloud*, MNRAS **494** 500, arXiv: 2003.01969 [astro-ph.SR] (cit. on p. 57).

Totani, T. (2013), *Cosmological Fast Radio Bursts from Binary Neutron Star Mergers*, Publications of the Astronomical Society of Japan **65**, L12, ISSN: 0004-6264, eprint: https://academic.oup.com/pasj/article-pdf/65/5/L12/9718269/pasj65-0L12.pdf, URL: https://doi.org/10.1093/pasj/65.5.L12 (cit. on p. 16).

van Straten, W. and M. Bailes (2011), *DSPSR: Digital Signal Processing Software for Pulsar Astronomy*, PASA **28** 1, arXiv: 1008.3973 [astro-ph.IM] (cit. on p. 75).

van Straten, W. et al. (2010), *PSRCHIVE and PSRFITS: Definition of the Stokes Parameters and Instrumental Basis Conventions*, PASA **27** 104, arXiv: 0912.1662 [astro-ph.IM] (cit. on p. 75).

Van Veen, B. D. and K. M. Buckley (1988), *Beamforming: a versatile approach to spatial filtering*, IEEE ASSP Magazine **5** 4 (cit. on p. 35).

Walsh, G. and R. Lynch (2018), "Searching for Single Pulses Using Heimdall", *American Astronomical Society Meeting Abstracts #231*, vol. 231, American Astronomical Society Meeting Abstracts 243.04 (cit. on p. 76).

Wang, N., R. N. Manchester and S. Johnston (2007), *Pulsar nulling and mode changing*, Monthly Notices of the Royal Astronomical Society **377** 1383, ISSN: 0035-8711, eprint: https://academic.oup.com/mnras/article-pdf/377/3/1383/5689745/mnras0377-1383.pdf, URL: https://doi.org/10.1111/j.1365-2966.2007.11703.x (cit. on p. 8).

Wex, N. and M. Kramer (2020), *Gravity Tests with Radio Pulsars*, Universe **6** 156 (cit. on p. 60).

Williamson, I. P. (1972), *Pulse broadening due to multiple scattering in the interstellarmedium*, MNRAS **157** 55 (cit. on p. 79).

Yao, J. M., R. N. Manchester and N. Wang (2017), *A New Electron-density Model for Estimation of Pulsar and FRB Distances*, The Astrophysical Journal **835** 29, URL: http://stacks.iop.org/0004-637X/835/i=1/a=29 (cit. on p. 15).

You, X. P. et al. (2007), *Dispersion measure variations and their effect on precision pulsar timing*, Monthly Notices of the Royal Astronomical Society **378** 493, ISSN: 0035-8711, eprint: https://academic.oup.com/mnras/article-pdf/378/2/493/2838682/mnras0378-0493.pdf, URL: https://doi.org/10.1111/j.1365-2966.2007.11617.x (cit. on p. 75).

Zhang, F. (2017), *Pulsar magnetospheric convulsions induced by an external magnetic field*, A&A **598**, A88 A88, arXiv: 1701.01209 [astro-ph.HE] (cit. on p. 16).

List of Figures

List of Tables